Atomically Thin Stacks of Polar Insulators: A Route to Atomic-Scale Multiferroics

Jose Martinez Castro

Submitted in partial fulfillment

of the requirements for the degree of

Doctor of Philosophy

of

University College London.

Department of Physics and Astronomy

University College London

University of London

August 1, 2016

I declare that the work presented in this thesis is my own. Where information has been obtained from other sources, I declare this has been clearly indicated in the thesis.

Abstract

The continuous demand for smaller electronic components is forcing industry to consider devices at the atomic scale. One of the side effects of size reduction in electronic devices is the appearance of quantum effects, which preclude engineers from simply scaling down the functionality of existing components. In the case of data storage, different approaches have been followed to increase of information density, for instance a reduction of the physical bit size or a combination of different properties (like magnetic and ferroelectric) to achieve more than two states in which to store data. Nonetheless, combining ferroelectric and magnetic properties has been difficult since there is a contra-indication between the conventional mechanism for cation off-centring in ferroelectrics and the formation of magnetic moments. Moreover, the observation of ferroelectric and magnetoelectric effects at the atomic scale has remained difficult due to physical constraints.

Using scanning tunnelling microscopy and spectroscopy we study the effects of stacking sodium chloride bilayer and monolayer (NaCl), that is, an atomically thin ionic insulator, on top of copper nitride (Cu_2N), which is another atomically thin insulating layer. We observe that NaCl exhibits inverse piezoelectric behaviour - displacement of the atoms driven by an applied electric field – that can reverse electric dipole orientations. Small detected hysteresis suggests that is an incipient ferroelectric behaviour, further confirmed when the same experiment is performed on top of defects of the NaCl layer, where the dipole reversal is pinned and the ferroelectric cycle broadened.

Combined capabilities of the microscope – single atom evaporation and high energy resolution – allow us to study spin excitation of single magnetic impurities when adsorbed on certain substrates. Co atoms adsorbed on top of NaCl defects give us the chance to perform inelastic electron tunnelling spectroscopy (IETS) and ferroelectric

cycles at the same time; with this, we observe a change in the magnetic excitation spectrum as a function of the polarization state of the supporting substrate.

These results suggest a new way to create piezoelectric effects at the interface between ultra-thin insulating polar materials near conducting electrodes, pushing the feasible size of functional polar materials down to the atomic scale. Incipient ferroelectric manifestations in combination with STM capabilities allow us to study the fundamental interactions between magnetocrystalline anisotropy, magnetic moment and electric polarization, providing in practice the proof of concept of a multiferroic device at the atomic scale.

Acknowledgements

Almost four years ago I showed up in David's office asking for help, I wanted to go to Germany and try a Ph.D. there. He did not ask me neither why I wanted to go or my grades. After some months he offered me this opportunity, a combined UCL-UZ-SPECS project. Dr Hirjibehedin and Dr Serrate could have waited and chose another student but they didn't.

Two years ago I came up with this crazy idea of depositing NaCl on top of Cu_2N. They said that it was a very interesting and allowed me to go for it despite of other projects which were actually very interesting. I could not even be more satisfied with the trust they had on me. In these three years I have tried to do my best in every day spent in the lab and of course, in my desk. So I just can say thank you very much Dr Cyrus F. Hirjibehedin for your infinite patience, for standing my bad language and seeing the bright side of everything. Dr. David Serrate, I am very thankful for your infinite patience (did I say infinite patience again?) teaching every minor detail of the STM technique.

Before acknowledging all the folks in Spain I would like to thanks to UCL for supporting this thesis that it was possible in collaboration with SPECS GmbH. SPECS GmbH has done a big financial effort that has made possible this thesis and particularly to Andreas Thissen and Oliver Schaff for their interest in this partnership. In the same way, I would like to thanks Universidad de Zaragoza for bringing all the equipment to the project. Without this partnership within these two institutions and this great company, this thesis would not have been possible. I would also like to thanks Mats Persson for his theoretical support, who carried out all the DFT calculations. Without his calculations, this work would have been barely understood.

As a spanish person I cannot express myself and to my friends and colleagues in other language that it is not spanish. So please, let us write a few words for them in

this language.

Primeramente, me siento obligado a agradecer a la gente del labo lo que me ha ayudado y enseñado. Maria de mi vida y de mi corazón, gracias por tener paciencia conmigo, por las meteduras de pata y por enseñarme todo el cacharreo. Eres una gran persona. Hallo Marten! *Grrrassiias* por enseñarme como tunelear *electronos* en tu máquina y por enseñarme el verdadero acento texano. Tú también has tenido infinita paciencia conmigo. Dankeschön! Carlicos, sin tus super habilidades de super técnico todavía estaría construyendo el evaporador. No habría llegado ni a la mitad de donde he llegado sin tu ayuda. Mari, Coffey, gracias por esa grata compañía mientras hemos coincidido en el labo.

Ciertamente estos tres años que he pasado en Zaragoza habrían sido un tostón de no ser por todos los amiguitos que he hecho dentro y fuera del INA. Laurita, gracias por ser como eres, con tus comentarios extremadamente incorrectos y tu gran corazón. Inesita, eres una crack en todos los sentidos, ciertamente, tienes un gusto exquisito con el humor. Serranito, me caes de fruta madre tío, aderecemos muchas más noches con litros y litros de cerveza! (Starship Troopers mola). Pili, Pilarica, Mapi, Maripili, eres de las pocas personas que entiende mi humor inigualable porque tú también eres inigualable. Eres top top top...! Alberto, me encantan tus ironías y particular sarcasmo. Hemos compartido grandes frikimomentos juntos. Chisma, fuiste el fichaje revelación 2014 gran año lleno de grandes acontecimientos. Nada comparable a tu llegada al INA (todo el mundo lo sabe) y esos barrancos y caminatas montañeras. Beíta, soriana ilustre donde las haya, acérrima defensora de costumbres ancestrales (Catapán, Lavalenguas, La Saca, Viernes De Toros, Bailas y no sé qué más) eres como una mamá, siempre dedicada a tu gente. Marcos digo... Mario! Obviamente has sido el fichaje estrella de 2015 eclipsando las demás figuras y personajes del INA. Nu tengu problema en falar Asturianu ho! Javi de Loscos y derredores, gracias por tus risas descontroladas con mis magníficos chistes y ocurrencias de primer nivel.

Acabado con la gente del despacho o del contiguo debo agradecer el tiempo compartido a otros miembros que son o han sido de la familia INA. A los queridos colombianos bailongos, Luislorena o Loreluis, pues son inseparables y el uno es todo y el todo es uno. Amenizasteis mucho el tiempo que compartí con vosotros, con el día del amor y la amistad y el café colombiano... consiguiendo hacer piña. A Pavel, siempre

dispuesto y realmente buena persona. La secta del TEM, haciendo más agradable la hora de la comida con temas de conversación dispares, espero no dejarme a nadie, César, Rodrigo, Álvaro, Alfonso y Luc. A Myriam, que no se muy bien en qué grupo colocarte. Tienes mucha paciencia soportanto mi nefasto acento argentino. Irene que eres todo carácter con técnicas mortales de taekwondoin! A los chicos de la sala blanca aunque no haya coincidido demasiado con ellos. Y cómo no al caimán de la misma charca señor Teobaldo.

No todo en esta vida es trabajo y aunque probablemente no lean estos agradecimientos me gustaría aprovechar la oportunidad para agradecer a mis amigos escaladores el tiempo compartido, especialmente a Carlos y el furgoneteo extremo, a la super maestra Sof a Javi, Miguel, Marta, Borja, Pedrete, Fer y Jean. Por supuesto tengo aquí mi espacio reservado a Candanchú S.A. y a mí mismo y mi torpeza por hacerme los últimos meses de mi tesis infinitamente más fáciles.

A mis amigos de Benidorm que NO bailan los pajaritos, Javi, Agus, Adri, Javito, Fran, Gabi, Iván, Loly, Mía, Diana... podría seguir hasta mañana.

El último párrafo es el más especial para mí pues lo dedico a mi familia, que me ha apoyado incondicionalmente en todo lo que he hecho. Gracias mamá por ser como eres, nunca habrá palabras para agredecerte todo lo que has hecho por mí. Jamás habría llegado donde estoy ahora de no ser por tí. Siempre sacrificándote por los demás. Padre, gracias por todo. Hermanita, me has ayudado un montón aquí en Zaragoza, solo tengo palabras de agradecimiento hacia tí. Javier, por supuesto, gracias por todo con esos grandes momentos de HeartBreak y en Zaragoza también, que lo hemos pasado en grande. Al pequeño Javi, la alegría de la huerta que hizo mi convalecencia muchísimo más llevadera y que quiero con locura. A mi hermano que por desgracia lo veo muchísimo menos de lo que me gustaría pero que siempre lo llevo en mis pensamientos. A Mariajo y a esas dos preciosidades que siempre estoy deseando ver, Marta y María.

Contents

Chapter 1

Introduction

1.1 Ferroelectricity

In this section we highlight some of the major concepts that underpin the topic of ferroelectricity. For a more detailed introduction, the reader is referred to the following excellent introductions [1, 2], from which much of the material in this section is taken. A ferroelectric material can be defined as an insulating system with two or more discrete stable or metastable states of different nonzero electric polarization separated by a finite energy barrier [1, 2]. The states can be switched via an applied electric field reversing in this way the electric polarization P. Electric polarization can be defined as the dipole moment obtained from the charge density divided by the volume of the system.

The electrical properties of a ferroelectric film can be measured when it is fabricated as a device. A ferroelectric material between the two electrodes becomes a capacitor. Since a change in the electric polarization is related to an increase of the measured current, by peforming voltage sweeps at a speed adapted to the charging time of the capacitor, it is possible to obtain the polarization of the ferroelectric sample and then its change with the ferroelectric cycle [2] (Fig. 1.1).

In ferroelectric crystals, the spontaneous polarization is produced by the atomic arrangement of ions in the crystal structure away from the position of perfect dipole compensation. Furthermore, it also must be possible to switch between different states by means of an applied electric field.

Among the different questions the ferroelectric community has been trying to answer, one of the most important ones has been what the critical thickness of a film is for

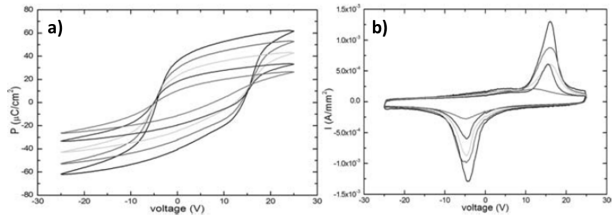

Figure 1.1: a) Hysteresis loops for a number of $PbTiO_3/SrTiO_3$ superlattice samples with different polarizations. b) The corresponding current-voltage loops (obtained during voltage sweeps in which the voltage is cycled, in contrast to leakage current I-V curves that measure current when the voltage is held constant for a period of time) from which the polarization-voltage hysteresis loops are obtained, showing clear switching peaks at the coercive voltage of the sample [2]. *Permission to reproduce this graphs has been granted by Springer ebook.*

which ferroelectricity is impossible. Past experiments have shown that it is possible to preserve ferroelectricity in ultra-thin films, reaching a critical thickness of 1.2 nm for $PbTiO_3$ grown on the (001) face of $SrTiO_3$ [3]. In order to reach such small dimensions one of the requisites is to avoid the depolarization field. In a metal, free charges will screen the spontaneous polarization of the ferroelectric layer. Depolarization field can be described in a simple equation:

$$\varepsilon_d = -2\frac{\lambda_{eff}}{d\varepsilon_0}P \tag{1.1}$$

where d is the thickness of the dielectric, ε_d is the depolarization field, λ_{eff} is the effective screening length into the dielectric and ε_0 the dielectric constant [1].

These parameters will gain relevance in the future where thanks to the insulating nature of our substrate an induced out of plane polarization will be preserved on our structure, allowing us to study in this way directly the piezoelectric response of the system.

1.2 Magnetism

The magnetic properties at atomic scale are given by the orbital population of the atoms and the interaction with their surroundings. The design of new devices call for the understanding of the fundamental properties and the effect of the different couplings of the environment with the atom. In this section, we are going briefly to describe the result of applying magnetic fields over magnetic atoms (Zeeman effect), the consequences of adding magnetic centers on a crystal lattice (magnetocrystalline

anisotropy and crystal field effect) and the interaction of the magnetic impurities with a host metal (Kondo effect).

1.2.1 Zeeman Effect

The Zeeman effect is the splitting of the spectral lines that occurs when a localized magnetic moment (composed by spin and orbital angular momenta) interacts with a static magnetic field (see Fig. 1.2). When a magnetic field is applied, the energy of the atom changes because of the interaction of its magnetic moment with the field [4].

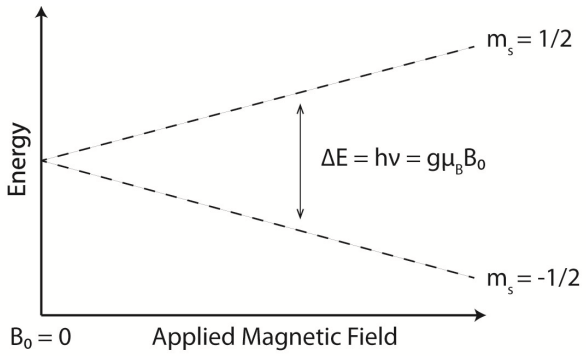

Figure 1.2: Zeeman splitting for a free atom of spin 1/2.

The electrons conforming an atomic term have an intrinsic spin angular momentum S so the spin magnetic moment μ_s will be expressed as:

$$\vec{\mu}_S = -2\frac{\mu_B}{\hbar}\vec{S} \tag{1.2}$$

where μ_B is the Bohr magneton and the factor of 2 is the Landé factor for a purely spin mangetic moment. When the spin and angular momentum l of an electron in an atom are simultaneously taken into account, the magnetic moment operator becomes:

$$\mu_S = -\frac{\mu_B}{\hbar}(2S_z + l_z) \tag{1.3}$$

For an n-electron atom, the magnetic moment is:

$$\mu_S = -\frac{\mu_B}{\hbar}(2S_z + L_z) \tag{1.4}$$

with S, and L the allowed total spin and angular momenta values. The energy E_z of a

magnetic moment in a uniform magnetic field taken along the z-direction is:

$$E_z = -\mu_S B_z \tag{1.5}$$

In the absence of a magnetic field, the energy levels of a free atom are characterized by the quantum numbers J and M of a total angular momentum and its projection onto a given quantization axis, each J value having a degeneracy of 2J+1 with M taking values between +J and -J.

The energy shift of an eigenvector $|\alpha JM\rangle$ (α represents all other quantum numbers of the state) in the presence of a magnetic field applied along the quantization axis will be:

$$\Delta E_Z = B_z \langle \alpha JM | \mu_s | \alpha JM \rangle \tag{1.6}$$

With some calculations [5], it is easy to get:

$$\Delta E = g_{\alpha J} \mu_B B M \tag{1.7}$$

where g is called the Lande g-factor of the level and M will be the total spin of the atom. The g-factor provides information about orbital and spin components of the magnetic moments, and therefore it is sensitive to the spin-orbit coupling.

1.2.2 Magnetocrystalline Anisotropy and Crystal Field Effect

The magnetocrystalline anisotropy is the tendency of the magnetization to align itself along a preferred crystallographic direction; likewise the magnetocrystalline energy is defined as the energy difference per volume unit between samples magnetized on the easy and the hard axis [4].

When a magnetic field is applied the electronic spin will minimize the Zeeman energy by aligning parallel to it. Nonetheless the spin moment is generally coupled to the lattice due to the spin-orbit coupling, which makes it harder to align in the direction of a hard axis because the anisotropy energy counterbalances the Zeeman energy gain. For this reason, the spin-orbit coupling is the main interaction responsible for magnetic anisotropy.

The strength of the magnetocrystalline anisotropy is characterized phenomenologicaly by the magnitude of the anisotropy constants K0, K1... and depends on several

variables like the material, temperature, etc.: these values are expressed as energy densities. The magnetocrystalline anisotropy energy (MAE) must have the same symmetry as the crystal structure, and therefore it can be expressed as a series expansion of the director cosines α_i, relative to the projections of the magnetization direction onto the principal crystallographic axis. [4]. For a cubic crystal the energy can be expressed in the following way:

$$E = K_0 + K_1(\alpha_1^2\alpha_2^2 + \alpha_2^2\alpha_3^2 + \alpha_1^2\alpha_3^2) + K_2(\alpha_1^2\alpha_2^2\alpha_3^2) + \cdots \tag{1.8}$$

The magnitude of the magnetocrystalline anisotropy generally decreases with temperature more rapidly than magnetization and it vanishes at the Curie temperature or Curie point. Since the anisotropy is related with the coercive field, at the Curie point the coercivity will become zeroed.

Magnetocrystalline anisotropy is not only found in bulk systems but also at the atomic scale and even on single atoms [6]. The study of these effects normally requires to work at low temperatures, so the thermal energy cannot overcome the magnetocrystalline energy. Due to the charge transfer and the distribution of spin-polarization away from the magnetic atom and into the network, it is possible to induce a stable spin since an extended spin polarization makes it more exposed to the lattice, resulting thus in the lifting of the degeneracy of spin states.

Transition metal ions are strongly affected by the local environment around them since the partially-filled 3d-orbitals are the outermost electronic shells. Depending on the symmetry of the local environment around the ion, the degeneracy of 3d-orbitals which carry spins can be lifted. As the 3d-orbitals have different angular distributions, orbitals with charge distribution closer to negatively charged ions are repelled and have a higher energy. Therefore the crystal field splits the degeneracy of the 3d-orbitals [6]. Due to the spin-orbit coupling, these changes affect the magnetic moment.

In the spin Hamiltonian method [6], the complex behaviour of the system is simplified into anisotropy constants; D and E. The correction to the single ion hamiltonian ascribed to spin-orbit coupling in a crystal electric field without cubic point symmetry, can be approximated to second order perturbation to be a quadratic function of

the spin operator $\vec{S}$ and D, where D is a real, symmetric tensor. By choosing the coordinate axes to be parallel with the eigenvectors of D, D is diagonal and therefore the hamiltonian is given by:

$$H_{CF} = D_{xx}S_x^2 + D_{yy}S_y^2 + D_{zz}S_z^2 \tag{1.9}$$

By subtracting the constant $\frac{1}{2}(D_{xx} + D_{yy})S(S+1)$ can be obtained:

$$H_{CF} = DS_z^2 + E\left(S_x^2 - S_y^2\right) \tag{1.10}$$

where $D = D_{zz} - \frac{1}{2}(D_{xx} + D_{yy})$ and $E = D_{xx} - Dyy$.

Summarizing, the first term is a representation of the axial term while the second one is the transverse term of the magnetic anisotropies, characterized respectively by D and E. The axial term splits the degeneracy of the spin-states on the basis of the magnitude of the spin's z projection S_z, while the transverse term mixes states of different S_z.

1.2.3 The Kondo Effect

The Kondo effect was discovered with the study of the variation of resistance in metals with the temperature. In pure metals, the electrical resistance decreases with temperature but in some metals containing magnetic impurities, the electrical resistance increases again below a certain temperature [7]. This effect remained unexplained until Kondo proposed a model in 1964 [8, 9]. It can be explained in terms of a scattering model where the spins of the conduction electrons of the host metal interacts with the magnetic impurities.

When the total spin of the impurity is non-zero, the electrons try to screen the spin of the atom. The Kondo resonance is the consequence of the spin exchange between the magnetic impurity and the electrons on the Fermi sea resulting in a many-body phenomenon.

From a classical point of view, an energy of $-\varepsilon$, is needed for an electron to hop from an occupied state to an empty state in the metal at E_F. An energy of $U + \varepsilon$ (where U is the Coulomb energy) is needed for the electron to hop from the metal to an empty state of the magnetic impurity. These fluctuations in the presence of

spin-spin interactions can lower the energy of the total system: impurity and host metal. From the quantum point of view, Heisenberg uncertainty principle allows the spin excitation as a virtual process of $\delta t \geq \frac{\hbar}{2\delta\varepsilon}$ (with δt and $\delta\varepsilon$ as time and energy uncertainties respectively). This will result in a new ground state with a lower total energy possessing an excitation on the DOS at Fermi level.

Kondo's theory describes the observed increase of the electrical resistance below a certain temperature scale, also called the Kondo temperature (T_K). However the model is not completely correct since for this theory the resistance diverges at 0 K.

This model starts by modelling a Hamiltonian that implies a host metal term, an impurity term and a hybridization term (Eq. 10):

$H = H_m + H_d + H_h$

$$H_m = \sum_{k,\sigma} \varepsilon(k) C^{\dagger}_{k,\sigma} C_{k,\sigma} \tag{1.11a}$$

$$H_d e = \sum_{\sigma} \varepsilon_d C^{\dagger}_{d,\sigma} C_{d,\sigma} \tag{1.11b}$$

$$H_h = \sum_{k,\sigma} V_(k) C^{\dagger}_{k,\sigma} C_{d,\sigma} + V_(k)^* C^{\dagger}_{d,\sigma} C_{k,\sigma} \tag{1.11c}$$

where $\varepsilon(k)$ is the energy eigenvalue for metal state k, $C^{\dagger}_{k,\sigma}$ and $C_{k,\sigma}$ are the creation and annihilation operators respectively, k is the wavevector, σ is the spin component, d is referred to d-impurity states and V_k is the hybridization potential of the impurity-conduction electrons system. The equation is solved by means of perturbation theory where the perturbation is the hybridization Hamiltonian. The main problem with this simplified model is that it does not take in account electron interactions. To solve this problem, Anderson included other local Coulomb correlations on the impurity term.

Anderson single impurity model assumes only a single orbital state that can be filled with zero, one or two electrons:

$$H_d = \sum_{\sigma} \varepsilon_d C^{\dagger}_{d,\sigma} C_{d,\sigma} + U n_{d\uparrow} n_{d\downarrow} \tag{1.12}$$

The problem can be simplified considering that the Coulomb energy is much higher than hybridization potential $(U >> V_K)$; in this case, the Anderson model becomes a

Kondo model [10]:

$$H = \sum_{k,\sigma} C^{\dagger}_{k,\sigma} C_{k,\sigma} + J\vec{S}' \cdot \vec{S} \tag{1.13}$$

where $\vec{S}$ is the spin of conduction electron at the impurity site and J is the exchange term. The impurity electron hops onto the band or the band electron hops onto the impurity leading to an antiferromagnetic exchange interaction between the local impurity spin and the conduction electron spin at the impurity site (Fig. 1.3). Therefore $J < 0$ and the total spin will be zero,which results in the so-called Kondo screening.

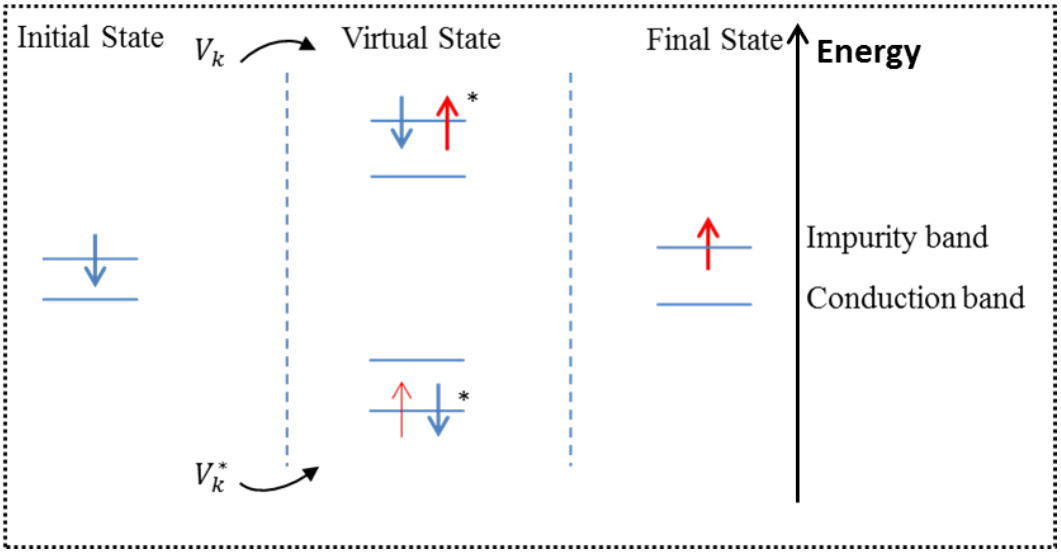

Figure 1.3: Schematic representation of spin transfer in Anderson model. The coherent superposition of this type of processes leads to the Kondo effect that manifests in the energy resolved dI/dV spectra as a peak close to the Fermi level.

Chapter 2

Experimental Techniques

2.1 Scanning Tunneling Microscopy

Since its design and invention [11], the scanning tunnelling microscope (STM) has been an exciting tool because it grants access to physical and chemical properties at the atomic scale. The possibility of measuring the local density of states (LDOS) of samples and its ability for manipulating atoms for the creation of complex structures [12] makes it very attractive for the study of systems that in other cases would have not been accessible. It can be said that STM is an excellent technique for observing the topography at atomic level as well as the LDOS of a given sample. A detailed explanation of STM as well as a theoretical explanation can be seen in Ref. [13]. Here we will present a brief review of the points that are most important for the understanding of this work.

2.1.1 The Tunnelling Effect

Scanning probe microscopy is a technique based on the idea that a surface is scanned by a physical probe. The surface is called sample and the physical probe, in the case of STM, is a metallic atomically sharp tip (Figure 2.1).

In the absence of an applied bias, the Fermi levels of the tip and the sample will be equalized and there will not be any net tunnelling current at absolute zero temperature. However, if a bias (V_T) is applied between the sample and the tip, there will be a probability of the electrons to cross the insulating barrier (vacuum), conserving their energy and spin. As a first approximation a simple model of STM in 1D can be written by just considering an energy barrier of height U_0 and an energy of the

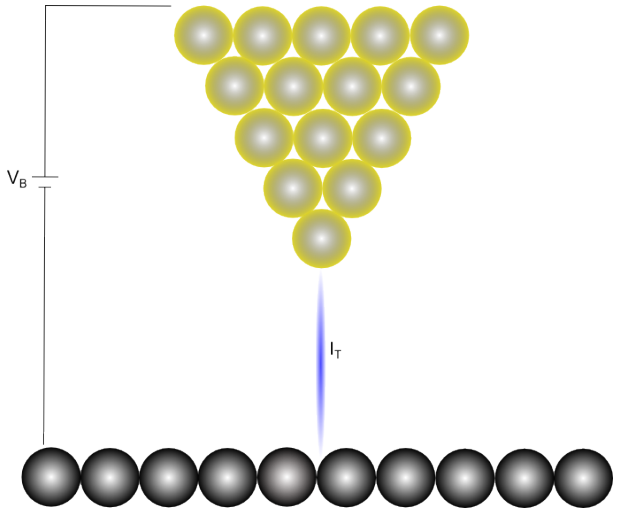

Figure 2.1: Representation of the tip-sample system on STM. A potential difference V_B is applied between the tip and the conducting sample producing a tunneling current I_T crossing from tip to sample.

electrons (considered as a planar wave function ψ) of E.

The time independent Schrödinger equation is

$$\frac{-\hbar^2}{2m}\frac{d^2\psi(z)}{dz^2} + U(z)\psi(z) = E\psi(z) \tag{2.1}$$

Starting the potential barrier at z=0, we have that the solution of the equation for $z < 0$ is

$$\psi(z) = \psi(0)e^{\pm ik_1 z}; \quad with \quad k_1 = \frac{\sqrt{2m(E-U_0)}}{\hbar} \tag{2.2}$$

The next step is to analyze what happens when the wave function enters the potential barrier. In the case $U_0 > 0$,

$$\psi(z) = \psi(0)e^{-k_2 z}; \quad with \quad k_2 = \frac{\sqrt{2m(U_0-E)}}{\hbar} \tag{2.3}$$

The wave function turns from a planar wave into an exponential decay. The higher the potential barrier is, the larger the decay will be. The probability density of an electron penetrating across the barrier from left to right is given by

$$|\psi(z)|^2 \propto |\psi(0)|^2 e^{-2k_2 z} \tag{2.4}$$

Using the work function of the metal as our reference point we can define the Fermi

energy of the system as $E_F = -\phi$. Tunnelling process can only occur if the Fermi levels between the two electrodes are not aligned. This can be achieved biasing one side of the junction with a voltage V. We will make the assumption that the bias applied in the junction is much lower than the average of the electrodes work functions in our system (this assumption will not be valid if we are studying states that are far from the Fermi level, like at 1 eV). In this way assuming that we have a rectangular barrier with the average barrier height, k_2 (generally expressed as k) can be described as:

$$k = \frac{\sqrt{2m(\frac{\phi_t+\phi_s)}{2}}}{\hbar} \tag{2.5}$$

where ϕ_t and ϕ_s are the work functions of the tip and sample.

In order to have a rough idea of the tunnel current dependence with the distance we can calculate the transmission coefficient, which describes the ratio of the intensity of the transmitted wave to that of the incident wave:

$$P(z) = \frac{I(z)}{I(0)} = e^{-2kz} \tag{2.6}$$

The work function is the minimum thermodynamic energy needed to remove an electron from a solid to the vacuum and it can be understood as the barrier height in our calculations. For metals it can go from around 2 eV up to 6 eV depending on the element [14]. Taking a typical value of 5 eV (like tungsten workfunction), 2k gives a value of 20 nm^{-1}. This means that a variation in z of 0.1 nm will give as a result one order of magnitude lower of the tunneling probability.

Elastic Tunnelling

The total current flowing across the junction can be calculated with a simple assumption: perfect one-dimensional metals for tip and sample. In sample bias convention (mainly used in STM community) the bias V_T is applied to the sample. An sketch of the junction that is described is shown in Fig. 2.2.

The current across the junction will be given by the rate at which a single particle will tunnel through the barrier. The Hamiltonian H that describes the system is separated into the time independent H_0 and a time dependent δH part. With the help of pertur-

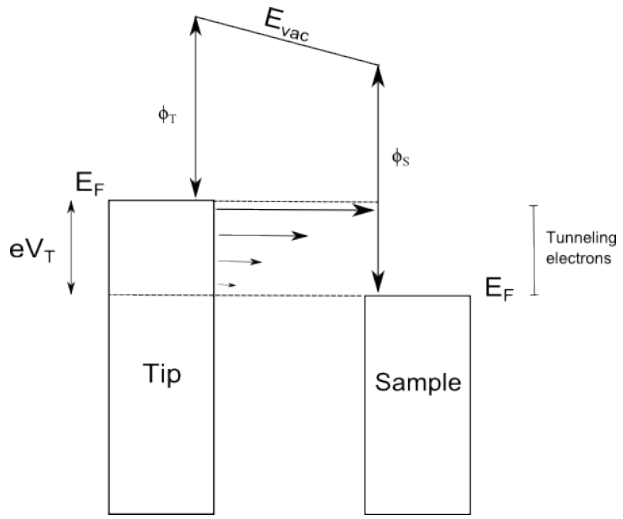

Figure 2.2: Tunnelling junction at T=0 K. E_F is the Fermi energy, ϕ_T and ϕ_S are the work functions of tip and sample respectively. In this example, the tip is at higher potential than the sample, this means that the electrons will tunnel from the tip to the sample.

bation theory, assuming that time dependent part results only in small perturbations, we can assume that the eigenstates of H are the same as H_0 [5]. The probability at which the system in state ψ_s (at the sample) at time $\tau = t_0$ and energy E_s will be in state ψ_t (at the tip) at time $\tau = t$ with energy E_t will be given by Fermi's golden rule:

$$W_{ts} = \frac{2\pi}{\hbar}|M_{ts}|^2 \delta\left(E_s - E_t\right) \tag{2.7}$$

where M_{ts} is the matrix element and it is given by $M_{ts} = \langle \psi_t | \delta H | \psi_s \rangle$, which in general is a non-trivial calculation as in the previous case of plane waves. As long as $T > 0K$ the tunnel junction will have two sets of transitions, one from the filled states in the sample to the empty states in the tip and one from the filled states in the tip to the empty states in the sample. Therefore, the total current is given by the difference between the two currents.

Fermi's golden rule give us the rate of transition for (in this case) the electrons to tunnel from one state to the other (sample to the tip). The rate of transitions has to be calculated for every energy in the tip and in the sample (every possible state) that will result in two. By multiplying the charge by the transition rate [13] and weighting the

thermal occupation with the Fermi Dirac distribution, f, we can obtain the current:

$$I_{s\to t} = \frac{4\pi e}{\hbar}\int_{-\infty}^{\infty} dE_t \int_{-\infty}^{\infty} dE_s \rho_t(E_t)\rho_s(E_s)f(E_s)(1-f(E_t))|M_{ts}|^2\delta(E_s - E_t - eV_T)dE \tag{2.8}$$

The sample and tip density of states appear after introducing Bardeen's approximation, which consists in treating the tunneling current as the sum of independent contributions from eigenstates at the tip and the sample (tip's and sample's states are separable). Remembering one of the properties of the Dirac′s delta function:

$$\int_{-\infty}^{\infty} f(t)\delta(t-T)dt = f(T) \tag{2.9}$$

where $t = E_t$ and $T = E_s - eV_T$, the solution of one of the integrals is immediate.

$$I_{s\to t} = \frac{4\pi e}{\hbar}\int_{-\infty}^{\infty} \rho_t(E - eV_T)\rho_s(E)f_s(E)(1-f_t(E-eV_T))|M_{ts}|^2 dE \tag{2.10}$$

where $f_s(E)$ are the occupied sample states and $1 - f_t(E - eV_T)$ are the unoccupied tip states.

Similarly the tunnelling current can be calculated from the tip to the sample and then, subtracting both currents $I_T = I_{(s\to t)} - I_{(t\to s)}$ the total current is obtained.

$$I_T = \frac{4\pi e}{\hbar}\int_{-\infty}^{\infty} [f(E) - f(E-eV_T)]\rho_t(E-eV_T)\rho_s(E)|M_{ts}|^2 dE \tag{2.11}$$

Assuming that the LDOS and M are constant and setting the temperature to 0 K, we have that only states between 0 and eV_T can tunnel.

$$I_T = \frac{4\pi e}{\hbar}\rho_t|M_{ts}|^2\int_0^{eV_T}\rho_s dE \tag{2.12}$$

The tunnelling current is therefore proportional to the integrated density of states.

2.1.2 Spectroscopy

One interesting feature is that STM allows us the possibility to perform spectroscopy [11], [15]. This means that with this technique it is possible to measure the LDOS of a conductive sample with spatial resolution. Two basic types of spectroscopies can

be carried out on STM. Like in the cases explained before we assume that the LDOS of the tip as well as the tunneling matrix element stay constant with energy, which allows us (from 2.11) to obtain the following relationship:

$$I_T = \frac{4\pi e}{\hbar}|M_{ts}|^2\rho_t \int_{-\infty}^{\infty}[f(E) - f(E - eV_T)]\rho_s(E)dE \tag{2.13}$$

Taking the derivative of the current with respect the applied bias V_T we obtain

$$\frac{dI_T}{dV_T} = \frac{4\pi e}{\hbar}|M_{ts}|^2\rho_t \int_{-\infty}^{\infty} -f'(E + eV_T)\rho_s(E)dE \tag{2.14}$$

When the temperature is approximately zero, the Fermi distribution turns into a step function and then, the derivative becomes a Dirac delta function. Taking this assumption, evaluating the integral is straightforward.

$$\frac{dI_T}{dV_T} = \frac{4\pi e}{\hbar}|M_{ts}|^2\rho_t \int_{-\infty}^{\infty} \rho_s(E)\delta(E + eV_T)dE = \frac{4\pi e}{\hbar}|M_{ts}|^2\rho_t\rho_s(eV_T) \tag{2.15}$$

Therefore, the derivative of the current is proportional to LDOS of the sample.
In real spectroscopy data acquisition there is a clear influence of the temperature. Hence, the temperature will cause a broadening, also called thermal broadening [16]. Taking the equation (2.14) and then calculating the derivative of the Fermi′s distribution gives:

$$\frac{dI_T}{dV_T} = \frac{4\pi e|M_{ts}|^2\rho_t}{\hbar} \int_{-\infty}^{\infty} \frac{\rho_s(E')}{4k_BT} sech^2\left(\frac{E'}{2k_BT}\right) dE' \tag{2.16}$$

The last assumption is considering a completely flat LDOS of the sample with an infinite peak (Dirac′s delta, $\rho_s = \delta(E - E')$ at a given energy. The integration is again immediate and it yields:

$$\frac{dI_T}{dV_T} = \frac{4\pi e|M_{ts}|^2\rho_t}{\hbar} sech^2\left(\frac{E}{2k_BT}\right) \tag{2.17}$$

This equation gives a quantitative solution of the maximum resolution that can be achieved if the temperature is non zero. One way to neglect any influence coming from the sample is thinking about the LDOS of the sample that is composed by a single infinite peak, the convolution with the thermal broadening will give us as a

result, a gaussian peak of at least $2k_BT$. This implies that the spectroscopy will not be sensitive to features within $2k_BT$.

Lock-in technique

There are two ways for the obtaining of a spectroscopic measurement, that is an energy resolved dI/dV curve: 1) taking an I(V) curve and differentiating it numerically and 2) taking the derivative electronically, which can be done with a lock-in amplifier. The second way often gives a higher signal/noise ratio.

The idea of the lock-in technique is simple. An AC bias modulation is added to the tunnelling DC voltage that is being ramped. The amplitude of the current response at the modulation frequency is proportional to the slope of the curve, and therefore proportional to the first derivative. As has been derived in equation 2.15, measuring the amplitude of the modulated current as a function of the DC bias will give a curve proportional to the energy resolved LDOS of the sample. The question is then,how this method is implemented in practice and how the signal to noise ratio is optimized.

.

From the equation 2.12 we know that the current is proportional to the integrated LDOS of the sample in the range between Fermi level and the sample potential eV sample. Introducing a small modulation in the tunnel voltage we get:

$$I_T \propto \int_0^{eV_T+eV_m sin(\omega_m t)} \rho_s(E)dE \tag{2.18}$$

where V_m is the modulation bias and ω_m the modulation frequency. Expanding in a Taylor series to first order:

$$I_T \propto \int_0^{eV_T} \rho_s(E)dE + \rho_s(eV_T)eV_m sin(\omega_m t) \tag{2.19}$$

The second part of the equation corresponds to the first derivative of the current. Once there is a simple way for describing the current response in terms of the modulation voltage, a noise signal characterized by the Fourier components a_ω can be added to the modulation. At the lock-in amplifier, the reference signal (the modulation of the bias) is convoluted by a multiplier with the whole current input signal conforming

the following equation:

$$\underbrace{sin(\omega_m t+\rho)}_{(1)}\left[\underbrace{\rho_s(E)eV_m sin(\omega_m t+\rho_0)}_{(2)}+\underbrace{\int_0^\infty a_\omega sin(\omega t+\rho_\omega)d\omega}_{(3)}\right] \tag{2.20}$$

The first part of the equation (1) corresponds to the reference signal. The reference signal is introduced by the lock-in which previously has been put in phase with the modulation signal. Part (2) of the equation corresponds to the modulated current signal and the third part to the noise inherent to the machine mechanical and electronic noise. With some calculations the output of the multiplier results in:

$$\frac{1}{2}\rho_s(E)eV_m[cos(\rho-\rho_0)+cos(2\omega_m t+\rho+\rho_0)]+... \tag{2.21}$$

Therefore the only contribution of the input signal [16] that has the same phase and frequency as the reference signal will be translated into the direct current signal, discarding noise with different phases. The high frequency contributions will be filtered by a low-pass filter leaving only the DC contribution proportional to the sample's LDOS. Here, the effective "temperature" will be a convolution of the microscope temperature and the inherent noises of the whole system. With this method it is possible to achieve spectroscopic resolution at the limit of the effective temperature if a small enough modulation amplitude is used.

Experimental aspects of the lock-in technique

The Lock-in system is composed of different modules (see fig. 2.3) that can be external to the microscope electronics or integrated. The most important parameters in a spectroscopy measurement are:

- Setpoint Bias Voltage: this setpoint will control the bias applied between the sample and the tip. For a constant current, a higher bias applied will result in a larger separation between the tip and the sample, and therefore a decrease in the tunnelling differential conductance we try to measure, resulting in a reduced signal/noise ratio.

- Setpoint Tunnel Current: this will control the total current passing through

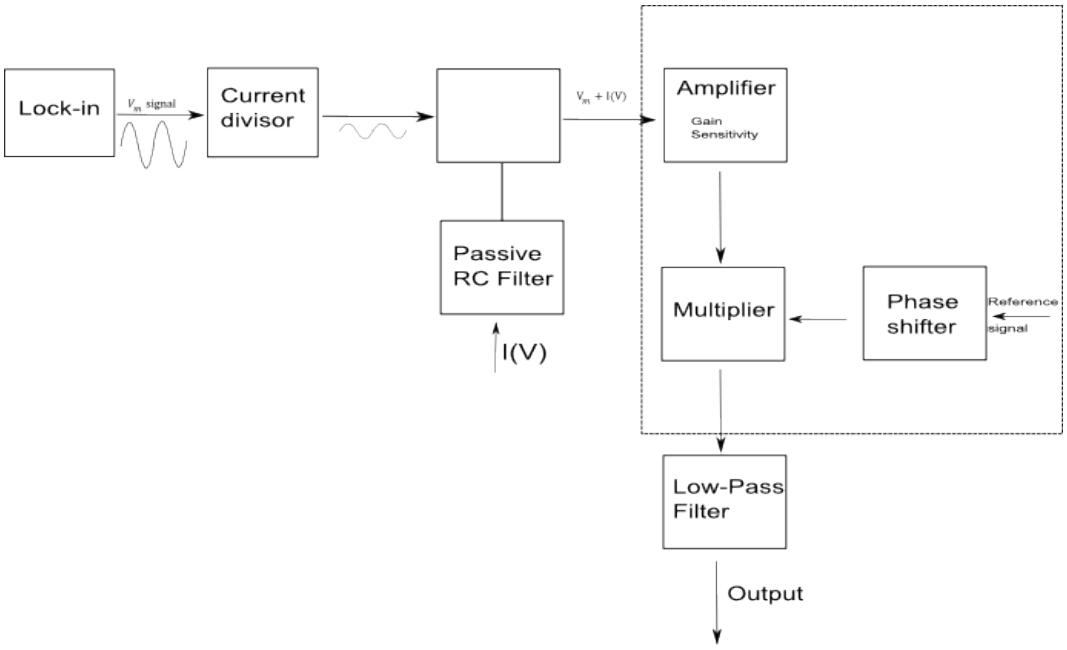

Figure 2.3: Schematic representation of the Lock-in system amplifier. Lock-in signal previously divided is mixed with the filtered tunnel current signal. The mixed signal is amplified and multiplied with a reference signal to only obtain DC contribution proportioanl to LDOS.

the tip to the sample at the setpoint bias voltage. As explained before, for a constant applied bias, a variation in the current will result in a variation of the distance between the sample and the tip. The intrinsic gap noise will not be reduced by this setting because the noise and the direct current will vary with a constant ratio between them. The electronic noise of the system, however, will be improved.

These two parameters are controlled by software settings and are mostly responsible for the lock-in signal saturation if the current that is passing through the sample is too high.

- Gain: it has control over the amount the current is amplified. The main role of the gain is to adjust the lock- in output to the full ADC voltage range of the control electronics.

- Oscillation Amplitude and Modulation: it is the oscillation introduced in the tunnelling current. The amplitude response depends on the slope of the *I(V)* curve and it is proportional on the first derivative. The modulation amplitude will determine the resolution and therefore the DC bias step in a spectroscopy

curve. With a peak to peak amplitude oscillation of 10 mV and a spectroscopy from -1 V to 1 V (that is between -1 eV and 1 eV around Fermi level) there will be 200 meaningful points.

- Integration Time: is the time after reaching each DC bias value of interest spent by the electronics averaging equivalent data points to decrease the noise (IT).

- Lock-in Integration Time: it is the time it takes to the lock-in to integrate the signal in equation 2.21 and low-pass filter it, usually from milliseconds to seconds (TC).

- Setting Time: is the time necessary to change the bias plus at least one integration cycle of the lock-in to avoid mixing the signal from two different DC biases.

There is a straight relationship between the integration time, the setting time and the integration time of the lock-in. It will depend strongly on the chosen lock-in amplifier.

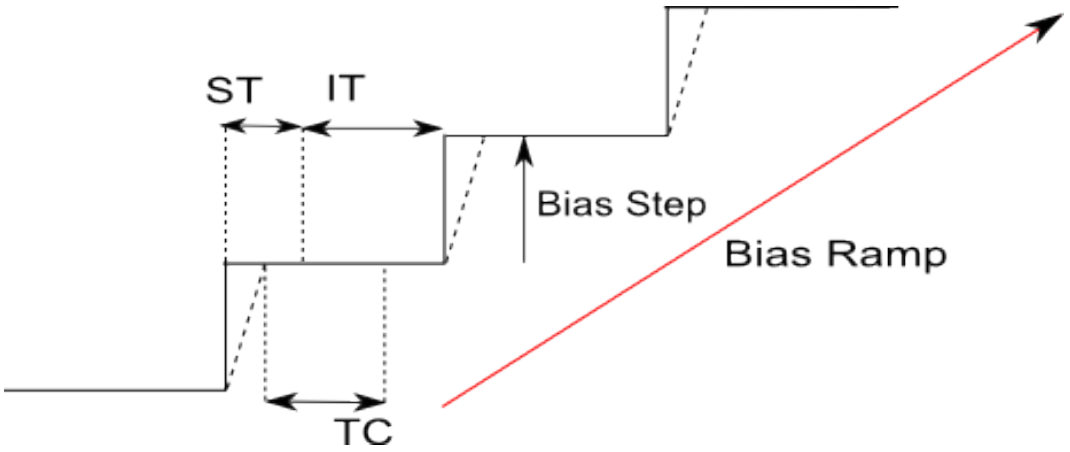

Figure 2.4: Representation of the different parameters on a bias ramp.

The way to check that waiting parameters do not affect the energy resolution is by doing a forward and backward sweep of the bias voltage. If the spectroscopic features do not match, it could be an indication that the parameters are not correct. This mismatch can be affected by by drift. To make sure the drift is not affecting the measurements and that the scan piezos are completely relaxed, the tip is usually kept in tunnelling range for several hours before performing spectroscopy.

The output given by the lock-in dI/dV is given in arbitrary units (V). For the conversion to dI/dV units (which is the conductance, and has units of A/V) it is necessary to take into account the different parameters mentioned before as well as different electronic passive and active components playing a role in the measurement like current divisors, filters, etc. With a divisor on the modulation voltage C_D and a $I-V$ gain of the preamplifier of $10^9 V/A$ conversion would be:

$$\frac{dI}{dV} = d(V)\frac{G(V)}{10V}\frac{1nA}{V}\frac{1}{\left(\frac{V_m(V)}{C_D}\right)} \tag{2.22}$$

where, d(V) is the dI/dV output, G(V) is the gain, 10 V is referred to the full DAC scale and V_m is the lock-in modulation.

There are other aspects that need to be taken into account in order to perform good spectroscopic measurements. Even waiting for several hours before performing spectroscopy and then letting the piezos relax, if the spectroscopy is long enough, a drift in the tip-sample system could cause a shift in the peaks. This could be corrected either by reducing the sweeping time of the whole spectroscopy or waiting even longer for the stabilization of the system. Different electronic parts can cause a spurious displacement of the nominal zero bias value, showing the features of the spectroscopy (peaks, dips, stepsâĂę) on the bias axis where they, in fact, are not really located. This effect can be corrected by plotting different I(V) curves and looking where these curves are crossing (since they should cross at zero bias).

2.1.3 Inelastic electron tunneling spectroscopy (IETS)

An inelastic process is defined as a phenomenon where a particle loses part of its energy in a scattering event. In the case of tunneling junctions, an electron will have enough energy to cause an excitation of energy Δ, opening a new channel in conductance and hence increasing it. An electron crossing the barrier will come out with less energy ($-\Delta$) than in the case of the elastic tunnelling:

$$I_{s\to t} = \frac{4\pi e}{\hbar}\int_{-\infty}^{\infty} dE_t \int_{-\infty}^{\infty} dE_s \rho_t(E_t)\rho_s(E_s) f(E_s)(1-f(E_t))|M_{ts}|^2 \delta(E_s-(E_t+eV_T-\Delta)) \tag{2.23}$$

With the integration of the equation, a similar equation to the elastic case is obtained, with the particularity of the appearance of Δ [17]:

$$I_{s\to t} = \frac{4\pi e}{\hbar}\int_{-\infty}^{\infty}\rho_t(E+eV_T-\Delta)\rho_s(E)f_s(E)(1-f_t(E+eV_T-\Delta))|M_{ts}|^2dE \quad (2.24)$$

The total inelastic current will be calculated subtracting the current tunnelling from tip to sample from the current flowing in the opposite direction:

$$I_T^{in} = I_{t\to s} - I_{s\to t} \quad (2.25)$$

$$I_T^{in} = \frac{4\pi e}{\hbar}\int_{-\infty}^{\infty}|M_{ts}|^2[f(E+eV_T+\Delta)(1-f(E))\rho_T(E+eV_T+\Delta)\rho_s(E)] \\ -[f(E)(1-f(E+eV_T-\Delta))\rho_t(E+eV_T-\Delta)\rho_s(E)] \quad (2.26)$$

Once the total inelastic tunneling current is calculated the elastic current can be added to yield the total current. Two different ways come along when facing the integral and then calculating the first derivative. The first one is doing a simplification of the equation for making it handier with an error lower than 5% [16], the other way is solving the integral analytically [17], [18], which gives for the first derivative:

$$\frac{dI}{dV} = A_e + A_i\left(F\left(\frac{eV-\Delta}{k_bT}\right)+F\left(\frac{-eV-\Delta}{k_bT}\right)\right) \quad (2.27)$$

where A_e is a constant that represents the elastic current, A_i is a constant that gives the intensity of the inelastic current and F is:

$$F(x) = \frac{1+(x-1)e^x}{(e^x-1)^2} \quad (2.28)$$

For the second derivative we have:

$$\frac{d^2I_T}{dV^2} = \frac{Ce^2}{k_bT}\left(\frac{e^x(x-e)+(x+2)}{(e^x-1)^2} - \frac{e^y(y-2)+(y+2)}{(e^y-1)^2}\right) \quad (2.29)$$

where

$$x = \frac{eV+\Delta}{k_bT} \quad (2.30)$$

$$y = \frac{\Delta - eV}{k_b T} \tag{2.31}$$

From the first derivative can be inferred the competition between thermal energy (k_bT) and the energy loss (Δ), which is related to the height of the step. Having $k_bT >> \Delta$ will result in the disappearance of the inelastic step due to the thermal broadening. If $k_bT \approx \Delta$ the step will become broad. If $k_bT << \Delta$ the thermal influence is negligible and the inelastic step will be sharp (step-like).

2.1.4 Atomic Manipulation

It only took nine years from the invention of the STM to achieve successfully atomic manipulation, when D. Eigler and E. Schweizer were able to write IBM with adsorbed Xe atoms on top of a Ni(110) surface [19].

Atomic manipulation can be classified in two different categories: vertical and lateral atomic manipulation.

In the lateral manipulation, the atom is dragged across the surface thanks to the interaction with the tip. The atom is forced to jump among equivalent binding sites of the surface crystal [20, 21, 22]. The force interaction between the tip and the adsorbed atom will be the sum of a perpendicular and parallel component. When the tip moves laterally far away from the atom, the lateral force increases. When the parallel component overcomes the binding energy of the atom to the surface, the atom hops to another atomic site following the tip. This is known as the pulling mode, making us of attracting tip-sample forces. Alternatively, when the binding energy to the surface gets larger, the pushing mode can be used, which makes use of stronger tip-sample repulsing forces.

Conducting surfaces with small lattice parameter are well suited for lateral atomic manipulation and then for most of insulating surfaces where atomic manipulation is required, vertical manipulation becomes an alternative [20, 23].

2.2 Non-Contact Atomic Force Microscopy

Even though STM was invented earlier, AFM has become more popular due to its potential for measuring a wider range of samples compared to STM which is limited to conducting samples. Recently, the inventors of the AFM, Gerd Binnig, Christoph

Gerber and Calvin Quate received the Kavli Nanoscience prize. In STM, the information is gathered through the tunnelling current. In AFM, the information is gathered through the interacting forces between the tip apex and the sample. AFM can be operated in many different ways; in this section we will focus on frequency modulation atomic force microscopy [24] that can be combined with STM. In this way, it is possible to measure forces at the atomic scale [25] in the range of pN.

In this mode, the cantilever is oscillating at its resonant frequency, and the force gradient is detected as a shift in the resonant frequency of the cantilever from the free oscillation value far from the surface. In the absence of external forces and for small amplitudes, the resonant frequency for a cantilever of mass m and stiffness k_0 is:

$$f_0 = \frac{1}{2\pi}\left(\sqrt{\frac{k_0}{m}}\right) \tag{2.32}$$

The qPlus tuning fork design [24] used in this thesis has a stiffness of k=1800 N/m and an effective mass contributed by the tuning fork prong and the tip. This gives a value of the resonant frequency that oscillates between 18 and 30 kHz.

In order to get atomic resolution [26] or even submolecular resolution [27], the tip must be brought very close to the sample. In this regime, the tip is affected by the short range tip-sample forces. The force gradient is sensed by the tip, causes a change in the effective stiffness of the oscillator:

$$f' = \sqrt{\frac{k_0 - \frac{\partial F_{TS}(z)}{\partial z}}{m}} \tag{2.33}$$

where F_{TS} is the force between the tip and the sample. For small oscillations, the shift of the resonant frequency can be approximated as:

$$\Delta f(z) = -\frac{f_0}{2k_0}\frac{\partial F_{TS}}{\partial z} \tag{2.34}$$

The frequency shift oscillation is proportional to the gradient of the tip-sample force. By using cantilevers with high stiffness is possible to measure with subnanometric precision avoiding jump to contact effect.

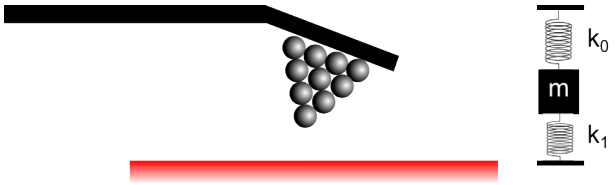

Figure 2.5: Left, representation of an oscillating tip over a sample. Right, schematic sketch that describes the interactions on the short tip-sample distances regime, k_0 is the stiffness of the tuning fork while k_1 is the apparent change in the stiffness due to the gradient of the force in z.

2.2.1 Forces in Atomic Force Microscopy

In this section, we will introduce briefly the forces that play a role in AFM. This will allow for the understanding of the effects that can be observed when $\Delta f(z)$ spectroscopy is performed over the sample of interest. A nice introduction to nc-AFM as well as a detailed description of the interacting forces between tip and sample at the atomic scale can be found in this thesis [28].

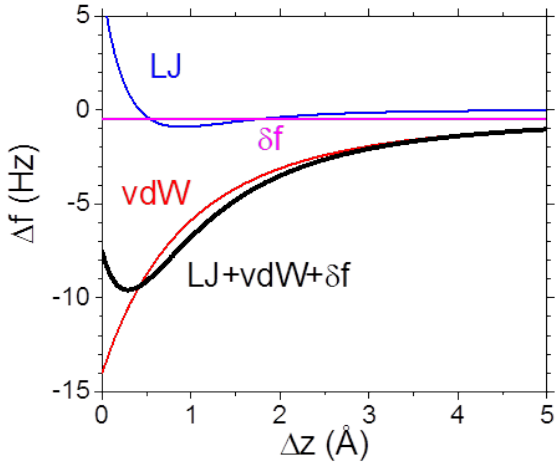

Figure 2.6: $\Delta f(\Delta z)$ model with the different contributions. Chemical contribution, with only influence at very short distances, van der Waals contribution which is long range, capacitive contribution which is taken as a constant as a first approximation and the addition of all the forces which describes an experimental curve.

2.2.1.1 Chemical Forces

Chemical forces play a role when the last atoms of tip and sample are close enough and orbitals overlap. Chemical forces can be described with Lennard-Jones potential which is composed by an attractive and a repulsive term (Fig. 2.6). The attractive term describes the attraction due to the overlap of the wave functions while the re-

pulsive term describes the Pauli repulsion at very short tip-sample distances.

$$E_{L-J}(z) = \varepsilon \left(\left(\frac{z_m}{z} \right)^{12} - 2 \left(\frac{z_m}{z} \right)^{6} \right) \tag{2.35}$$

where ε is the depth of the potential at the equilibrium distance z_m. The chemical force as a function of the distance can be obtained differentiating E_{L-J}:

$$F_{L-J}(z) = -\frac{\partial E_{L-J}}{\partial z} = 12 \frac{\varepsilon}{z_m} \left(\left(\frac{z_m}{z} \right)^{13} - \left(\frac{z_m}{z} \right)^{7} \right) \tag{2.36}$$

2.2.1.2 Van der Waals Forces

Van der Waals forces includes dipole-dipole interactions between the tip and the sample. Dipolar interactions can be itemized in interactions between permanent dipoles, permanent dipoles and induced dipoles and instantaneously induced dipoles. Although the van der Waals potential takes account of dipolar interaction, the additive character of the interactions make them to be a long range force (Fig. 2.6) which needs to be subtracted in case a specific analysis of chemical forces is needed. Considering a given tip-sample distance z, a radius of the tip R, and the Hamaker constant, which is an approximation of the interaction between a ball of radius r and an infinite parallel plate composed by balls of radii r, the approximated equation that describes van der Waals interaction [28] is:

$$F_{vdW} = -\frac{HR}{z^2} \tag{2.37}$$

Therefore, the radius of the tip will play a major role on the van der Waals interaction. Sharp tip termination will mean less van der Waals interaction and hence less masking of the chemical forces while a blunt tip oppositely, will not able to detect chemical interactions.

2.2.1.3 Electrostatic Forces

Electrostatic forces are responsible for the forces generated by an electrostatic potential gradient between the sample and the tip and from all the contributions are those with the longest range of interaction (Fig. 2.6). In the model case of two metallic

plates separated by a vacuum gap, they can be described as [29]:

$$F_{el} = \frac{1}{2}\frac{\partial C}{\partial z}V^2 \tag{2.38}$$

where C is the capacitance which can be related to the dielectric constant, the junction geometry and V is the effective electrostatic potential difference. V is defined as the applied external bias plus the contact potential difference which corresponds to the difference between the work functions of tip and sample $V = V_e + V_{CPD}$.

2.2.2 Kelvin Probe Force Microscopy

Given two metals in electrical contact with different work function, the Fermi levels will align, causing an electron flux from the metal with lower work function to the one with the higher work function. The charges will accumulate on the surface creating thus a space charge and then an effective electric field or potential difference called *contact potential difference* (CPD), which is the difference in work functions of the two metals.

This magnitude can be probed by NC-AFM, with the advantage of having a lateral resolution in the order of the angstrom [30], giving rise to the so-called Kelvin Probe Force Microscopy (KPFM). The difference in work function creates a potential difference between the plates that encloses an electrostatic energy U,

$$U(z) = -\frac{1}{2}C(z)V_{CPD}^2 \tag{2.39}$$

where C is the capacitance, V_{CPD} is the potential difference due to the difference in work functions and z is the tip-sample distance. The force will be the first derivative of the potential with respect z:

$$F(z) = -\frac{1}{2}\frac{\partial C(z)}{\partial z}V_{CPD}^2 \tag{2.40}$$

In KPFM, a potential is applied across the junction changing the force that the tip experiences:

$$F(z) = -\frac{1}{2}\frac{\partial C(z)}{\partial z}(V_{CPD} + V_{Bias})^2 \tag{2.41}$$

When the external bias across the junction equals the difference in work function, the potential across the junction is in the minimum and then the voltage across the junction cancels out the V_{cpd} (Fig. 2.7). Since in Δf measurements we are sensitive to the gradient of the force, the maximum of the parabola described by $\Delta f(V)$ will give us the voltage that is equal to the difference in work function ($\frac{\Delta\Phi}{e}$). A map of this quantity provides a KPFM image.

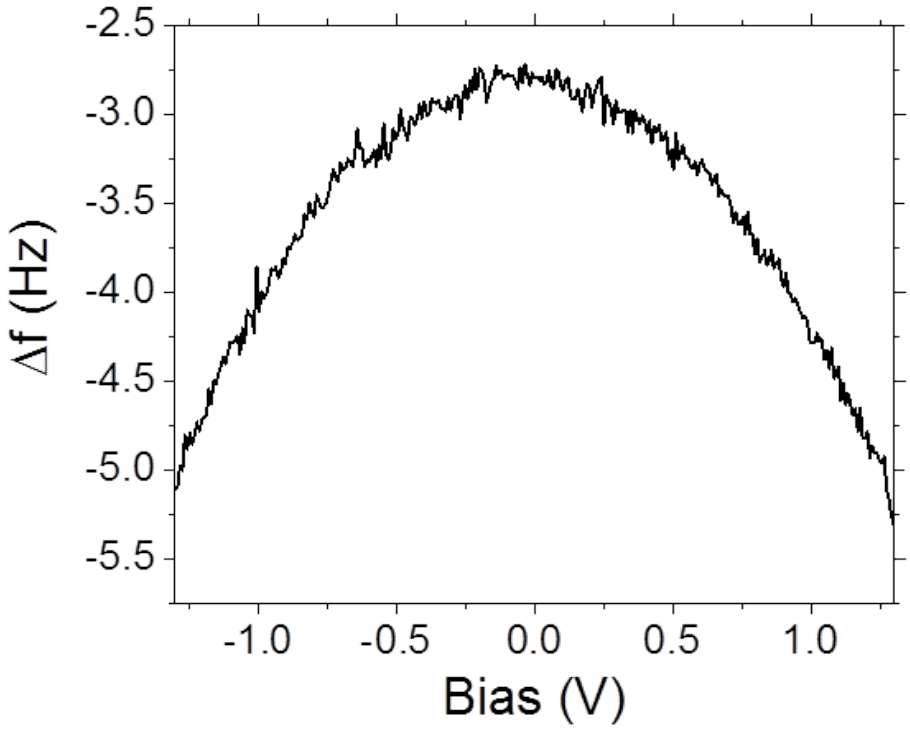

Figure 2.7: Kelvin probe parabola measured over Cu_2N. The maximum of the parabola indicates $-V_{CPD}$ (V_{set}=-1.3 pA, I_{set}=50 pA.

2.3 Experimental Equipment

This section describes the STM systems used in this work. The systems are hosted by the Advanced Microscopy Laboratory in Zaragoza, Spain. It is composed of three different microscopes: an Aarhus STM and a JT STM made by SPECS GmbH and an LT STM made by Omicron. The JT and LT STM systems are operated at low temperatures while the Aarhus is mainly operated at room temperature. All the systems are operated under ultra-high vacuum (UHV) conditions (lower than 2 x 10^{-10} mbar).

2.3.1 SPECS Joule-Thomson STM

The SPECS JT STM [31] is a microscope designed for working at low temperatures, typically in the range of 4.7 K to 1.1 K (which is reached by Joule-Thomson effect). It features a split coil providing an axial magnetic field of 3 Tesla, and allows for the use of spin polarized STM tips. This microscope allows in-situ deposition of adsorbates by molecular beam epitaxy and in-situ tip exchange. The STM coarse motor is based on the Pan design [32], and the compact size and non-magnetic construction make it ideal for low temperature and high magnetic field applications (Fig. 2.8).

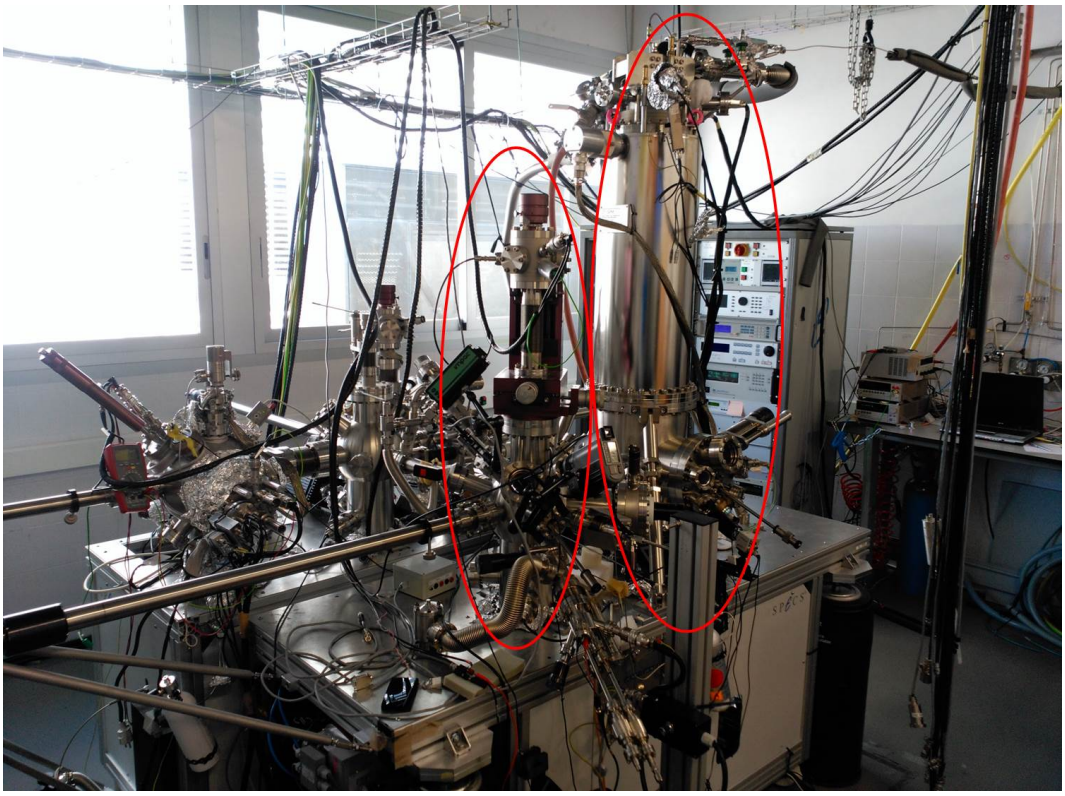

Figure 2.8: UHV system with a SPECS J-T microscope (right) and an attached preparation chamber (left).

The preparation chamber attached to the JT microscope is composed of four molecular beam epitaxy (MBE-4) evaporators, a sputter gun usually used for cleaning crystals, a heater capable of reaching 1300 K, a high-temperature heater that can reach temperatures above 2600 K, a low energy electron diffraction (LEED) and an Auger spectrometer. All these instruments together make a powerful system for cleaning and preparing new samples for their characterization on the microscope. In addition, a second preparation chamber equipped with an e-beam heater and another sputter

gun loaded with N^2 gas allows for the preparatoin of Cu_2N surfaces.

2.3.2 Omicron LT STM

A part of this thesis consist in KPFM, force microscopy and AFM imaging. These results were taken on an Omicron LT system with a tuning fork qPlus sensor mounted on the STM scanner. The system is operated at 4.3 K and in UHV, where the pressure is lower than 1×10^{-10}mbar.

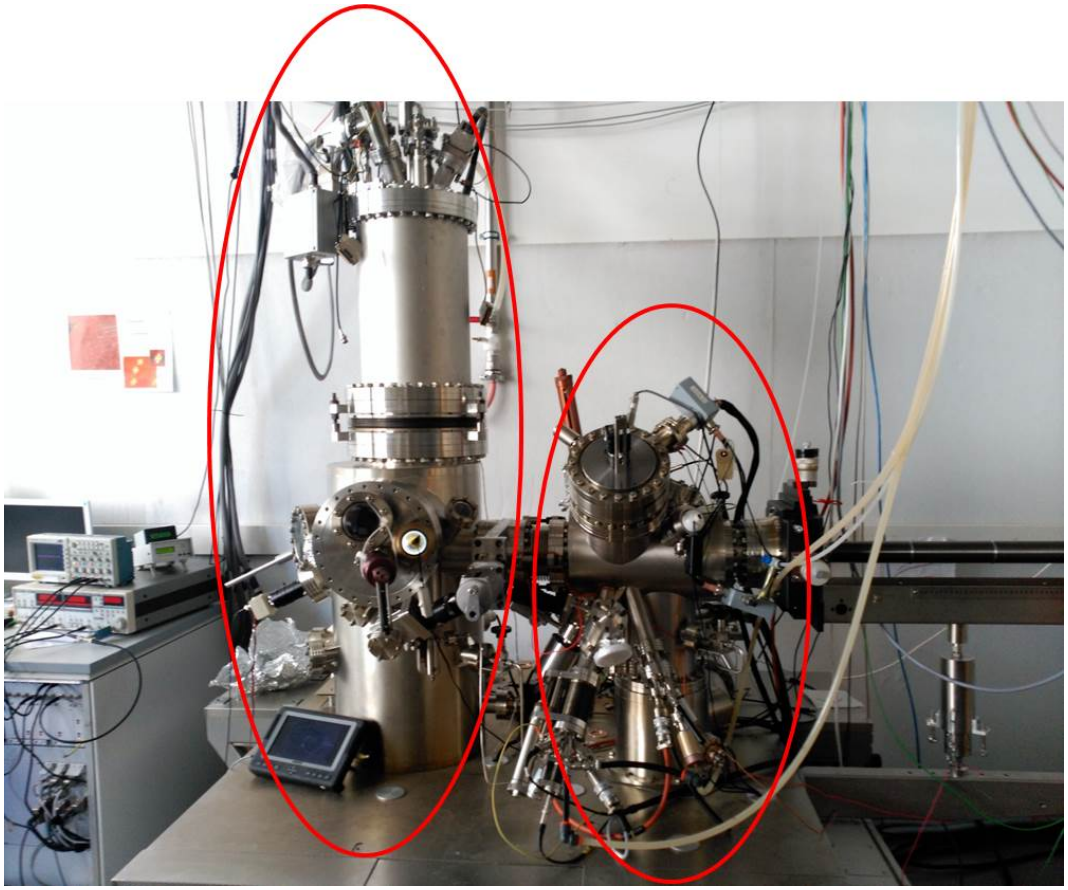

Figure 2.9: UHV system with a Omicron LT microscope (left side) and the preparation chamber on the right side.

The system consists of two chambers which are preparation and STM chamber (Fig. 2.9). The preparation chamber has two sputter guns, one prepared for N_2 sputtering and another one for Ar sputtering for surface cleaning. One sample stage is designed for cold depositions, capable of reaching 77 K (Liquid nitrogen temperature) while in the other one there is a radiative heating. In addition, attached to this chamber there are effusion cells capable to evaporate different compounds (in this case NaCl). The chambers are pumped by an ion pump and a titanium sublimation pump (TSP).

2.4 Determination and Optimization of the Energy Resolution

Obtaining accurate spectroscopy requires a systematic effort, which means the reduction of many sources of noise, vibrational and electronic. For this purpose, an experiment with superconducting Nb tips [33] was performed in the 1 K based JT-STM. The superconducting gap is highly sensitive to the spurious noise sources, resulting in the broadening of the non-thermal dependent sharp spectra corresponding to Cooper pairs. Therefore this is an ideal experiment for optimizing the microscope, minimizing the vibrational level of noise and improving the electronic filtering of the lines.

2.4.1 Introduction

Tunneling junctions have been studied and developed since the end of the 1960s. It has been developed not only for normal junctions but also for superconductive (SC) junctions and also for SC/normal junctions. Extensive reviews have been written explaining these phenomena [34].

This system has been transferred successfully to STM [33], where the SC behavior can be either in the tip, in the sample or in both. One of the advantages of this system is that it can be used to determine the temperature of the microscope or rather its effective temperature (and hence its inherent noise) by deconvoluting the acquired spectroscopy. This is particularly useful for minimizing the noise and knowing the real working temperature of the microscope. In this experiment spectroscopy will be performed with a SC Niobium tip over an Au(111) and W(110) sample.

2.4.2 Theory

In the case of a superconductor, according to the BCS theory, the density of states has a gap in the spectrum of the size of Δ and singularities in the DOS at $E = \pm\Delta$.

$$\rho_s(E) = \begin{cases} \frac{\rho_n(E)E}{\sqrt{E^2-\Delta^2}} & |E| \geq \Delta \\ 0 & |E| < \Delta \end{cases} \tag{2.42}$$

where ρ_s is the DOS of the tip in this case (Figure 20).

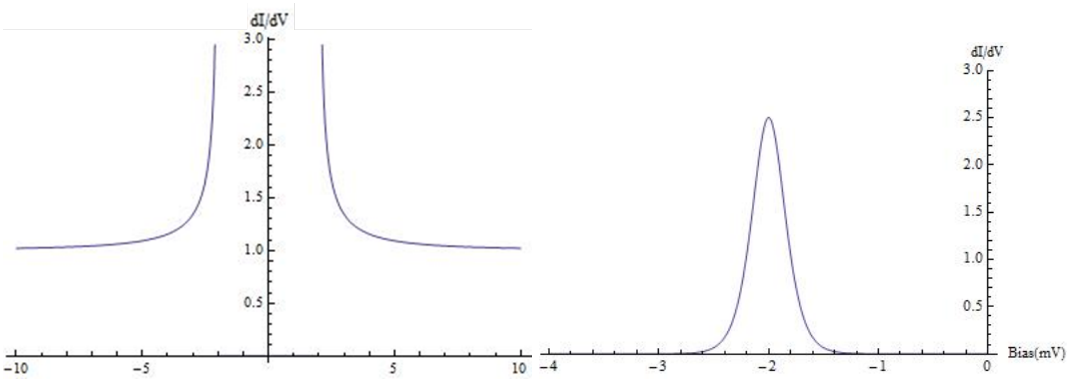

Figure 2.10: (a) Superconducting DOS. (b) Kernel function.

At first approximation, since the SC gap manifests at the fermi level (low bias regime), the density of states in the sample, which is not SC will be constant, and thus can be removed from the integral that describes the tunnelling current 2.12.

$$I \propto \int_{-\infty}^{\infty} \rho_s(E)[f(E+eV) - f(E)]dE \tag{2.43}$$

The DOS can be extracted by just taking the first derivative of I respect to V:

$$\frac{dI}{dV}(V) \propto \int_{-\infty}^{\infty} N_s(E)K(E+eV)dE \tag{2.44}$$

where K is the derivative of the Fermi function, which is also known as the kernel function (Figure 2.10).

$$K = \frac{\beta e^{[\beta(E+eV)]}}{\left(1+e^{[\beta(e+eV)]}\right)^2} \tag{2.45}$$

with $\beta = \frac{1}{kT}$. The obtained dI/dV at any point of the sample without defects or impurities will be a convolution of the superconducting DOS and the kernel function. The final shape will depend on the temperature of the microscope (T), the superconducting gap (Δ) (which is highly dependent of the tip) and the noise, that includes external noises as well as the modulation voltage (V_m), resulting in a U-shape function (Fig. 2.11).

The effective temperature can be calculated as a quadratic sum of real temperature

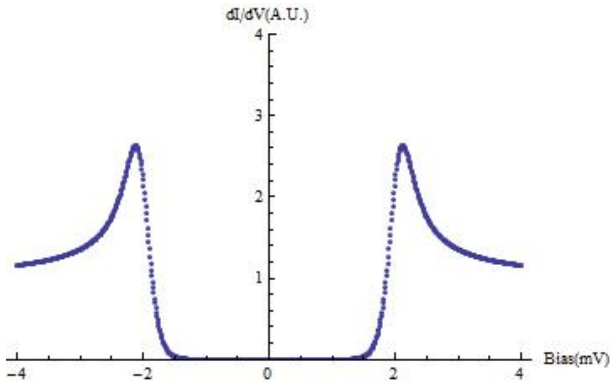

Figure 2.11: Theoretical SC DOS for a SC gap of 2mV and a temperature of 1.16K.

and the thermal noise:

$$T_{eff} = \sqrt{T_{noise}^2 + T_{real}^2} \tag{2.46}$$

2.4.3 Experiments

2.4.3.1 Sample preparation

Mechanically sharpening of Nb tips in ambient conditions presents two different problems. Oppositely to Pt/Ir, Nb wire has poor ductility. Mechanically Nb sharpened tips show a non-microscopically sharp apex. Secondly, oxidation of Nb tips apex occurs after the etching. Since it is necessary to have pure Nb in order to have superconducting properties, it would be desirable to do this process in vacuum conditions. In-situ cleaning of the tip to remove the oxide layer in UHV was tried, but it results in poor superconducting gaps much smaller than the bulk value for Nb. This is probably due to the Ar inclusion at the tip during the sputtering process.

Therefore to improve the performance of Nb tips, in-situ Nb tip cleavage in UHV conditions was performed. The wire was mounted on a tip holder and cut in a 45° angle with a razor. When the wire was weak enough the whole system was put in UHV conditions and then stretched until it was split in two different parts. In this way the tip apex is free of oxide.

Noise-improvement measurements

Improving the tip by high current pulses, as well as filtering the bias line, made a big difference. In addition, more tests were performed on the JT setup. All electrical

lines (scanner, piezo motors, temperature sensors and current feedthrough for the superconducting coils) are filtered by passive pi-filter with 100 kHz cut off frequency. These experiments were performed at the base temperature of the system of 1.16 K. Tests listed in Table 2.1 points did not make any significant change on the SC gap:

Filtering piezos and temperature. lines with pi-filters.	Putting a DC bias divisor.
Wrapping with aluminium foil every JT input/output and cable.	Switching off JT temperature controller.
Switching off turbo and ion pumps.	Switching off any electronic or mechanic device inside the room.
Switching off ion gauges.	

Table 2.1: Tests performed in order to improve the signal/noise ratio.

SC Gap improvement through tip treatment with high currents and bias pulses

Besides the temperature, other factors can affect the SC Gap such impurities in the tip apex or the angle of the tip at a nanoscopic scale. At the time of the characterization, there was no possibility of applying 100 V on the tip-sample system and hence performing field emission. However, with 10 V applied to the tip-sample system, high currents were reached (larger than 100 nA) which in any case changed the tip completely, helping to remove impurities.

In summary, the SC Gap was improved after consecutive treatments of the tip (Bias pulses and high current scans). These treatments removed impurities and oxide from the tip, having then a pure Nb tip and probably, a sharper tip.

In practice, this can only be checked through many tip-sharpenings noticing no improvement in the gap with subsequent treatments.

After several bias pulses, no improvements were shown on the SC Gaps (Figure 2.12).

Gap improvement through filtering the bias line

In a RC filter, also called low pass filter, the cutoff frequency will be determined by the resistance and capacitance following this relationship:

$$f_c = \frac{1}{2\pi RC} \tag{2.47}$$

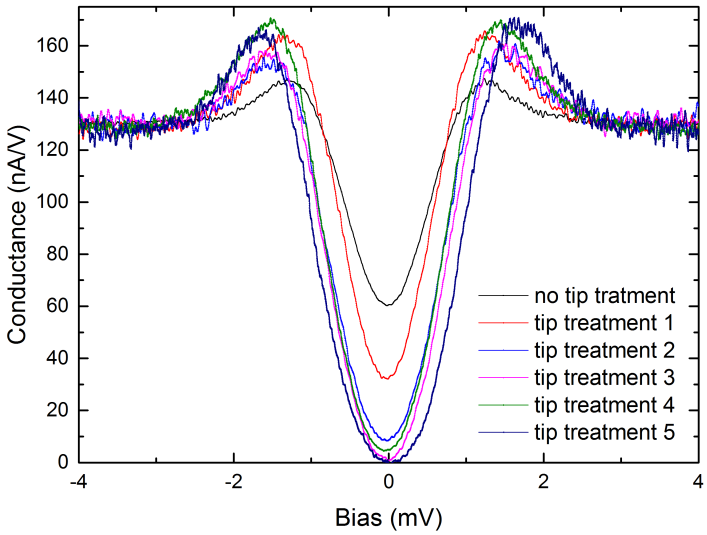

Figure 2.12: .Improvement of the SC Gap through the different tip treatments. The spectroscopies were taken in the following conditions: V=-4 mv, I=800 pA, Gain=10 mV, Vm=50 μV (rms), TC=50 ms.

a higher resistance or capacitance will decrease the cutoff frequency.

There is a large difference between the SC gaps, with no RC filter, with a 17 kHz RC filter after tip improvement and with a 1.7 kHz RC filter (Figure 2.13) on bias line.

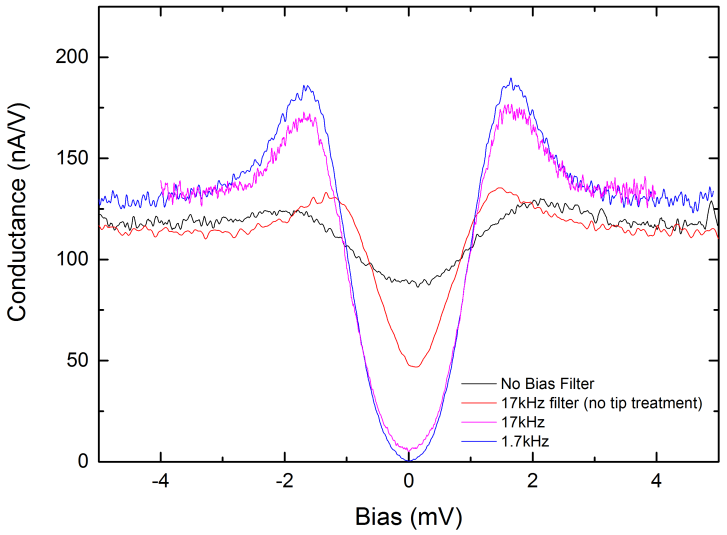

Figure 2.13: Spectroscopy measurements of SC Gap without filtering bias line and with two RC filters with a different cutoff frequency. The spectroscopies were taken in the following conditions: V=-5 mv, I=800 pA, Gain=10 mV, Vm=50 μV (rms), TC=50 ms.

It can be noticed that a significant increase in terms of resolution (the slope is higher, which makes the gap sharper) is obtained with the filter in place.

A more restrictive RC filter with f_c=300 Hz was inserted after tip treatments (voltage pulses and at high currents), in order to increase the resolution; this produced only a slight difference. 1.7 kHz configuration was kept for the high resolution spectroscopy performed throughout this thesis.

After having the system in the best possible conditions, spectroscopy was performed with different bias modulation to find any possible difference in the SC Gap (2.14).

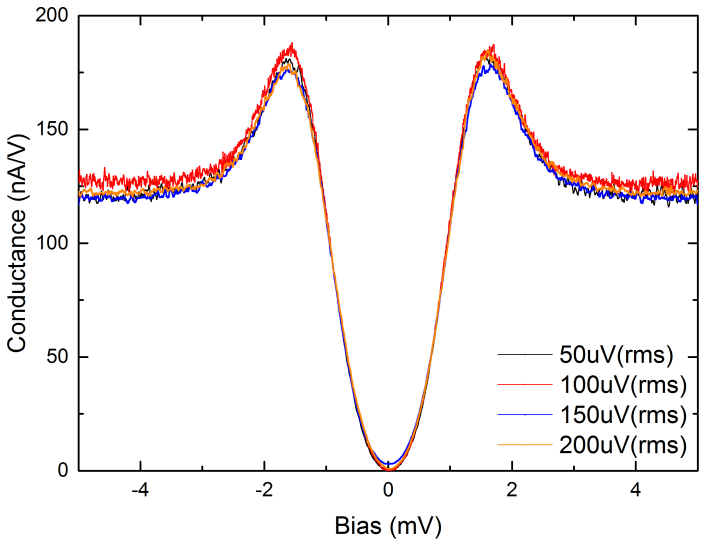

Figure 2.14: Spectroscopies taken with different bias modulation. The spectroscopies were taken in the following conditions: V=-4 mv, I=800pA, TC=50 ms. For each curve the gain was adjusted to obtain the largest possible signal.

As seen in figure 2.14, no differences were found through the different bias modulations below 200 μV with the same conditions, while above this value systematic broadening is observed.

2.4.3.2 Effective Temperature Calculation

As it has been mentioned before, theoretical fits based on Teadrow-Mersevey theory can be performed in order to find the SC gap tuning the both SC gap and effective temperature. Once the fit matches and hence the gap is found, the effective temperature can be inferred from them.

Figure 2.15 shows an improvement in terms of resolution through the different theo-

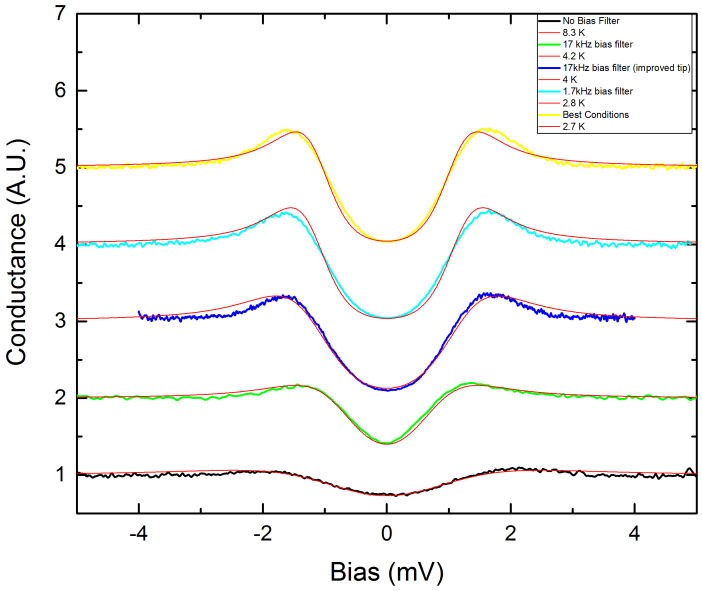

Figure 2.15: Experimental SC gaps adjusted with a theorical effective temperature curve (red). Every plot is labelled with the bias filter attached, the effective temperature and the special experimental conditions. The curves are stacked for more clarity.

retical fits. The effective temperature goes from 8.3 K to 2.7 K by essentially attaching a low-pass filter on the bias line. On the other hand, as it was expected, the tip improvement increased the size of the SC Gap.

Once the effective temperature is inferred from the fits, the calculation of the energy limit resolution of the STM is straightforward by just multiplying by the Boltzmann constant. The energy limit resolution is hence 230 μeV.

From the equation 2.46 the electronic broadening can be deduced by just solving T_n, giving a value of 210μeV.

SC Gap Temperature Dependence

One of the capabilities of the system is the possibility of varying the temperature of the microscope in a controlled manner. The evolution of the SC Gap with the temperature can give useful information, like the nature of the noise in the microscope (since an electronic noise should keep constant with the temperature). The evolution of the SC Gap can also give useful information about the quality of the SC tip. A critical SC temperature which matches the temperature reported on the literature (9.2 K) [35]

would indicate a pure Nb tip, while a lower value would indicate that the tip contains some impurities or finite size effects that interfere with the superconductivity.

These curves can give useful information about the inherent noise of the microscope. By fitting to theoretical curves the effective temperature can be calculated (Figure 2.16).

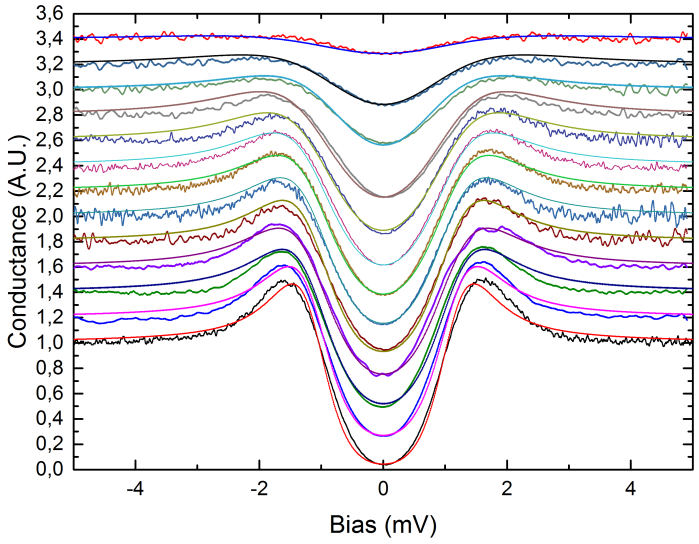

Figure 2.16: Variation of the SC Gap with the temperature and the adjusted theoretical curves. The temperature goes from 1.18 K up to 7 K. Effective temperature values go from 2.7 K to 10 K and the SC Gap goes from 1.13 mV to 0.65 mV.

Once retrieved the effective temperature from the data shown in fig. 2.16 it is possible to compare with the real temperature measured independently (Fig. 2.17). This will determine the nature of the noise. A linear tendency where an increase of 1 K on the real temperature is observed. The same equivalent increase would indicate a constant electronic broadening while other deviations from the linear trend could indicate a source of mechanical noise.

The linear tendency of the graphs up to 5.5 K indicates a constant base noise. The temperature increase does not affect the resolution of the microscope beyond the temperature contribution. The exponential increase beyond 6 K could be related to the difficulty of the system to keep the temperature completely stable or the bubbling of liquid He contributing to mechanical excitations.

At the same time the SC Gap decrease can be plotted as a function of the temperature (Fig. 2.18). With the equation 2.50 it is possible to fit the curve to the experimental

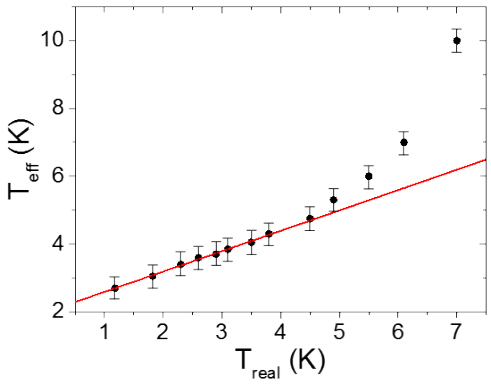

Figure 2.17: Extracted effective temperature from fitted SC gaps vs real temperature measured on the STM stage.

points and obtain the critical temperature of the niobium [36], which will be the intersection with the x axis.

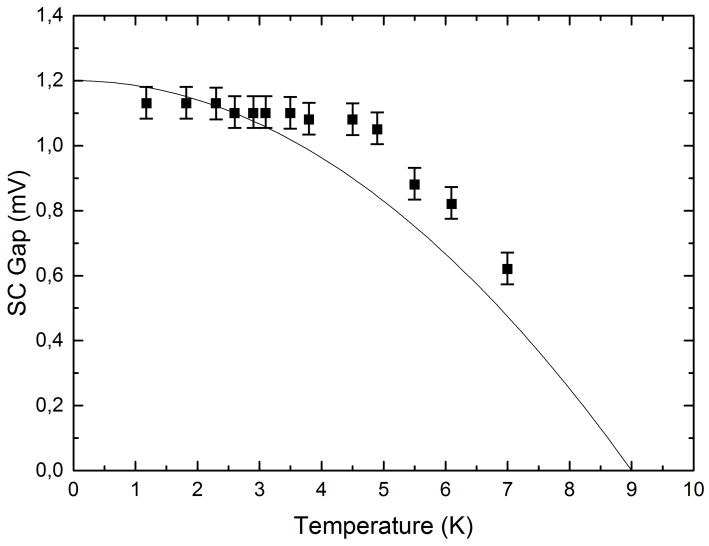

Figure 2.18: Predicted (solid line) and measured (black squares) superconducting gap energy vs. temperature.

$$H_c(T) = H_c(0)\left[1 - \frac{T^2}{T_c^2}\right] \tag{2.48}$$

where H_c is the critical magnetic field, T the temperature and T_c is the critical temperature.

The critical magnetic field can be related with the superconducting gap [37]:

$$\Delta E_{SC}(T) \approx g H_C(T)^2 \tag{2.49}$$

By substituing the equation 2.48 into 2.49 is possible to find the following relationship:

$$\Delta E_{SC}(T) \approx g H_C(0)^2 \left(1 - \frac{T^2}{T_C^2}\right)^2 \tag{2.50}$$

The fit roughly adjusts for a critical temperature of 9 K.

2.4.3.3 Conclusions

The noise analysis is effective and it is mandatory when the experiment requires obtaining small signals or features close to the resolution limit, like inelastic steps or small features at Fermi level.

It should be remarked that is also important how the tip is made. For systems where it is not possible to set high bias and hence, there is no real possibility to perform field emission, tip cleaving in UHV makes a difference, since it is only necessary to make a few voltage pulses to have a good SC gap. By this method the very end of the tip is not oxidized and it is only necessary to get rid of some impurities and a proper shape or the tip apex.

In addition, with this method, the major sources of noise have been debugged, and we have concluded that the major source of noise is not mechanical, which indicates that the system is well decoupled from the environment. Figure 2.17 demonstrates that the major source of noise at low temperatures is electronic. This can be significantly suppressed by properly filtering the different electrical lines that go into the JT system. Through the different tests it was observed that filtering the piezoelectric line and the thermometry line that go towards the JT head did not play a major role in decreasing the noise. In contrast, filtering the bias line by just a simple RC filter made a big difference.

It has been demonstrated that filtering properly the bias line is mandatory to have a good performance in terms of noise level. Moreover due to the noise contribution, modulating with less than 200 μV will not make any difference. Therefore a design of

Procedure.	Noise contribution.
No filter	700 μV
17 kHz filter	340 μV
Tip treatments	330 μV
1.7 kHz filter	240 μV
1.7kHz filter + Best possible conditions	210 μV

Table 2.2: Comparison of the different methods followed to improve the signal/noise ratio.

a better filter is required to decrease the noise level and hence having the possibility to modulate with 50-100 μV (meaning the resolution for the nominal base temperature is reached).

2.4.3.4 Design of a New Filter

Simple RC filters have been proven not to be good enough for filtering the bias line and then reaching the limit resolution of the microscopy. One of the major drawbacks of these filters is the inability to filter the radio frequency (RF) noise inherent in ambient conditions due to their design since it is impossible to separate the filter in a dirty side and a clean side grounded to the whole microscope system. If the experiment requires reaching the limit resolution of the microscope, filtering RF signals is mandatory and a design formed by a clean and a dirty cavity is needed (Figure 2.19).

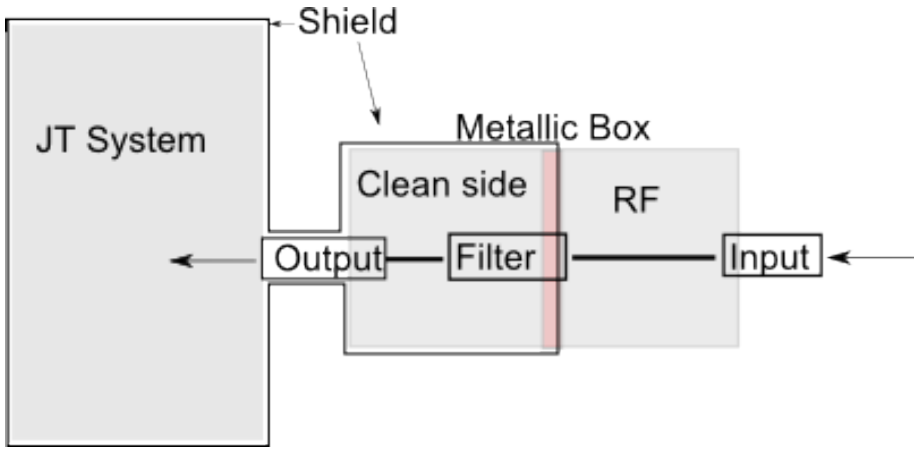

Figure 2.19: Schematic draw of a RF filter.

Due to its characteristics, a pi-filter is an appropriate choice since it can be separated from the dirty side and screwed to the copper plate. The chosen Pi filter (Tusonix 4206-001LF) has a cutoff frequency of the order of MHz but by adding a proper

resistance in series it can work as an effective low-pass filter. A pi-filter with a capacitance of 5.5 nF and a resistance in series of 100 kOhm will give a cutoff frequency of around 900 Hz. By adjusting the transfer function (Equation 2.52) to the measured points, the cutoff frequency (921 Hz) can be easily calculated (Figure 2.20). However this aggressive filtering of the line showed a clear disadvantage. Since the 100 kOhm resistor can be close to the tunnel junction impedance in some spectroscopic measurements, there will be a non-negligible voltage divider effect, with a part of the voltage being dropped across the resistor and part across the tip-sample junction.

The RC circuit can be considered as a voltage divider:

$$V_{out} = \frac{1}{j\omega RC + 1} V_{in} \tag{2.51}$$

where the modulus will be:

$$\frac{V_{in}}{V_{out}} = \frac{1}{\sqrt{1 + (2\pi RC\nu)^2}} \tag{2.52}$$

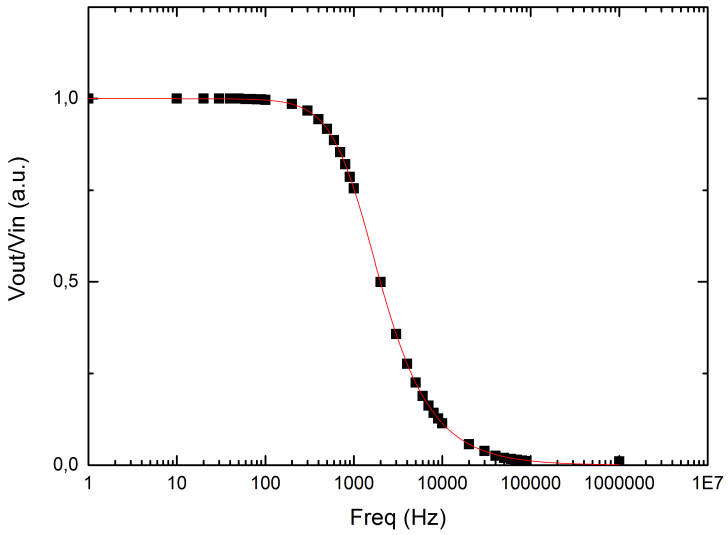

Figure 2.20: Adjusted transfer function to measured points on a PI+R filter.

By this method it should be possible to reach the maximum energy resolution of the microscope.

2.5 Sample preparation

2.5.1 Cu(001)

The Cu(001) surface was cleaned in a preparation chamber by repeated cycles of Ar^+ sputtering with an energy of 1 kV and a pressure of $1x10^{-6}$ mbar and consecutive annealings at around 500 °C (Figure 2.21).

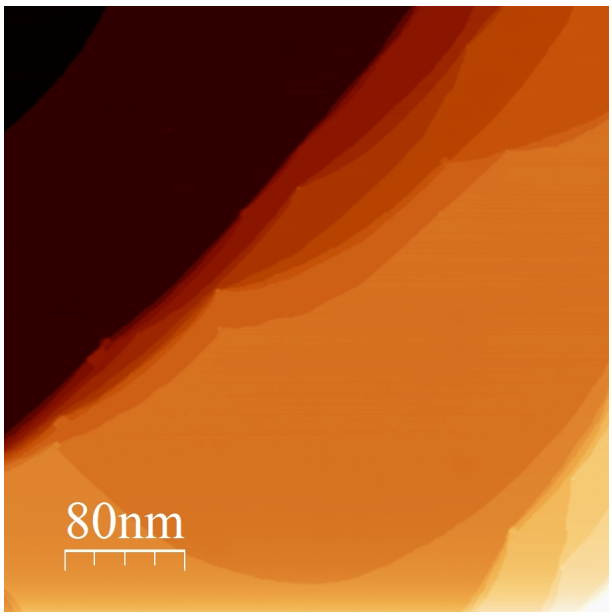

Figure 2.21: Clean Cu(001) surface after repeated cycles of sputtering and anneling (V_{set}=0.5 V, I_{set}=0.5 nA).

2.5.2 Copper Nitride

Copper nitride (Cu_2N) is a monoatomic insulating layer where a N row is positioned between 2 Cu rows. Early experiments with Cu(001)[38, 39] showed that by sputtering the surface with N_2 and then annealing it at around 300 °C, self-assembled Cu_2N can be grown (Fig. 2.23).

The coverage of Cu_2N can be controlled by varying the sputtering time or N_2 pressure. Increasing one of these two parameters will result in a larger coverage of Cu_2N. Increasing the temperature and time of annealing will result in larger and more regular islands only if the temperature is not high enough to desorb the sputtered N_2.

Cu_2N has shown interesting properties. The insulator properties (4 eV gap) have been used to decouple the magnetic moment of atoms from metallic surfaces reducing the hybridization and allowing spin-flip inelastic transitions of single atoms [40, 41, 42]

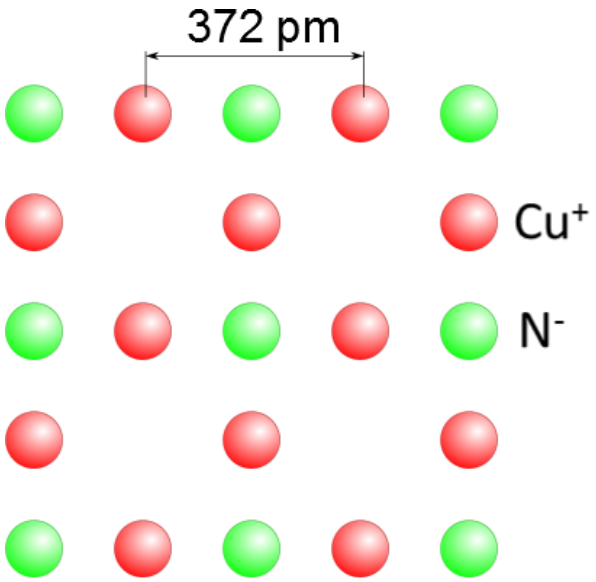

Figure 2.22: Cu_2N structure with N atoms (green dots) intercalated every two rows of Cu (red dots).

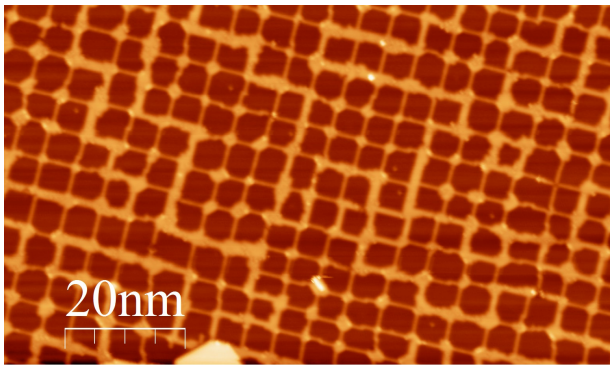

Figure 2.23: Self-assembled Cu_2N in a grid mode. Dark squares are Cu_2N while bright rows is bare Cu(001)(V_{set}=100 mV, I_{set}=200 pA).

and observing Kondo excitations with a very low Kondo temperature [43].

In addition, copper nitride can be used as a template for the growth of organized nanostructures. The different sticking rates of bare Cu and Cu_2N and the grid growth make it perfect for self-assembled grid structures [44, 45].

2.5.3 Sodium Chloride

Sodium chloride (NaCl) has attracted the interest of researchers as an atomically thin insulator since the end of the 1990s [46]. Its bilayer growth reveals a weak interaction with metallic substrates, making it appropriate to grow over very different kind of metals. Due to its large insulator gap, NaCl is a good system for decoupling molecules from the metallic substrate, for example enabling imaging molecular or-

bitals on isolated molecules [47]. Another interesting aspect is the possibility for charging one single atom adsorbed on the top of the layer by modifying the neighbouring structure [48].

For NaCl evaporation, a home made evaporator was used (Figure 2.24). The evaporator consists of a button heater (internally wired boron nitride resitive heater), a copper crucible where the NaCl is introduced and different pieces that allows the current flowing without shortcuts. The NaCl was bought from Alfa Aesar with a purity of 99.999%. The copper head was heated up to 580 C. The deposition rate is extremely dependent of the temperature above the sublimation threshold and thus, the coverage can vary from less than a monolayer to more than two monolayers in the range of tens of degrees with the same deposition time.

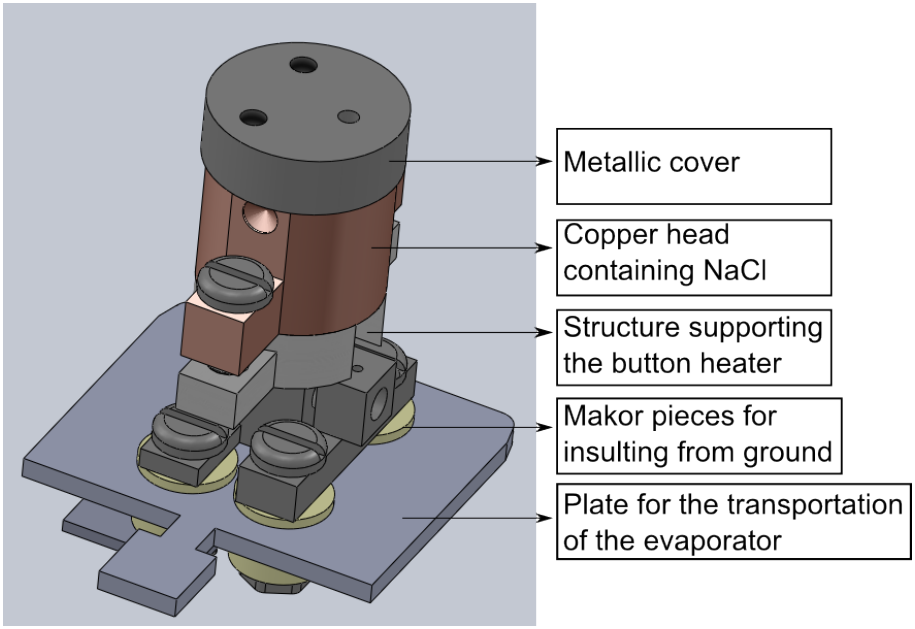

Figure 2.24: Transportable evaporator for evaporation of NaCl.

The NaCl deposition was characterized by STM imaging the NaCl over Cu(001) and observing bilayer and trilayer formation (Figure 2.25).

Figure 2.25 shows an NaCl deposition over Cu(001) at RT for approximately 30 s. Most of the surface covered by bilayer patches of NaCl, altough small areas of third layer of NaCl are also spotted.

2.5.4 Single Atom Deposition

Single Co atoms were deposited in situ onto the NaCl/Cu_2N substrate from an electron beam evaporator loaded with a high purity Co rod focused at the STM sample

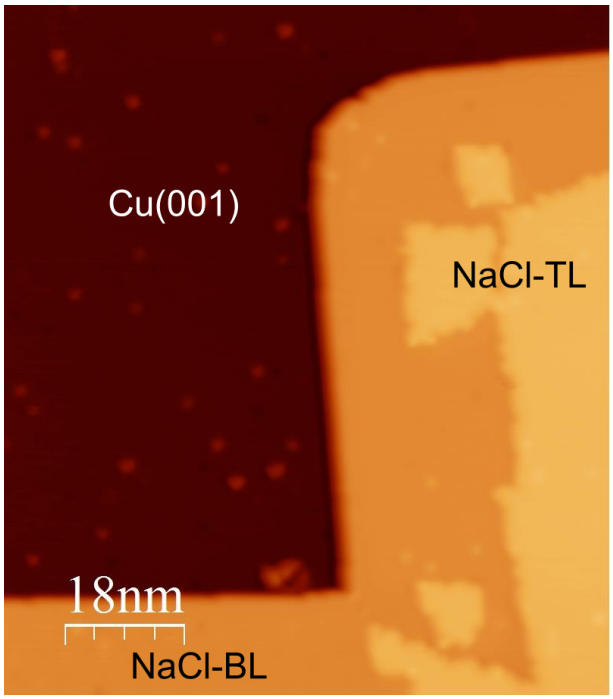

Figure 2.25: STM image taken over an area partially covered with NaCl(V_{set}=0.6 V, I_{set}= 100 pA).

stage at $T < 5K$, preventing atoms diffusion. The evaporation flux was increased until 10 nA was reached and then kept constant. For this flux a potential bias difference of 800 V was applied between the rod and the filament and the filament current was increased until the desired evaporation flux was reached. The evaporation time varied from 10 to 30 seconds depending on the desired coverage.

Chapter 3

Growth and Characterization of Ultrathin Stacks of Polar Insulators

3.1 Abstract

Interactions at the atomically precise interface between different polar materials can trigger a variety properties, from induced ferroelectricity [49] to superconductivity [50, 51]. With two dimensional materials like graphene and transition metal dichalcogenides, it is now possible to create heterostructures of atomically thin van der Waals bonded materials [52]. In this chapter, we combine the concept of van der Waals materials and ultrathin polar insulators by stacking atomically thin layers of sodium chloride (NaCl) on copper nitride (Cu_2N). Because of electrostatic interactions, the polar NaCl adopts the lattice parameter of Cu_2N, compressing it by 7%. Furthermore, the interface between NaCl and Cu_2N modifies the local density of states versus NaCl on top of Cu(001), avoiding hybridization and charge transfer in the NaCl layer. This new class of polar insulating interfaces represents a promising way to engineering the structural and electronic properties of atomically thin polar layers. The material presented in this chapter is being submitted for publication in a research journal.

3.2 Introduction

A wide range of properties can be tuned in polar oxides (from simple binary compounds to more complex transition metal oxides) due to their extreme sensitivity to structural distortions. These phenomena can include magnetism, ferroelectricity [49] or high temperature superconductivity [50, 51]. One way to control the structural

distortions, which can induce an out of plane dipole, is through epitaxial strain, when a certain material is grown on a substrate with a different lattice parameter. The polar nature of these materials comes into play, interacting electrostatically and hence, causing electrostatic coupling. Since these properties manifest over a critical thickness, many efforts have been made in the control and stabilization of polarization and rumpling at the ultrathin regime [53].

Nonetheless, the growth of the compounds as well as detection of these new phenomena at the interface has remained relatively challenging. It is necessary to achieve accurate control on the layer growth to produce atomically precise interfaces. At the same time, high sensitivity equipment is necessary to detect the weak signal coming from the interaction between these ultrathin compounds, which may produce new emergent phenomena. In the same way, progress on different materials has allowed not only to produce 2D-materials such as graphene, boron nitride or silicene [54, 55, 56] but to study in depth their different properties. Breakthrough advances have shown that it is possible to stack these 2D-materials, which interact through van der Waals forces, giving rise to new collective phenomena [52]. However, none of this work has been oriented on the study of stacked atomically thin insulating layers and their interactions. Furthermore, the insulating nature of most of the different polar compounds has prevented the study of emergent phenomena by STM.

Over the past two decades, different insulating layers in the ultrathin regime have been employed due to their capability to decouple metallic substrates from the system of interest. Many of these insulating layers have been studied with STM, including aluminium oxide (Al_2O_3) on NiAl, where it was possible to decouple from the metallic substrate single atoms of Pd [57]; dielectric insulators like NaCl with a broader bandgap [48, 58, 59, 60]; nitrides like Cu_2N [38]; and polar oxides like MgO [61] . These insulators have been used extensively as decoupling layers to isolate electronic and magnetic properties of adsorbed atoms and molecules. Limiting the size of the insulators to a few atomic layers enables the study of the electronic properties due to the possibility of tunnelling through them into the underlying metal substrate.

Past experiments have shown that it is possible to force NaCl to place in energetically favourable binding sites by depositing it in a charge modulated surface [62]. In addition, theoretical predictions have suggested that straining binary rocksalt compounds

could lead to new properties, including ferroelectricity [63, 64]. As an analogy to van der Waals materials, NaCl is stacked on Cu_2N with atomic precision, confirming a new material with the opportunity to study with STM which will be shown in the following sections.

3.3 Sample Preparation

Once Cu_2N is prepared, by the method described in the previous chapter, NaCl is deposited on top of the sample with Cu_2N.

NaCl can grow monolayer (ML), bilayer (BL) and trilayer (TL) over Cu_2N. One of the characteristics of depositing NaCl on Cu_2N is the growth of a single layer of NaCl. The quantity of NaCL-ML found on a Cu_2N/Cu(001) substrate depends on the deposition rate of the NaCl over the sample. High deposition rates (approximately 3 ML per minute) will result in high coverage of NaCl-ML (Fig. 3.1a) while low deposition rate (approximately 1 ML per minute) will result in the formation of NaCl-BL and TL (Fig. 3.1b). Temperature dependence in the NaCl evaporation is noticed. NaCl deposited on top of Cu_2N at room temperature (RT) will result in more homogeneous islands (NaCl covering the whole Cu_2N area) (Fig. 3.2a). NaCl deposited on Cu_2N at low temperature (e.g. on a sample that has been immediately removed from the low temperature stage of the LT-STM) will result in the formation of irregular islands of NaCl (Fig. 3.2b).

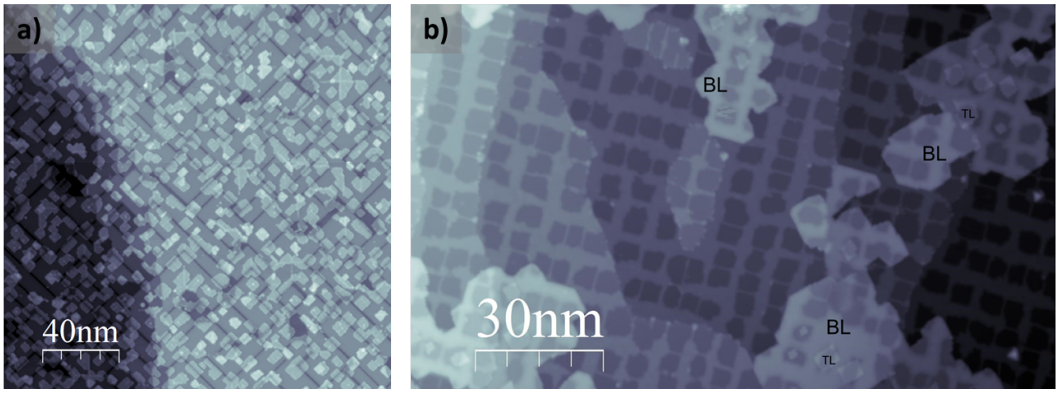

Figure 3.1: High deposition rates vs low deposition rates. a) NaCl deposited onto Cu_2N/Cu(001) at 3 ML per minute. High quantity of NaCl-ML observed and a few islands of NaCl-BL. b) NaCl deposited onto Cu_2N/Cu(001) at 1 ML per minute. Only NaCl-BL and TL observed. (V_{set}=-1.3 V I_{set}=50 pA).

NaCl-BL can exist in large areas across both Cu(001) and Cu_2N, regardless of the

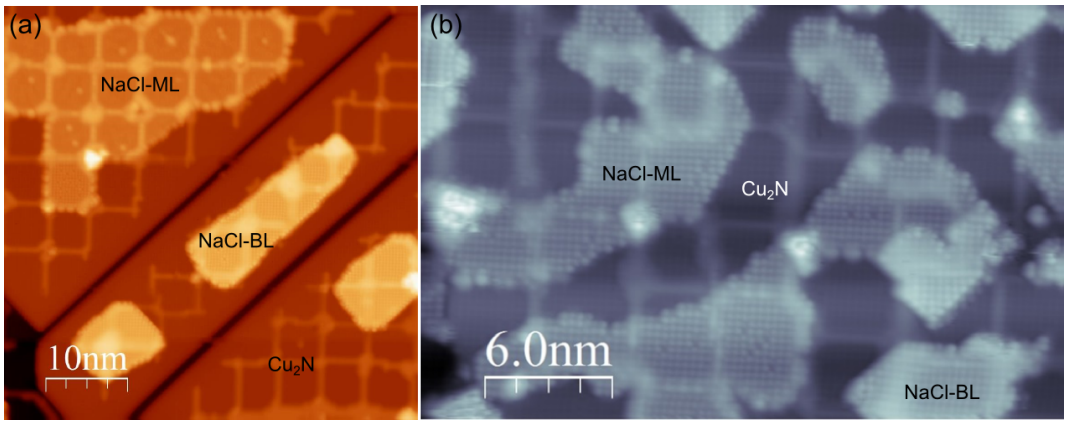

Figure 3.2: Comparison between NaCl deposited on RT Cu_2N and LT Cu_2N. a) NaCl deposited with substrate at RT. The borders look regular and NaCl (specially in the ML) is mostly covering the patches. b) NaCl deposited with substrate at LT. The borders are not so regular and NaCl is not covering completely the Cu_2N patches. (V_{set})=-1.3 V I_{set}=50 pA)

separation distance between Cu_2N regions.. This fact indicates that the formation energy in both cases must be similar since large differences in formation energy (defined below) of NaCl on top of Cu_2N and Cu(001) would not allow the formation at the same time on both substrates.

To further confirm these observations, the electronic and geometric structure of NaCl on Cu_2N/Cu(001) was investigated by density functional theory (DFT) calculations performed by Mats Persson using the Vienna ab-initio simulation program (VASP) [65]. The electron-ion-core interactions and the exchange-correlation effects were treated using the projected augmented wave (PAW) method [66] with a plane-wave, kinetic energy cut-off of 400 eV, and the optB86B version of the van der Waals density functional [67, 68, 69, 70], respectively. The Cu(001) surface is represented in a super-cell by a six layer slab with a c(12x12) surface unit cell and a 16.2 Åvacuum region. During the geometry optimization, the atoms in the bottom two layers were constrained at their bulk positions with a calculated lattice constant a of 3.60 Å(the value for bulk Cu) and a = 3.72 Å(the value for Cu_2N), and consistent results were obtained in both cases; the positions of the remaining atoms were relaxed until all forces were less than 0.02 eV^{-1}.

Formation energy of n monolayers (nML) per NaCl dimer is defined here as

$$E_f = [E(NaCl(nML)/Cu_2N/Cu(001)) - E(Cu_2N/Cu(001)) - nE(NaCl)]/n \quad (3.1)$$

while the film adsorption energy in the surface unit cell is defined as:

$$E_{ad} = E(NaCl(nML)/Cu_2N/Cu(001)) - E(Cu_2N/Cu(001)) - E(NaCl(nML)) \tag{3.2}$$

The formation energy of NaCl-ML, and NaCl-BL on top of Cu_2N and Cu(001) are very similar (Table 3.1). For the calculation of the energies, four different adsorption sites were considered: Cl on top of Cu (Fig. 3.3a), Cl on bridge sites (Fig. 3.3b), Cl on top of N (Fig. 3.3c) and Cl on top of Hollow sites (Fig. 3.3d). As it will be further analysed in the following section, the most stable configuration is placing Cl atoms on top of Hollow sites.

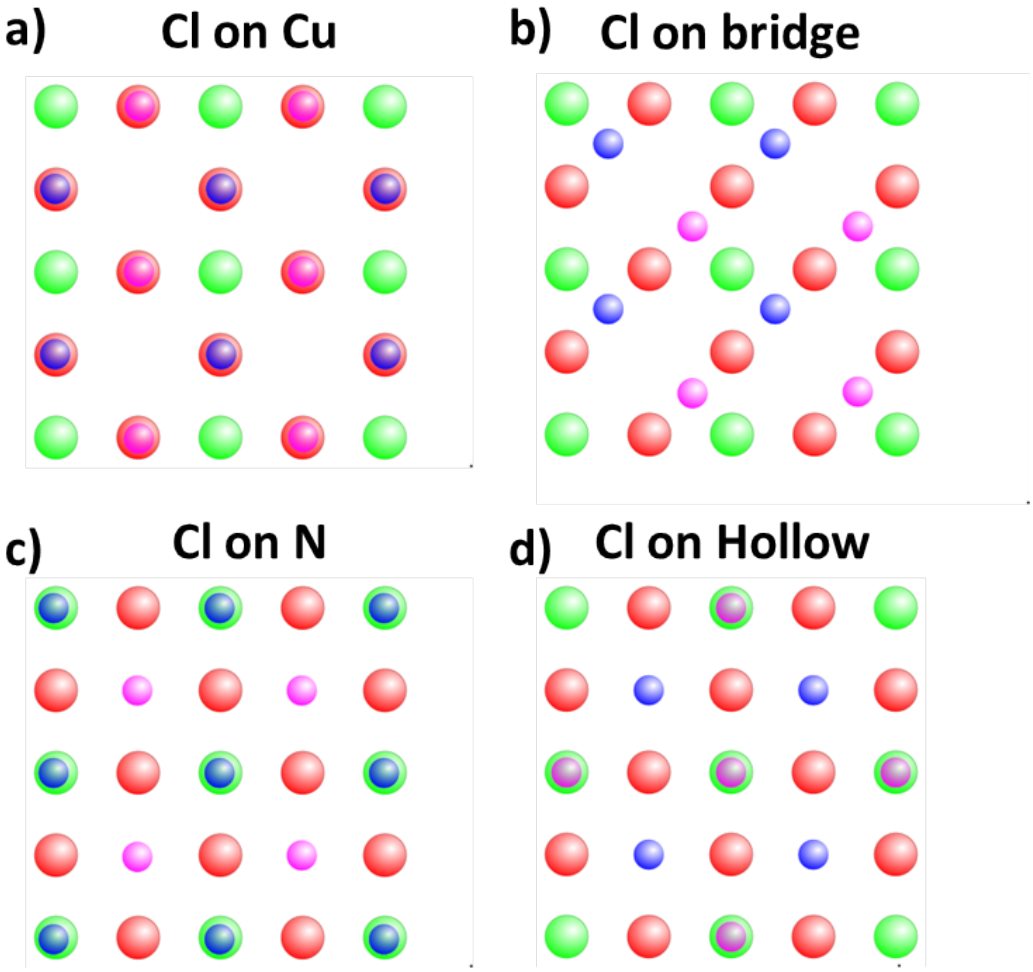

Figure 3.3: Sketch of considered adsorption sites for NaCl on top Cu_2N/Cu(001) for DFT calculations. Green balls correspond to N atoms, blue to Cl atoms, red to Cu atoms, magenta to Na atoms. a) Cl atoms on top of Cu sites. b) Cl atoms on top of bridge sites. c) Cl atoms on top N sites. d) Cl atoms on top of Hollow sites.

The Cu_2N lattice is incommensurate with Cu(001) due to strain effects [71]. There-

fore, two lattice parameters were considered for DFT calculations: the Cu(001) bulk lattice parameter (3.6 Å) and the Cu_2N lattice parameter (3.72 Å).

3.6 Å			
	N Site	Cl Site	Hollow Site
E_f (eV)	-2.00	-2.07	-2.19
ΔE_f (eV)	0.19	0.12	0.00
E_{ad} (eV)	-0.18	-0.25	-0.36
3.72 Å			
E_f (eV)	-2.10	-2.19	-2.33
ΔE_f (eV)	0.23	0.14	0.00
E_{ad} (eV)	-0.18	-0.26	-0.40

Table 3.1: NaCl on Cu_2N formation and adsorption energy. Calculated film formation energy E_f (per NaCl dimer), relative change in film formation energy ΔE_f, and film adsorption energies E_{ad} in the surface unit cell. Values are shown for calculated lattice constants a of 3.60 Å(the value for bulk Cu) and a = 3.72 Å(the value for Cu_2N).

3.4 Structural Characterization

3.4.1 Height Analysis

A full characterization of NaCl-ML and BL over Cu_2N implies STM topographic height analysis (Fig. 3.4). The most relevant heights obtained at V_{set}=-1.3 V, $I_{set} = 50pA$ are shown in table 3.2. From Cu, the NaCl-ML/Cu_2N shows a relative height of 0.5 Å, NaCl-BL/Cu_2N shows an apparent height of 2 Åwhile NaCl-BL on bare Cu(001) is 3 Å.

Relative heigh from Cu(001)		Relative height from Cu_2N/Cu(001)	
Phase	Height (Å)	Phase	Height (Å)
Cu_2N	-0.65	Cu	0.65
NaCl-ML/Cu_2N	0.5	NaCl-ML/Cu_2N	1.15
NaCl-BL/Cu_2N	2	NaCl-BL/Cu_2N	2.65
NaCl-BL	3	NaCl-BL	3.65

Table 3.2: Analysis of the relative height for the NaCl-ML and Bl over Cu_2N.

Depressions observed on Cu_2N islands when performing STM are due to their insulating nature rather than the formation of structural holes. This electronic contrast can also be observed through the NaCl overlayer and it varies with the applied bias. In order to confirm that NaCl-ML and BL over Cu_2N was in fact structurally flat as

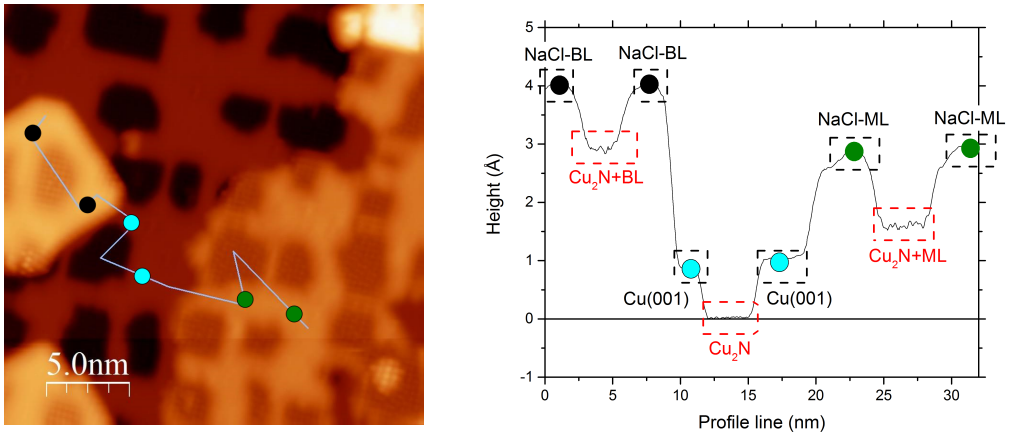

Figure 3.4: Profile analysis of NaCl-ML and BL over Cu_2N/Cu(001) and Cu(001). a) Topographic STM image of NaCl-ML and BL over Cu_2N islands with a profile line. b) Profile analysis of the different layer heights (V_{set}=-1.3 V, I_{set}=50 pA).

it is suspected, AFM measurements over NaCl-ML were performed. FM-AFM at constant Δf measurements show a flat surface while the current image (a -10 mV bias was applied) shows contrast delimiting perfectly the border of the Cu_2N islands (Fig. 3.5).

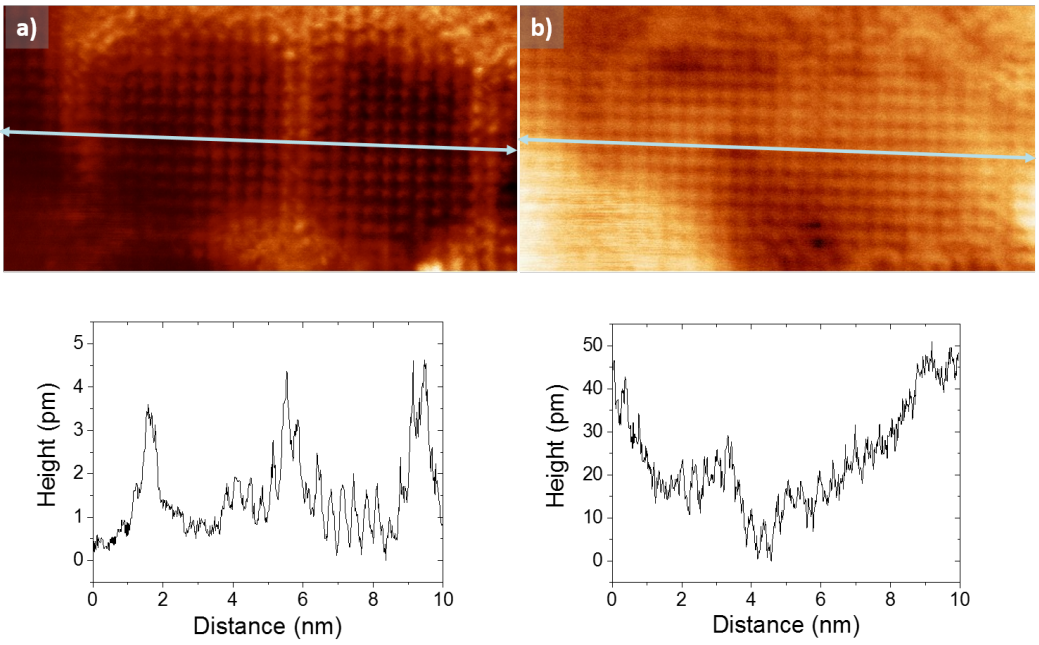

Figure 3.5: Simultaneous STM and AFM image. a) Simulataneous current image (with an applied bias of -10 mV) and its line profile (lower graph). b) Topographic AFM image of NaCl-ML over Cu_2N islands and its profile (lower graph) covering the whole image (Δf_{set}=-2.40 Hz).

3.4.2 Estimation of the Tip-Sample Distance

One of the requisites for performing STM is that the scanned surface must be conductive. Nonetheless it is possible to perform STM over an insulating adlayer above a metallic substrate if the film is thin enough so the electrons can tunnel through it. Tunnelling through an insulator, reduces inevitably the absolute tip-sample distance, forcing the tip to scan closer to the insulating layer.

In normal conditions (tip over conducting surface), the tip cannot approach to the surface unless high currents are applied. Hence, short range tip-sample interactions are neglected [72]. Stacking several insulators will reduce the tip-sample distance. For this reason, it is important to do an estimation of the real tip-sample distance.

The point contact impedance is 12.9 kΩ [73], which is the inverse of the quantum of conductance. With this approximation it is possible to do a rough estimation of the tip-sample distance. With the employed scanning conditions for this sample (V_{set}=-1.3 V and I_{set}=50 pA) and the fact that increasing 1 Åthe tip-sample distance will reduce in one order of magnitude the tunnelling current (or in other words, and increasing of one order of magnitude the impedance), we have that the tip will be around 6.3 Åabove the bare metallic surface. With the calculated structure by DFT (see discussion in the following section) and the relative heights of the STM images, it is possible to estimate the height of the tip above various surfaces; the results are shown in the table 3.3.

Substrate	Height (Å)
Cu(001)	6.3
Cu_2N	5.65
NaCl-ML/ Cu_2N	3.8
NaCl-BL/ Cu_2N	2.3
NaCl-TL/ Cu_2N	0.1

Table 3.3: Estimation of the absolute tip-sample distance for the following scanning conditions V_{set}=-1.3 V, I_{set}=50 pA.

On the LT-STM, the qPlus AFM sensor incorporated into the tip gives us the possibility to confirm these estimations. Setting the bias to zero (in order to minimize flowing tunnelling current) it is possible to observe where the tip is contacting with the insulator, since there is a disturbance in Δf(z) and in I(z) (Fig. 3.6).

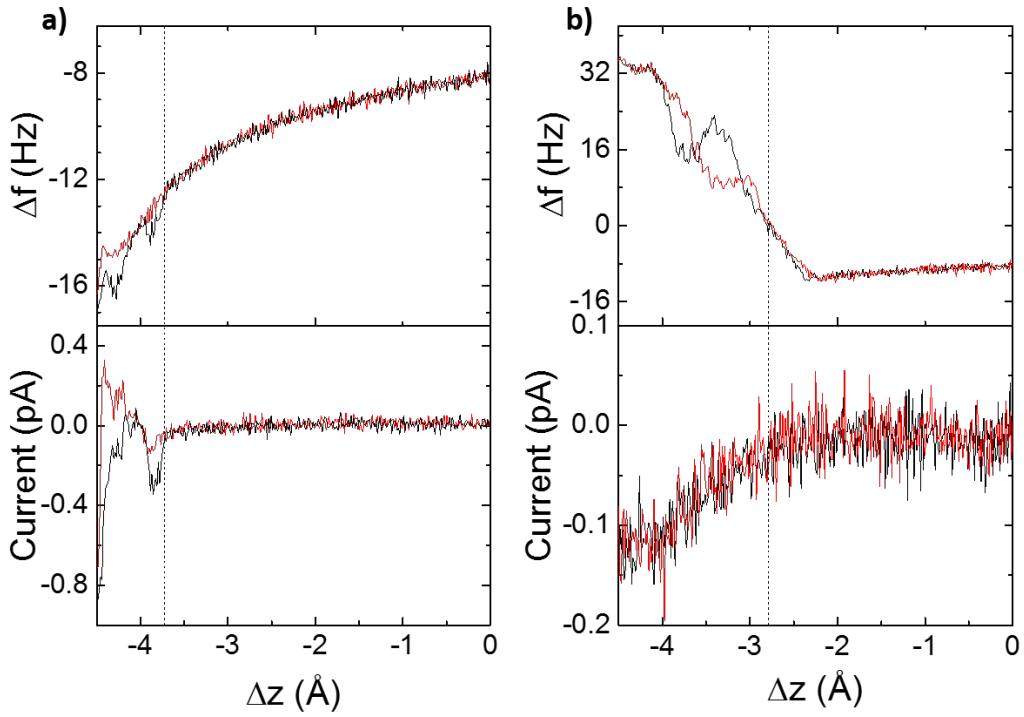

Figure 3.6: Height estimation for NaCl-ML and BL on Cu_2N based on simultaneous measurements of Δf and I vs Δz (V_{set}=-1.3 V, I_{set}=50 pA); after the feedback loop is opened, V is set to zero for the measurements. The black (red) spectrum is measured as the tip approaches (is retracted from) the surface. Vertical dashed line points out where the tip "disturbs" the NaCl layer, as indicated by a change in the current. a) Tip-sample distance measured for NaCl-ML in a saturated Cu_2N sample. b) Tip-sample distance measured for NaCl-BL in a saturated Cu_2N sample.

There are two different characteristics that can be detected when the tip is in point contact with the NaCl. The first one is the disturbance in the current. The second one is the hysteretic behaviour of the forces ($\Delta f(\Delta z)$), which indicates the chemical interaction with the substrate.

The distances measured here for a V_{set}=-1.3 V and I_{set}=50 pA, which corresponds to the tip being approximately 3.72 Åabove the surface for the ML and 2.8 Åfor the BL are in agreement with the estimation performed previously.

3.4.3 Atomic Structure

Previous studies have identified the chemical species of Cu_2N (Fig. 3.7a) and NaCl (Fig. 3.7b) using STM with atomic resolution in combination with theoretical calculations. These studies show that STM images of NaCl only show the anionic species (Cl atoms) while Na atoms remain as dark spots. In the case of Cu_2N, when scanning

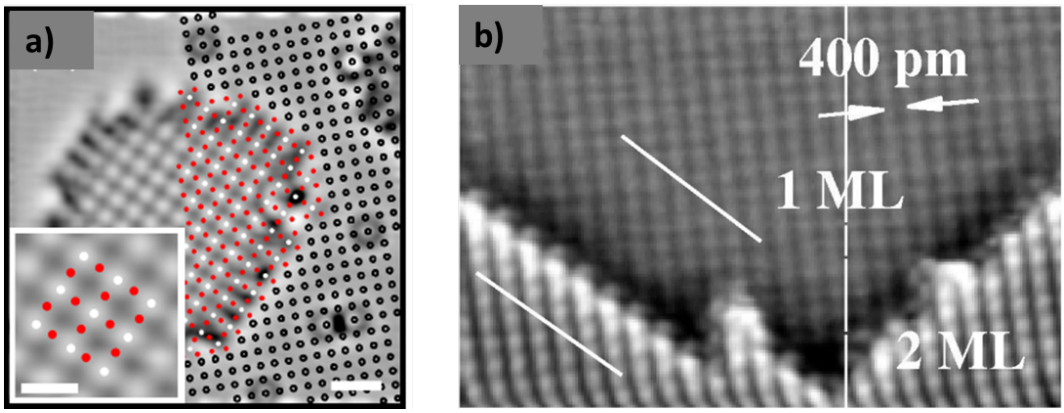

Figure 3.7: Chemical species determination for; a) Cu_2N measured at V_{set}=-0.4 V, I_{set}=6 nA, where bright spots at negative bias are determined to be N atoms and dark spots are the Hollow sites between Cu atoms. Empty circles are Cu atoms beyond the Cu_2N island where due to strain effects both Cu lattices are incommensurate [71]. *Permission to reproduce this image has been granted by Physical Review B.* b) NaCl measured at V_{set}=-1.2 V, I_{set}=0.61 nA, where with the help of an STM atomically resolved image and DFT calculations, bright spots are determined to be the anionic species (Cl atoms) and dark spots correspond to Na atoms [74]. *Permission to reproduce this image has been granted by Surface Science.*

at high negative bias (sample bias convention), N atoms are bright dots while empty space between Cu atoms (Hollow sites) are identified as dark spots. With this criterion we can interpret atomically resolved STM images to resolve the binding sites of NaCl on Cu_2N (Fig. 3.8). NaCl grows epitaxially on top of Cu_2N. By sketching the NaCl lattice, centering on top of Cl atoms and then extending it to adjacent Cu_2N layer is possible to determine with atomic precision the binding sites. This process can be extended in the same way for NaCl-BL to NaCl-ML on top of Cu_2N/Cu(001). As described previously, four different adsorption sites were considered for NaCl atoms on Cu_2N. DFT calculations show that the most stable adsorption site is Cl on top of Hollow site, forcing the Na atoms to place on top of N. Previous DFT calculations have shown that Cu_2N is polar covalent bonded to Cu(001), transferring part of charge to the Cu(001) (covalent bond) and a modulation of the charge due to its insulating nature [41].

DFT calculations show that the electrostatic potential is positive above the Cu and hollow sites of Cu_2N, and negative above the N. (Fig. 3.9). Therefore, identified binding sites of NaCl-ML on top of Cu_2N are not only consistent by energy formation means but also by simple electrostatics, where Cl atoms (which are negatively charged) place on the most positive site of Cu_2N (hollow sites) and Na atoms (which

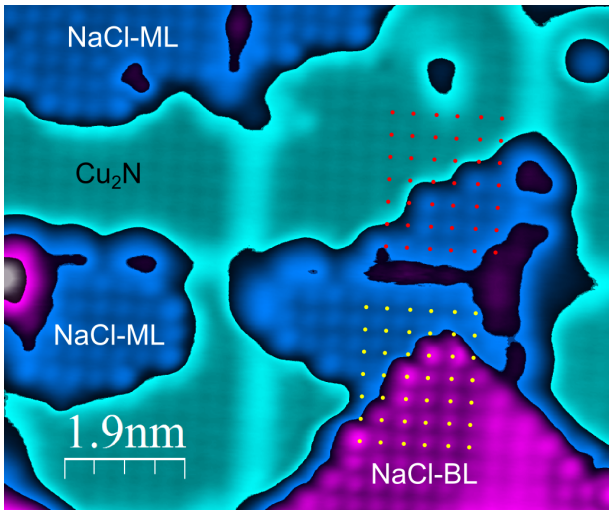

Figure 3.8: STM image with atomic resolution of NaCl-ML on Cu_2N and NaCl-BL on NaCl-ML. Red dots are centred on bright spots of the NaCl-ML which corresponds to Cl atoms. The lattice is extended to the emerging Cu_2N patch free of NaCl. The atoms matches to the dark spots, identified as Hollow sites of Cu_2N. Yellow dots are centred in the bright spots of NaCl-BL corresponding to Cl atoms. The extended lattice match with dark spots between Cl atoms of the NaCl-ML. This follows the expected stacking for NaCl, where Cl are on top of Na atoms and vice versa (V_{set}=-1.3 V and I_{set}=50 pA).

are positively charged) go to the most negative site (N atoms) (Fig. 3.9).

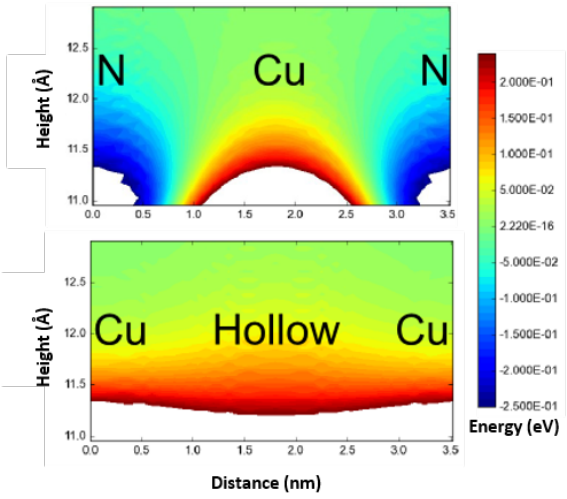

Figure 3.9: Cross sections of calculated electrostatic potential energy in eV for Cu_2N centered in Hollow site and Cu.

Once the arrangement of NaCl on top of Cu_2N is understood, a ball model is created to understand how NaCl accommodates to the Cu_2N lattice (Fig. 3.10). The NaCl structure is rotated 45° and compressed by a 7% in order to match the Cu_2N lattice. By calculating charge transfer between Cu_2N and NaCl-ML layers it is possible to

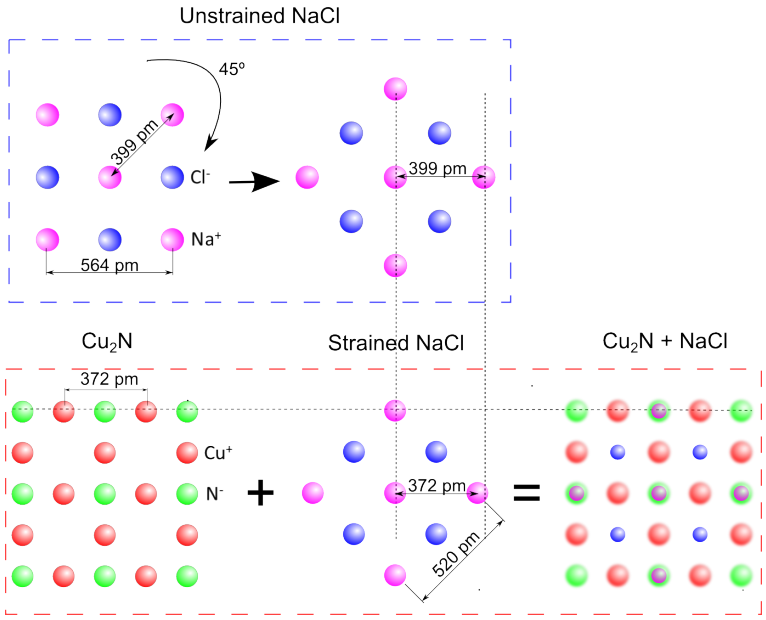

Figure 3.10: Ball model of Cu_2N and NaCl showing the atomic rearrangement of NaCl in order to match the lattice of Cu_2N.

determine what is the bonding nature of these two layers. Figure 3.11 shows charge density difference plots which are defined by the following equation

$$\Delta n = n(NaCl(1ML)/Cu_2N) - n(Cu_2N) - n(NaCl - ML) \tag{3.3}$$

where electron density of NaCl-ML/Cu_2N/Cu(001) is subtracted from the electron density of Cu_2N/Cu(001) and free standing NaCl-ML. Lack of charge transfer between layers in combination with large bonding distance (around 3 Å) and a weak film adsorption energy (-0.4 eV) indicates that the covalent component is small. This therefore points to a purely elecrostatic bonding (eq. 3.3) when NaCl-ML is placed on top of Cu_2N.

3.5 Electronic Structure

One of the advantages of STM with respect to other surface techniques is the possibility of performing spectroscopy with atomic precision. In this way, the electronic structure up to single atoms can be studied [41]. In the same way, electronic structure of atomically thin insulators on metals is accessible by this tool, which in a first approximation, will be a convolution of the local electronic structure of the insulator and the underlying metal with the electronic structure of the tip [13].

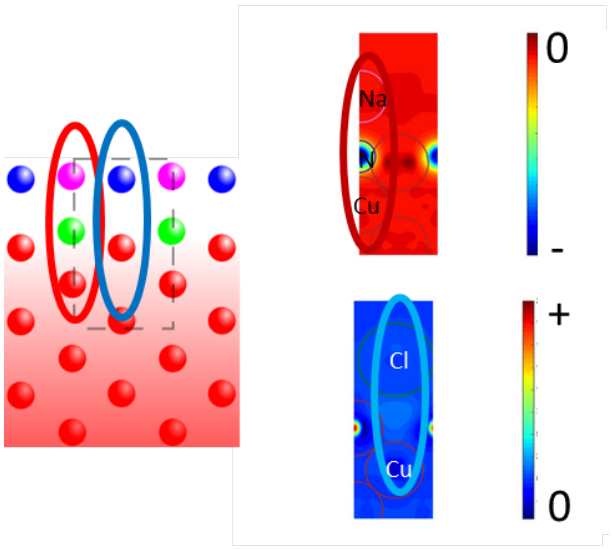

Figure 3.11: Side views of calculated charge transfer for NaCl-ML/Cu_2N/Cu(001) supported with its atomic structure for simplicity.

Spectroscopy taken over Cu_2N/Cu(001), NaCl-ML/Cu_2N/Cu(001) and NaCl-BL/Cu_2N/Cu(001) with the same tip and the same regulation conditions (Fig. 3.12) shows no dramatic differences between insulators. Due to the insulating nature of the layers, it was not possible to go to larger voltages in order to avoid high currents, which damage the NaCl. The features on the spectroscopy have different contributions from the stacked insulators. On one hand, the onset at +2 V is attributed to the band gap of the Cu_2N and thus, the state comes from the Cu(001)/Cu_2N interface. In addition, this feature is spatially variable within the Cu_2N island [75]. On the other hand, the left side of the dI/dV curve (-2 V) shows a new onset.

DFT calculations suggest that the onset at -2V is not a new state coming from the interaction between NaCl and Cu_2N but rather a shift of the NaCl band gap. Figure 3.13 shows the projected density of states for NaCl isolated, NaCl-ML/Cu_2N and NaCl-BL/Cu_2N. The distance between the peaks determines the NaCl band gap; a small shift of the band gap is predicted between NaCl-ML/Cu_2N and NaCl-BL/Cu_2N on the p_z states of chlorine atoms (corresponding to the occupied states of NaCl) due to the electrostatic interaction with Cu_2N.

Figure 3.14 shows NaCl-Bl deposited in a Cu_2N grid (structure composed by Cu and self assembled square Cu_2N islands). Dark areas correspond to Cu_2N while bright areas correspond to Cu(001) rows between Cu_2N islands. Points sketched on

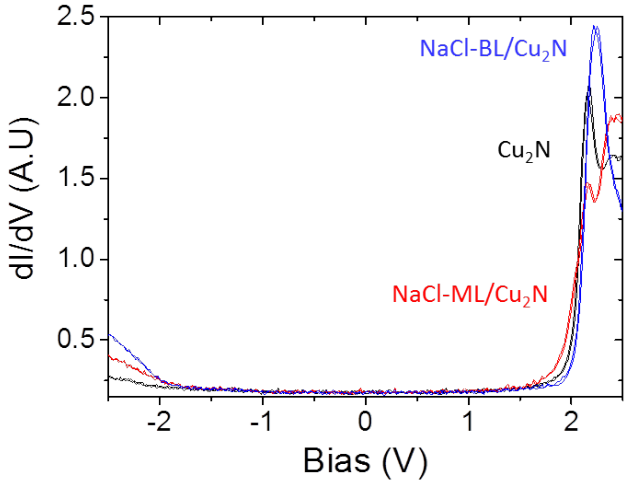

Figure 3.12: dI/dV performed with the same tip over Cu_2N, NaCl-ML/Cu_2N and NaCl-BL/Cu_2N (V_{set}=2.5 V, I_{set}=600 pA, V_m=12 mV).

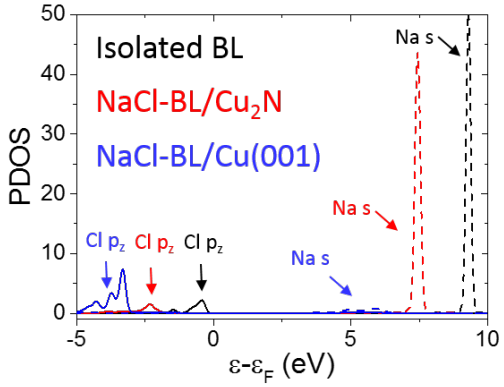

Figure 3.13: Projected density of states of NaCl Cl p_z (solid line) and Na s states (dashed line). Isolated (black), NaCl/Cu(001) (blue) and NaCl/Cu_2N/Cu(001) (red).

the image shows where spectroscopy was taken. As it can be shown, the electronic transition is occurring within two atomic distances. This suggests that Cu_2N is in fact modifying the electronic properties of the NaCl overlayer. Two remarkable aspects are observed in this transition. For NaCl on Cu_2N grid (Fig. 3.14a) no features are detected on NaCl between Cu_2N islands, while for spaced Cu_2N islands (Fig. 3.14b), a feature at 1.5 V can be spotted and close to the Cu_2N, the spectroscopy is similar to Fig. 3.14. The feature at +1.5 V is an unscreened peak by the NaCl layer coming from the Cu(001) (Fig. 3.15) also observed on figure 3.14b while the absence of features on the Cu(001) on grid Cu_2N or close to these islands is due to the influence of the nearby Cu_2N islands on the Cu(001) [76].

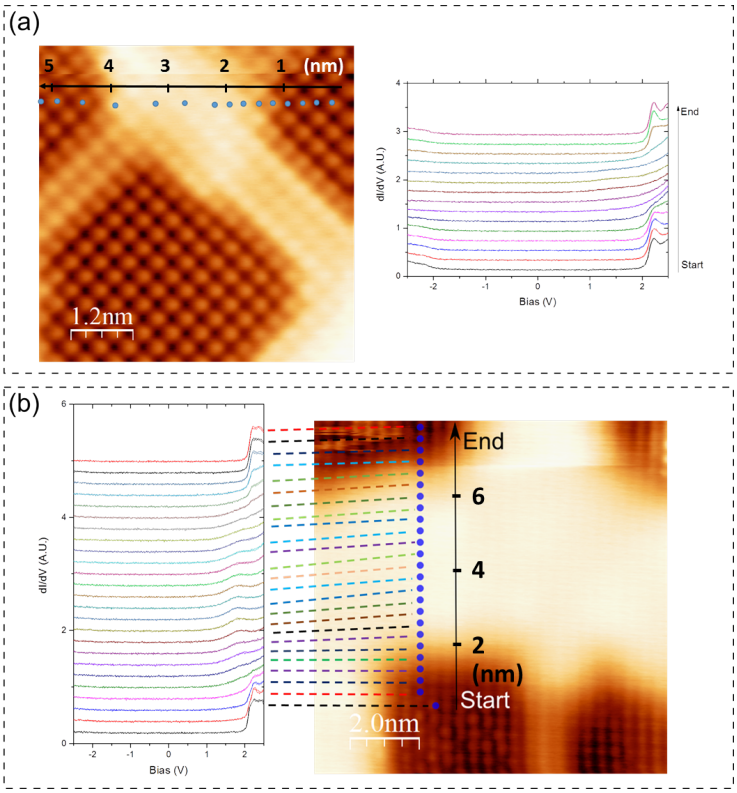

Figure 3.14: Sequential dI/dV curves taken over NaCl-BL on top of Cu_2N. a) Cu_2N grid. b) spaced Cu_2N islands.

It is important to emphasize another role played by Cu_2N. DFT calculations show substantial differences in the electronic structure between isolated NaCl, NaCl-BL/Cu(001)and NaCl-BL/Cu_2N/Cu(001) (Fig. 3.13). When NaCl is deposited on the bare metal surface, the projected density of states p_z of Cl and the s states of Na are strongly hybridized as it is observed by going from sharp peaks to broad features. In contrast, the states of NaCl on Cu_2N are in a narrow range of energies becoming sharp again and therefore it removes the degeneracy of the projected density of states of Cl and Na ions. This, indicates a lack of hybridization with the substrate. Cu_2N is hence, isolating an insulator. This, in first approximation, naive affirmation will have important implications that will be discussed in the next chapter.

Many experiments have used NaCl and other rock-salt binary compounds as a decoupling layer for the study of molecules and atoms [47, 77]. In these studies submolecular resolution of pentacene molecules was achieved by depositing them on top of insulating NaCl layer. As seen in those experiments, submolecular resolution is achieved when the molecule is scanned at HOMO-LUMO energies which corresponds to -2.4 and 1.7 V respectively (Fig. 3.16). Since DFT shows strong

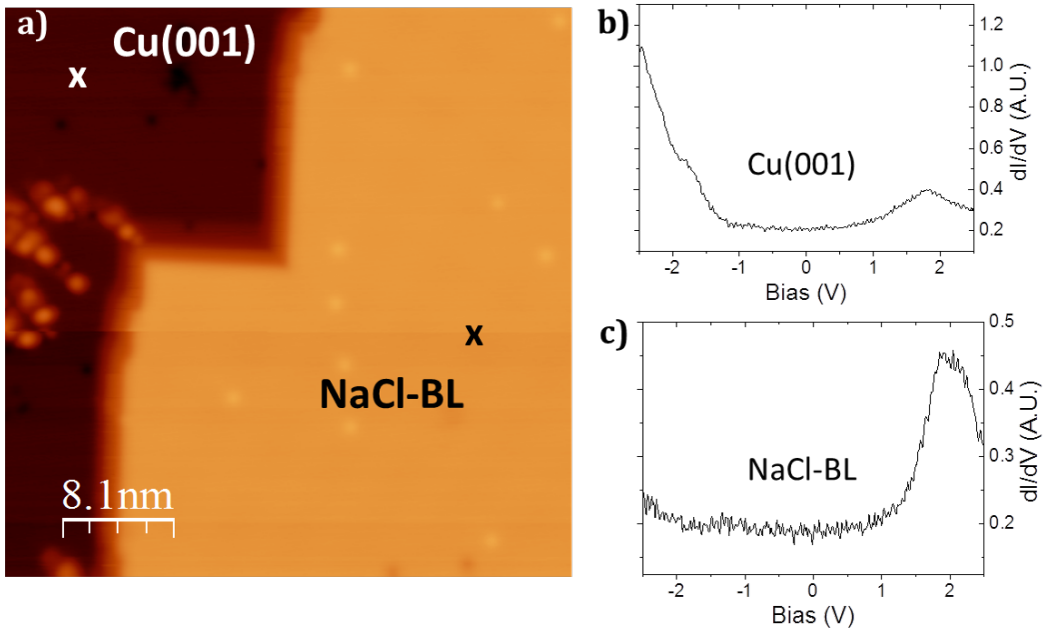

Figure 3.15: Spectroscopy for NaCl-BL on top of Cu(001). a) Topographic image of NaCl/Cu(001)(V_{set}=-1.3 V, I_{set}=50 pA) the crosses points out where the spectroscopy was taken. b) Spectroscopy taken on bare Cu(001). c) Spectroscopy taken on top of NaCl-BL (V_{set}=-2.5 V, I_{set}=200 pA).

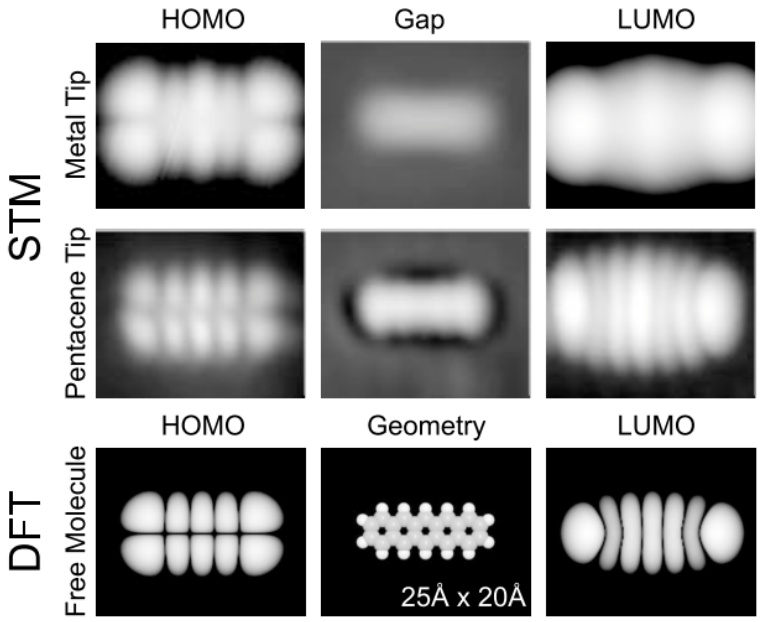

Figure 3.16: Submolecular resolution on pentacene on NaCl [47]. *Permission to reproduce this images has been granted by Physical Review Letters.*

hybridization of NaCl with the metallic substrate, there might be also be influence on the molecule decoupling causing in this way a hybridization with the underlying metal. Thus, the visualization of these orbitals might be affected because of the hy-

bridization. An improvement of the resolution might be achieved by depositing the molecules on top of NaCl/Cu_2N.

3.6 Conclusion

In this chapter we have shown the creation and characterization of a new material which is NaCl/Cu_2N/Cu(001) consisting in stacked atomically thin insulating layers. STM study in combination with DFT calculations have shown that NaCl adopts the lattice parameter of Cu_2N, which works as a charge modulated template.

In addition electronic characterization, by means of STS, have been performed on this new system. Spectroscopy in agreement with DFT suggests a band gap shift of NaCl/Cu_2N/Cu(001) due to electrostatic interactions in contrast with NaCl on Cu(001) or isolated NaCl-BL.

Cu_2N acts as a decoupling layer preventing the NaCl layer to hybridize with the substrate. Previous studies have pointed to the importance to chose the right substrate for decoupling molecules and atoms from the metal host. Free charges in the interface between a metallic substrate and a polar material will lead to surface dipole suppression due to screening produced by the free charges as well as a charge transfer between the polar compound and the host metal [78, 79] . This effect can be reduced by growing the polar material on top of an insulator. Regularly used insulating buffers comprise oxide compounds. If an oxide insulator is used to buffer and decouple the active polar layer, other side affects are expected to appear. For instance, oxygen vacancies may produce free carriers leading in the same way to a surface dipole screening. In addition a polar surface free electrode may suffer a reconstruction in order to avoid surface charges [80].

For these reasons using an atomically thin insulating layer of Cu_2N can represent a new approach for the control of induced properties on polar compounds like the emergence of unscreened surface dipoles. The NaCl on Cu_2N growth proof-of-concept shows a vast family of rock-salt binary compounds that can have a variety of artificially induced strain conditions.

3.7 Future Work

NaCl is able to adopt the lattice parameter of Cu_2N by compressing its lattice a 7% respect its bulk structure. Past theoretical studies have suggested that provoking a compressive strain on rocksalt binary compounds might lead to induced ferroelectricity [63, 64]. One of the limitations of this system is the impossibility of studying it beyond 3 atomic layers due to the insulating nature of the components. In order to explore the possible ferroelectricity one possibility could be growing a thin layer film and study it by conventional techniques used in the ferroelectric field.

Another important aspect is the fact that the structural and electronic properties of the compound might change with the applied strain. It has been shown that it is possible to grow and study a wide range of rocksalt compounds on metallic surfaces [81, 60, 82, 83, 59]. Depositing these compounds with rock-salt structure with larger lattice parameter on Cu_2N could lead to dramatic changes in their electronic and structural properties.

Compound	Lattice Constant Å	Ref.
LiCl	5.14	[59]
LiBr	5.50	[83]
NaCl	5.64	[48]
KCl	6.29	[58, 82]
KBr	6.586	[60]
RbCl	6.59	[59]
RbI	7.35	[82]

Table 3.4: Lattice parameter of binary rock-salt compounds already studied by SPM.

Chapter 4

Piezoelectric behaviour in atomically thin stacks of polar insulators

4.1 Abstract

Here, we report that atomically thin layers of sodium chloride (NaCl) exhibit inverse piezoelectric behaviour: a displacement of the atoms driven by an applied electric field. This is due to the combination of polar layer isolation and induced out of plane dipole arising from compresive strain. Using scanning probe microscopy, we locally manipulate and reverse the atomic dipoles in NaCl, as measured through sharp changes in the tunnel current and force between the surface and a nearby probe tip. These results suggest a new way to create piezoelectric effects at the interface between ultra-thin insulating polar materials, pushing the feasible size of functional multiferroics down to the atomic scale.

4.2 Introduction

The reduction in size of modern electronic devices is forcing them inevitably towards the atomic scale. This size reduction not only affects technology based in the giant magnetoresistance effect (magnetic hard disk drives) but any technology potentially used to store information. For competitive ferroelectric-based memory devices, it is mandatory to reduce the size of the ferroelectric domains, which implies an overall size reduction. Contrary to ferromagnets, where the size limits are well known, there is still an open question about what is the critical thickness for ferroelectricity to manifest [78, 84]. Ferroelectric materials can be used as binary data storage media

in which opposite directions of polarization represent the 1 or 0 data bits. This is particularly important because the standard read out of the stored data implies the use of electric fields and therefore a depolarizing field which erases or perturb the stored information through successive cycles. Different strategies have been employed to avoid destructive read out like multiferroics [85], where the data is written by means of electric fields and read out in the change of the magnetization state [86].

Another way to read the polarization in a non-destructive manner calls for the preservation of ferroelectricity in the ultrathin regime [87, 88]. Because a tunnel current can flow between metallic electrodes sandwiching an ultrathin ferroelectric barrier, it is possible to change the polarization with the help of electric fields. In this way, a change in the conductivity will be detected due to the change in the tunnelling barrier and hence it becomes possible to *read* the current polarization.

Main strategies to achieve ferroelectricity at these regimes have employed perovskite oxide compounds and an insulating layer that can exclude the appearance of free charges that would otherwise cause a depolarizing field cancelling the spontaneous polarization of these structures [80, 79]. Unfortunately, an insulating substrate implies that these systems are not reachable by techniques such as STM, which can characterize the electronic properties of the system with atomic resolution.

The previous chapter has dealt with the necessary ingredients that are required to succeed in the creation of an ultrathin ferroelectric material. Cu_2N, as an insulating layer, prevents on the one hand hybridization and charge transfer between layers and on the other hand lacks free charges that are responsible for creating depolarizing fields. Through strain engineering we will show that we are able to break the center of symmetry of NaCl, inducing in this way, a net out of plane dipole.

Because we are able to tunnel through NaCl/Cu_2N stacked insulating layers (that are atomically thin), we can study the electronic properties of this heterostructure as a function of applied electric fields, showing piezoelectricity and a possible incipient ferroelectricity.

4.3 Induced Polarization

The polar nature of Cu_2N works as a charge modulated template for NaCl. This forces NaCl to adopt the lattice parameter of Cu_2N and in this way, suffer a compres-

sive strain of a 7% with respect to the bulk lattice. As a consequence of the compressive strain and due to Pauli's repulsion between adjacent co-planar atoms, an induced rumpling emerges on NaCl. This causes an out of plane dipole moment on NaCl and consequently, it breaks the symmetry center of the rock-salt binary structure. Calculations carried out for NaCl-ML and BL on Cu_2N/Cu(001) show an induced out of plane rumpling of 11 pm for NaCl-ML/Cu_2N/Cu(001) (Fig. 4.1c) in contrast to bulk NaCl (Fig. 4.1b). NaCl-BL layers also suffer an induced rumpling which is more pronounced on the most external layer (Fig. 4.1c) (12 pm). No significant perturbation of the Cu_2N lattice is noticed.

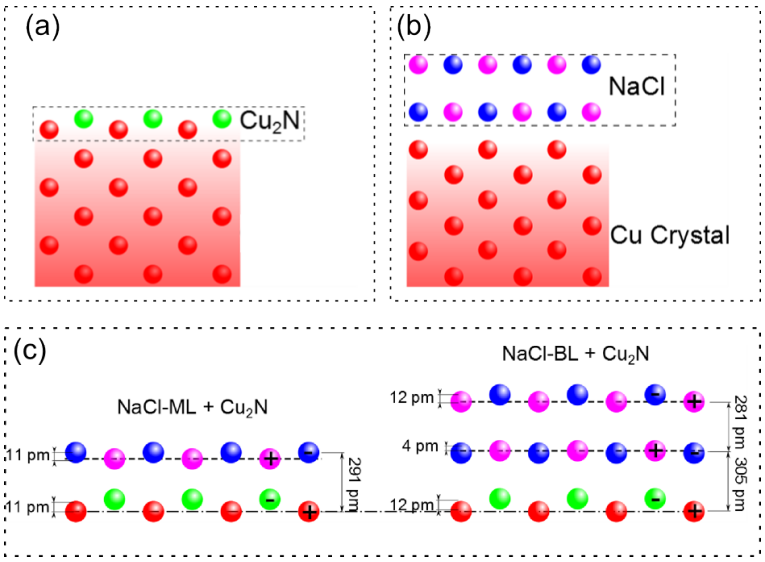

Figure 4.1: Side view of (a) Cu_2N, (b) NaCl on Cu(001), (c) NaCl ML and BL on Cu_2N. The rumpling has been multiplied by 3 for the sake of clarity.

It is important to note that there is not new creation of an out of plane dipole moment on the whole system by adding NaCl to Cu_2N, since Cu_2N possess already a net out of plane dipole due to its polar-covalent bonding nature. Nonetheless there are several differences between Cu_2N and NaCl. In contrast to NaCl, Cu_2N is strongly bonded to the metal surface through an electrostatic and partially covalent interaction [38]. This difference might lead NaCl to exhibit a strong response in the presence of an electric field, which will be explored in the following sections.

The tunnelling barrier height can be related to the surface density dipole moment through the work function [89].

$$\frac{\mu}{A} = -\frac{\Phi\varepsilon_0}{e} \tag{4.1}$$

where μ is the dipole moment, Φ is the work function, A is the surface area, ε_0 is the dielectric constant and e the elementary charge. And thus, a larger dipole moment will imply a larger work function. DFT calculations show that the out of plane dipole moment does increase noticeably when NaCl is deposited on Cu_2N, but does not increase substantially with the number of stacked layers (table 4.1).

	NaCl-TL/Cu_2N	NaCl-BL/Cu_2N	NaCl-ML/Cu_2N	Cu_2N
Φ (eV)	5.31	5.12	5.38	4.88
μ (eÅ)	-0.381	-0.367	-0.386	-0.350
$\Delta\mu$ (eÅ)	-0.031	-0.017	-0.036	0.000

Table 4.1

From the structure (Fig. 4.1) it is easy to see that for each layer the dipole formed by Cl and Na is antialigned with the adjacent layer in NaCl-BL/Cu_2N/Cu(001). In this way the dipoles are partially cancelled out and then, the total out of plane dipole does not increase with the stacking of subsequent layers. This kind of structure could be the precursor of an antiferroelectric, where every dipole is antialigned.

In order to probe the change of the net out of plane dipole in the different stacked insulators, I(z) measurements will be performed to retrieve information about the change in the apparent barrier height. Furthermore, in view of the properties explained previously (lack of charge transfer, prevention of the hybridization of the states of the NaCl on Cu_2N and the induction of a net out of plane dipole) the response with the electric field will be studied.

4.4 Probing the Apparent Barrier Height

The accuracy of STM resides in the fact that the tunnelling current depends exponentially on the distance. Small changes in z distance result in big changes in the current, generating a large contrast between objects that are only a few angstroms away from each other in height. The decay of the tunnelling current with distance is ruled by the following expression:

$$I(z) = |\Psi(z)|^2 = |\Psi_0|^2 e^{-2kz} \tag{4.2}$$

with

$$k = \frac{\sqrt{2m(\Phi_{avg} - eV)}}{\hbar} \tag{4.3}$$

where Φ_{avg} is the average barrier height of tip and sample.

4.4.1 Apparent Barrier Height Modification with Stacked Insulating Layers

Since the apparent barrier height and the dipole moment are directly related [89], it is possible to follow the evolution of the surface dipole with the same tip over different insulating layers by means of I(z) spectroscopy.

Figure 4.2 shows the different current decays for the insulating layers. Fitting the obtained exponentials, the extracted apparent barrier heights, which are an average of the tip and sample barrier heights, are 5.75, 5.25 and 5.4 eV for Cu_2N/Cu(001), NaCl-ML/Cu_2N/Cu(001) and NaCl-BL/Cu_2N/Cu(001) respectively; this is similar to prior measurements of the Cu_2N workfunction of 5.5 eV [76]).

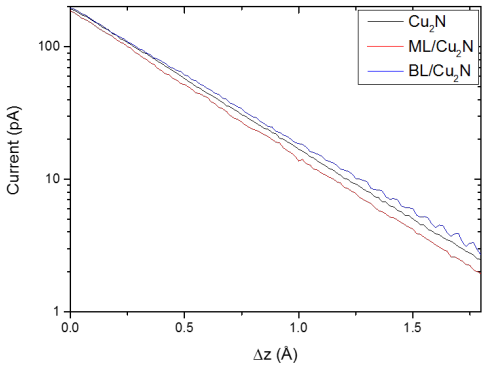

Figure 4.2: Comparison between current decays for Cu_2N/Cu(001), NaCl-ML/Cu_2N/Cu(001) and NaCl-BL/Cu_2N/Cu(001) (V_{set}=-1 V, I_{set}=200 pA).

These results can be compared with theoretical calculations, where the work function varies from 4.86 eV for Cu_2N to 5.02 and 4.91 for NaCl-ML and BL on Cu_2N/Cu(001). The surface dipole is enhanced when NaCl is stacked on Cu_2N/Cu(001) with respect to Cu_2N/Cu(001).

4.4.2 Unusual Effects on Close Tip-Sample Distances: Elastic Deformations

Due to the insulating nature of stacked NaCl on Cu_2N/Cu(001), the estimated tip-sample distance in regular scanning conditions (-1.3 V and 30 pA) is only 3.72 Åfor NaCl-ML/Cu_2N and 2.8 Åfor NaCl-BL/Cu_2N. For this reason, an influence of prox-

imity effects on I(z) spectroscopy can not be discarded. Here we show, how tip-sample distance (controlled through the setting bias) has an influence on the measured current decay curves. Strong interaction at short tip-sample distances produces a distortion of the current decay, resulting in a non-exponential behaviour.

Figure 4.3 shows the shape dependence of the exponential with the regulation bias. While upper panel shows a variation in the shape of the exponential with the regulation bias, the lower panel shows the existence of at least two different regimes: a short distance regime, which cannot be fitted to an exponential and a long distance regime, which follows a completely exponential decay.

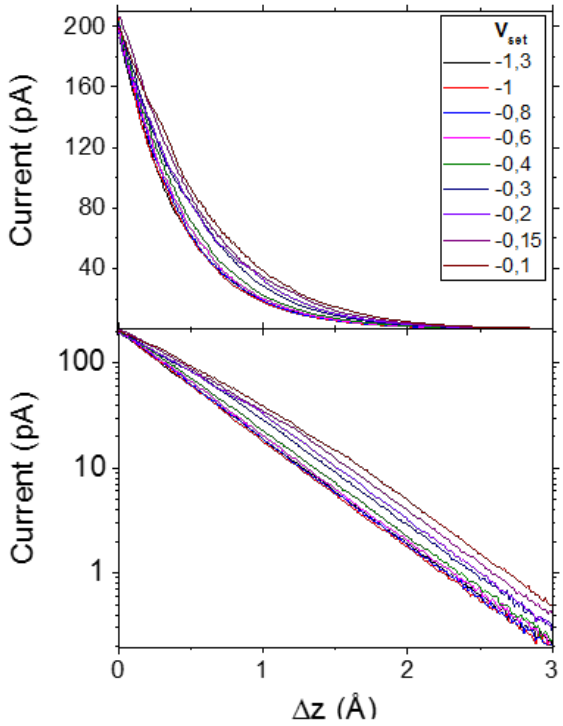

Figure 4.3: I(z) curves measured at I_{set}=200 pA and V_{set} that varies from -1.3 V (large tip-sample distance regime) to -100 mV (short tip-sample distance regime) on NaCl-BL/Cu_2N/Cu(001). There was a background current of 500 fA inherent to the microscope that was subtracted. Upper panel, distortion of the exponential decay with the setting bias. Lower panel, upper graph plotted in semi-log scale.

In order to disentangle the dependence of both regimes with setting bias, the curves were normalized in the large tip-sample distance range since at that range the decay is purely exponential. In this way, it can be observed that there is shift from the non exponential to the exponential regime dependent on the setting bias; in addition, simultaneous Δf(z) measurements were performed. As it is observed (Fig. 4.4), the

beginning of the non exponential regime can be associated with the beginning in the increase of the Pauli repulsion contribution in Δf.

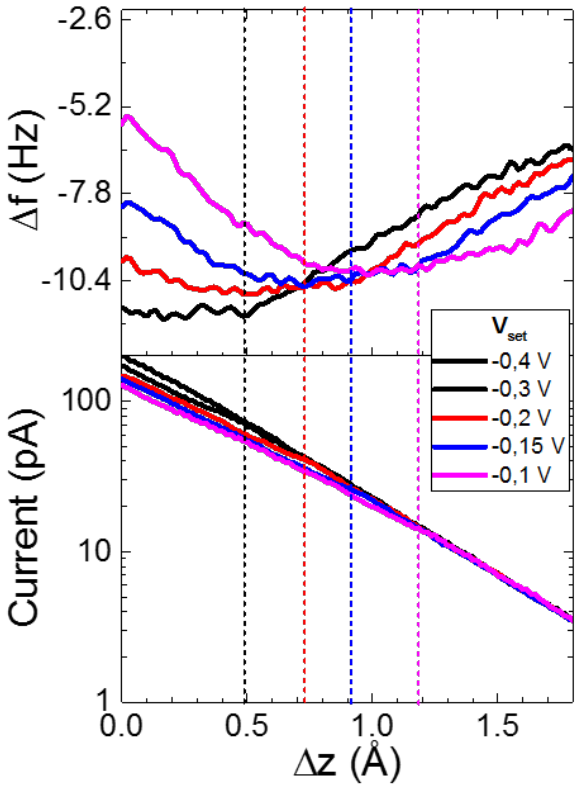

Figure 4.4: Simultaneous $\Delta f(\Delta z)$ and $I(\Delta z)$ measurements. Upper panel, $\Delta f(\Delta z)$ at different setting bias. Lower panel, simultaneous I(z). A spectrum at V_{set}=-0.4 V is included for better comparison between a regular exponential curve and an exponential with a deviation at short distances. Vertical dashed lines indicate the beginning of the exponential behaviour correlated with the minimum in $\Delta f(\Delta z)$.

Once the distance dependence of the exponential deviation is determined, the next step is the correlation of the exponential deviation with a precise movement of the tip with respect to the sample. For this, the tip was approached in steps of 10 pm and then retracted measuring simultaneously I(Δz) and $\Delta f(\Delta z)$. Fig. 4.5 shows a linear relationship between the relative tip displacement and the displacement of the non exponential behaviour. This indicates that piezoelectric behaviour of the system may be occurring (modification of the induced dipoles through applied pressure). However, it is impossible to disentangle whether the effect comes from the modification NaCl/Cu_2N/Cu(001) structure or the tip itself.

Therefore, differentiating a tip effect from a sample-induced effect becomes essential

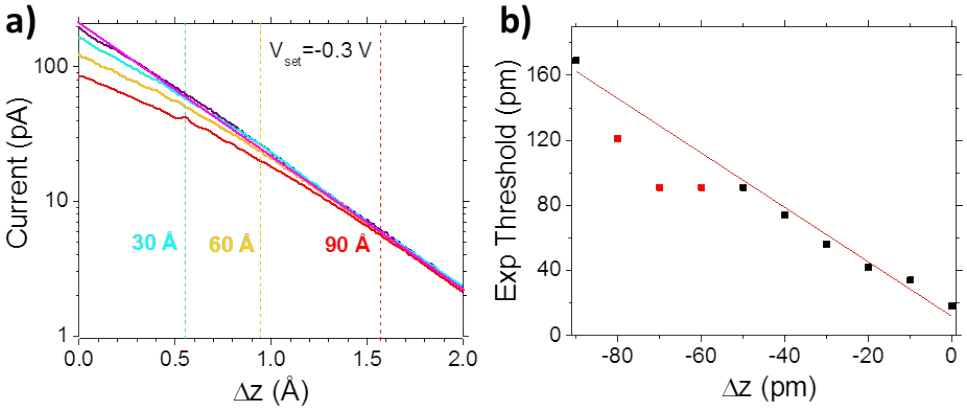

Figure 4.5: Relation between tip-sample distance and exponential distortion displacement. a) Current decay curves normalized to the low electric field state. Dashed lines indicate where the non exponential regime starts, numbers associated to the dashed lines indicates the displacement of the piezo (in pm). b) Displacement of the relative tip-sample distance vs displacement of the beginning of the non exponential behaviour Three points were masked (coloured in red) for the linear fit (V_{set}=-0.3 V, I_{set}=200 pA).

not only for the study of the piezoelectric effect itself but as a general effect that can be always present as a collateral effect in short tip-sample distance measurements.

I(z) spectroscopic measurements performed on top of Cu_2N/Cu(001) (Fig. 4.6) also show deviation from the regular exponential behaviour. Since tip-sample distances are larger for the same conditions above Cu_2N/Cu(001) than above NaCl/Cu_2N/Cu(001), smaller V_{set} will be required to achieve the same tip-sample distance (I_{set}=200 pA, V_{set}=-10 mV). Figure 4.6a indicates, as in the previous case, an I(z) exponential deviation linked to Pauli's repulsion contribution making indistinguishable a structural deformation occurring in the tip or the sample. This is further confirmed by simultaneous Δf (Δz) (Fig. 4.6b) where the arising Pauli's repulsion contribution indicates that the tip is very close to Cu_2N.

Experiments carried on NaCl-BL/Cu_2N and Cu_2N suggest that the tip-sample proximity is responsible for the exponential decay deviation through strong interactions. The strong bonding of Cu_2N to Cu(001) [41] (polar covalent bonding) makes unlikely that the atoms of the substrate move but rather that the positions of atoms in the tip are being distorted. In conclusion, elastic deformations of the tip at short tip-sample distances lead to a modification of the tip structure that is seen as a perturbation on the purely exponential decay of the current. These results are relevant on highly insulating systems as the one studied in this thesis where tip-sample distances are short

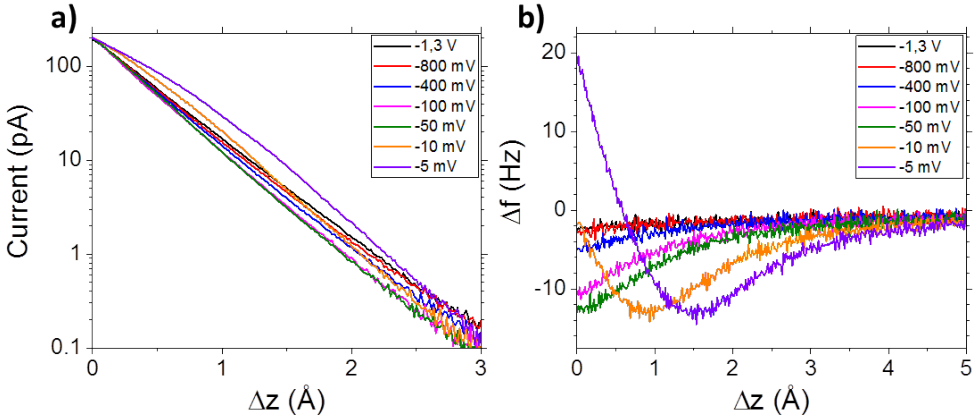

Figure 4.6: I(Δz) and $\Delta f(\Delta z)$ Taken simultaneously at variable tip-sample distances on top of Cu_2N. a) I(z) spectroscopy taken on top of Cu_2N. b) Δf(z) taken at the same time.(I_{set}=200 pA. V_{set} indicated in the legend).

and this effect comes into play.

4.5 Electric Field Induced State on NaCl-BL/Cu_2N

Experiments carried on bare Cu(001) and Cu_2N/Cu(001) [76] reveal no dramatic deviations from the expected exponential behaviour. In the case of NaCl-ML/Cu_2N/Cu(001), as described in the previous section, notable changes are only observed for small tip-sample distance at both positive and negative bias. For NaCl-BL/Cu_2N/Cu(001) no deviations are observed at negative bias if the tip-sample distances are large enough. However, as seen in Fig. 4.7, a sharp step in I is observed for the NaCl-BL/Cu_2N/Cu(001) at positive bias when a critical electric field is reached. Here, two different states can be distinguished: a high electric field state (at small Δz) with a relatively larger current, and a low electric field state (at larger Δz) with a relatively smaller current.

4.5.1 Electric Field Induced Transition: I(Δz) Measurements

Knowing what is triggering the transition can give us information about its nature. As it is related to two different currents and there is a relationship with bias, three different parameters may come into play: bias, current and electric field. For a constant initial tip height z_0, the critical distance increment (Δz_c) at which the transition occurs increases linearly as the applied bias increases (Fig. 4.7), suggesting that this phenomenon is induced by an applied electric field. Fitting the points to a linear trend gives us a critical electric field of the order of 1 V/Å(Fig. 4.7b); this remains

constant on specific NaCl-BL regions, but can vary by up to 50% for different tips and regions. Figure 4.8 shows equal slopes before and after the step for the different applied bias.

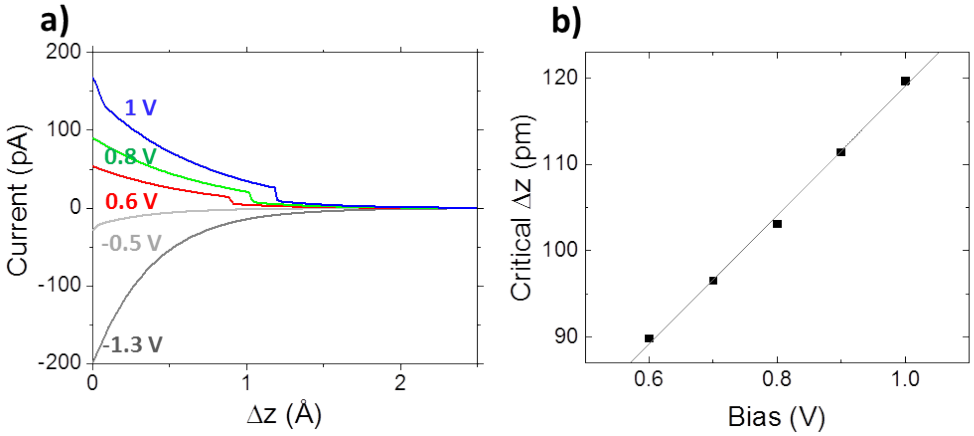

Figure 4.7: Electric-field induced switching of NaCl-BL/Cu_2N/Cu(001). a) I vs. Δz acquired above an NaCl-BL/Cu_2N/Cu(001). A clear step in I is observed for $V > 0$, but not for $V < 0$ (V_{set}=-1.3 V, I_{set}=200 pA). b) Change in the critical Δz vs. V, with a slope corresponding to a critical electric field Ec=1.33 $V/$.

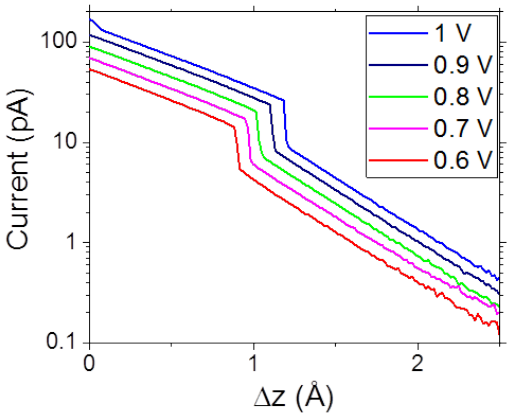

Figure 4.8: Electric-field switching previously showed in figure 4.7 in semilog scale. The graph denotes linear behaviour with two well-defined slopes before and after the switch (V_{set}=-1.3 V, I_{set}=200 pA).

For the previous I(Δ z) series, current decays before and after the transition are fitted to exponential functions (Fig. 4.9a). Fits show two well defined decay lengths, which are independent of the applied bias once a critical electric field is overcome (Fig. 4.9b). This result is reproducible at different positions in the sample and also with different tips. This, indicating a general trend, suggests that the decay length of the high electric field state is always larger than the low state and is constant for different

applied bias. The variation in the measured decay length might be due to the different gap geometries among the different measurements (Fig. 4.10) . For instance, a small tip-sample distance modifies the the exponential decay and then modifying the decay length if it is adjusted to a simple exponential.

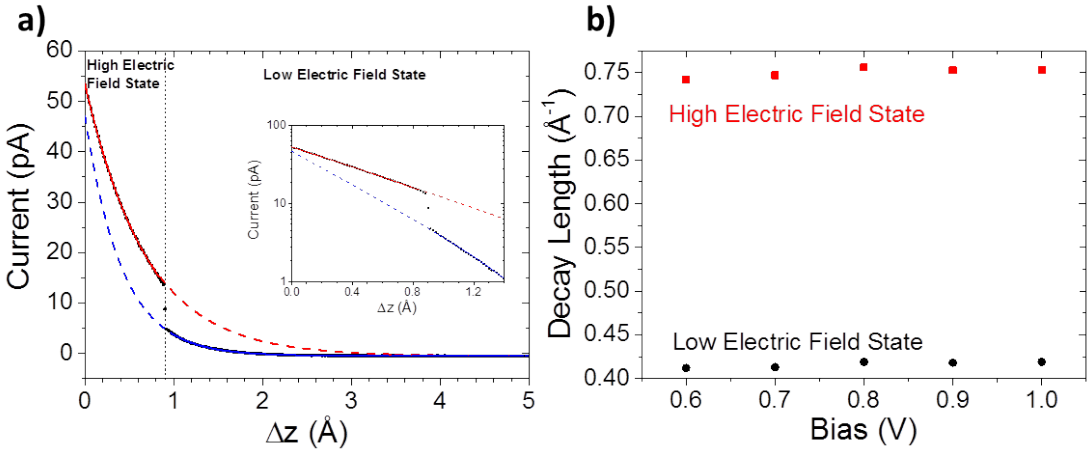

Figure 4.9: Decay length dependence with the state. a) Fit of two exponentials with different decay length, before and after the transition. Inset shows the same graph on semi-log scale. Two markedly different slopes can be observed. b) Decay length independence of the effective electric field.

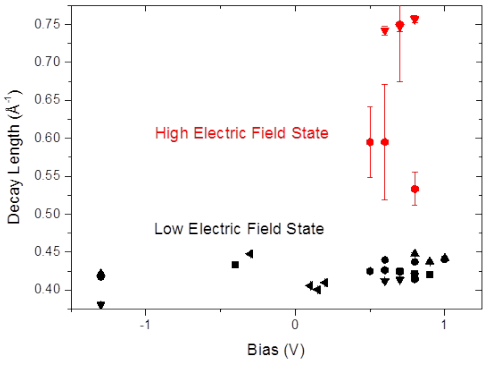

Figure 4.10: Decay length of low and high electric field states (black and red) through different tips and areas (shape of the point data) over NaCl-BL/Cu_2N/Cu(001).

4.5.2 NaCl/Cu_2N/Cu(001) Structure in the Presence of an External Electric Field: DFT Calculations

Since the tunnelling barrier height is related to the surface dipole moment (which has been previously discussed), it is natural to interpret the sharp change in current as arising from a modification of the position of the ions of NaCl layers. As seen

in Fig. 4.11a, DFT calculations indicate that the heights of the Na and Cl ions in the top NaCl layer vary in the presence of an electric field, and that for fields larger than approximately 0.5 V/Åthe rumpling is reversed, with the Na atom shifting to be above the Cl atom. At a fixed location above the NaCl-BL, the integrated LDOS (which is proportional to I) also increases significantly for electric fields above this value (Fig. 4.11b); as the figure shows, the data at 0.25 and 0.75 eV overlap the data at 1.25 eV when multiplied by a factor of 5 and 1.5 respectively. Therefore, it is not a variation of the electronic structure with impact at some energies but a variation of the work function inducing the same relative changes of the integrated LDOS at any energy. We note that the calculations correspond to an infinitely wide layer of NaCl-BL/Cu_2N/Cu(001) subjected to a uniform electric field. This may explain why the calculations show a continuous change in both the position of the ions as well as the integrated LDOS while our experiments show a sharp transition. Finite size effects might evidence not only a sharp change of the state, but an incipient ferroelectricity, fast reversal of the polarization by means of applied electric fields. It is well known that polarization reversal in ferroelectric materials are in the order of 10^{-9} s [78].

4.5.3 Electric Field Induced Transition: Δf(Δz) Measurements

To further confirm the nature of the transition, we performed simultaneous STM and AFM measurements above the NaCl/Cu_2N/Cu(001) layers. As it was mentioned previously, the tip is approximately 3 Åabove the outer NaCl layer at regular scanning conditions (V_{set}=-1.3 V, I_{set}=30 pA) making it possible to approach to the surface without using high currents that may damage the surface. Previous studies suggest that three contributions should be dominant in the interactions between the tip and the substrate [24]: a chemical interaction described by a Lennard-Jones potential, which has a characteristic minimum at intermediate distances separating an attractive regime at large distances from a repulsive regime at small distances; a longer range attractive van der Waals interaction; and a electrostatic term term arising mainly from the contact potential difference between the two sides of the junction [90].

As it is seen for I(Δz), two different regimes can be distinguished in $\Delta f(\Delta z)$ measurements: a ground state that occurs for negative and low positive electric fields, and a second state that is triggered when the positive electric field exceeds a threshold

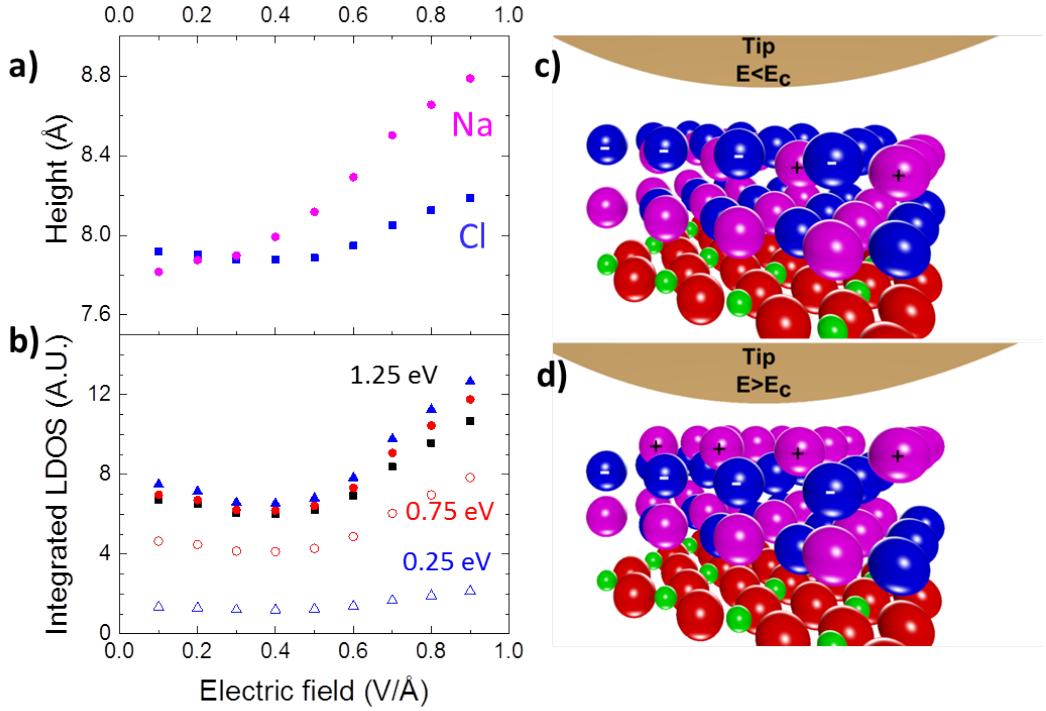

Figure 4.11: Shifting of atoms in NaCl-BL/Cu_2N/Cu(001). a) Calculated height of the topmost Na (magenta) and Cl (blue) atom as a function of applied electric field. b) Integrated LDOS at a fixed point (approximately 0.25 Åabove the NaCl surface) as a function of applied electric field for 0.25, 0.75 and 1.25 eV. Empty dots correspond to the integrated LDOS for different energy. Blue and red solid dots are 0.25 and 0.75 eV multiplied by a constant factor of 1.5 and 5 respectively, evidencing that the tendency is the same independently of the energy and only depends on the applied electric field. c) Illustration of the positions of Cu (red), N (green), Na (magenta), and Cl (blue) atoms in NaCl-BL/Cu_2N/Cu(001) for the low electric field configuration, as defined by DFT calculations for E=0 V/Å. In the outermost layer, the Cl- atoms sit above the Na atoms and are thus closer to the tip above. d) Same as (c) for the high electric field configuration, as defined by DFT calculations for E=0.9 V/Å. In the outermost layer, the Cl- atoms are now below the Na atoms, indicating a reversal of the rumpling and therefore dipolar orientation.

called critical electric field. This behaviour on $\Delta f(\Delta z)$ can also be observed on the low electric field state regime.

As seen in Figs. 4.12a and 4.12b, the measured $\Delta f(\Delta z)$ matches the expected sum of these three contributions (Fig. 4.12d) for negative bias above both Na and Cl sites on the NaCl-BL/Cu_2N/Cu(001) which are the Lennard-Jones potential, accounting for the chemical forces; van der Waals force, which is the interaction between induced tip-sample dipoles, and electrostatic interaction. However, as in the case of the I(Δz) measurements shown in Fig. 4.7, a transition in $\Delta f(\Delta z)$ is observed as a sharp drop in

Δf that shifts linearly in Δz with the applied bias; the minimum in $\Delta f(\Delta z)$ also shifts with V.

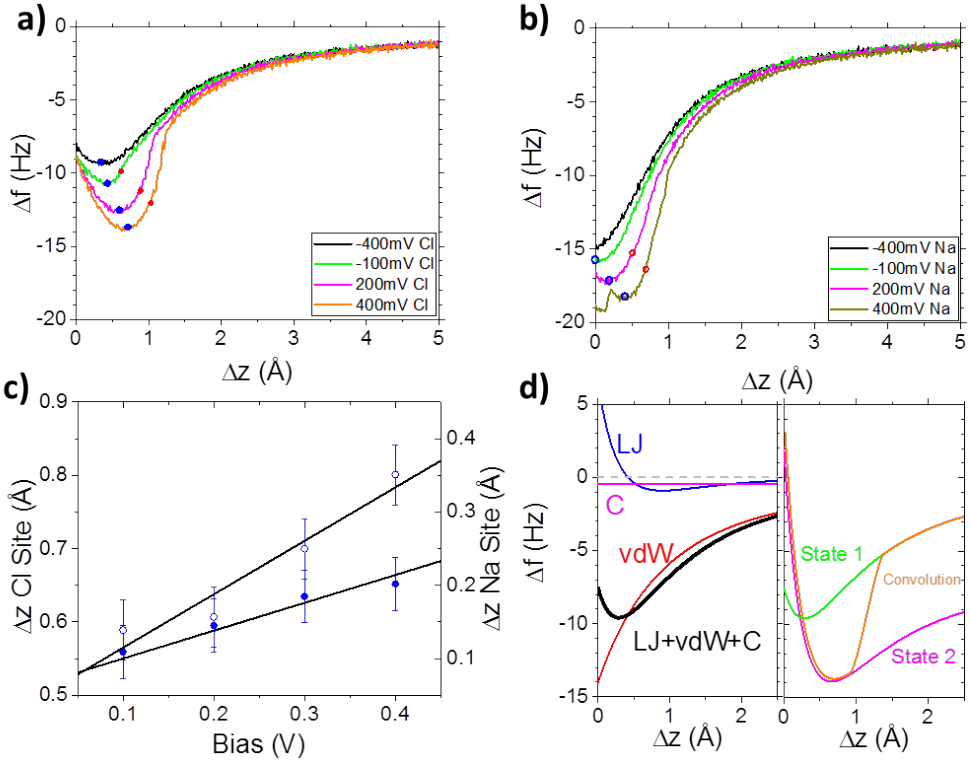

Figure 4.12: Force measurements for NaCl-BL/Cu_2N/Cu(001). a) $\Delta f(\Delta z)$ measurements for NaCl-BL/Cu_2N/Cu(001) acquired above a Cl atom with V=-400 mV (black), -100 mV (green), 200 mV (magenta), and 400 mV (yellow). (V_{set}=-0.4 V, I_{set}=200 pA) Blue dots indicate the location of the minimum Δf value, and red dots indicate the location of the deconvoluted step observed in simultaneously obtained I vs Δz measurements. b) Same as panel a but with the tip kept at a constant vertical height and laterally displaced to be positioned over an Na atom c) Shift of the minimum in$\Delta f(\Delta z)$ vs V obtained above Cl (solid circles) and Na (open circles) sites. d) Left panel shows a sketch of the individual components contributing to the $\Delta f(\Delta z)$ curve âĂŞ including the Lennard-Jones (black), van der Waals (red), and constant electrostatic (purple) terms âĂŞ as well as their sum (blue). Right panel shows the expected $\Delta f(\Delta z)$ curve for the low field (green) and high field (magenta) states, as well as their convolution (orange).

Furthermore, the value for E_c is very close to the one retrieved from I(Δz) (Fig. 4.13). Intriguingly, measurements performed with the tip at constant height on top of a Cl and a Na atom (Fig. 4.12a,b) show the same overall trends but with clear differences. The different shape in $\Delta f(\Delta z)$, and more particularly the height Δz at which the Δf minimum is achieved, is due to differences in the chemical interaction between the tip and the two atomic species [91]. Figure 4.12c shows the different trends in the

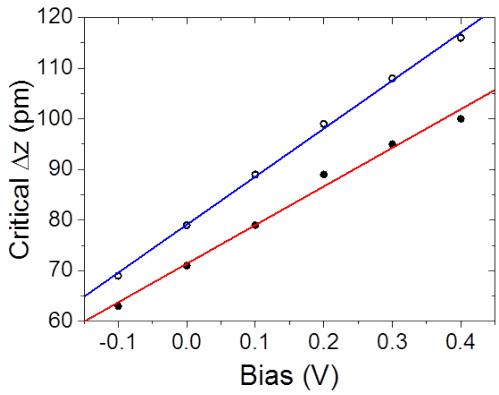

Figure 4.13: Change in the Δz_c vs. V measured in Δf (black empty dots), with a slope corresponding to a critical electric field E_c=0.76 $V/$. Change in Δz_c vs. V measured in Δf extracted from the deconvolution of the current explained in Supp. Fig. 4 , with a slope corresponding to a critical electric field E_c=0.96 $V/$ ((Vset=-1.3 V, Iset=200 pA).

shift of the $\Delta f(\Delta z)$ minimum with V.

4.5.4 Correlation of the transition between I(z) and Δf(z) measurements

Because of the oscillation of the tip, the sharp transition in simultaneously acquired I(Δz), shown in Fig. 4.12, is broadened [92]. To deconvolute the influence of the oscillation, we fit the I(Δz) spectrum to two exponentials coupled by a sharp step (as is observed when the oscillation is not present); these are mixed by a semi-circular function [93] to average contributions over different parts of the oscillation cycle with a radius equal to the oscillation amplitude.

In the absence of any tip oscillation, the current can be modelled as:

$$I(\Delta z) = I_1 e^{-k_1 \Delta z} \theta(\Delta z_c) + I_2 e^{-k_2 \Delta z} (1 - \theta(\Delta z_c)) \tag{4.4}$$

where $I_1 = I(V, \Delta z = 0)$ in the low field state and $I_2 = I(V, \Delta z = 0)$ in the high field state; k_1 is the decay length in the low field state and k_2 in the high field state, which can be described as $k_{1(2)} = 2\sqrt{\frac{2m(<\phi_{1(2)}> - eV)}{\hbar^2}}$ with $<\phi_{1(2)}>$ the apparent potential barrier energy (average of the tip's and surface's workfunctions) for state 1 (2);$\theta(\Delta z)$ is a step function with $\theta = 1$ for $\Delta z > \Delta z_c$ and $\theta = 0$ for $\Delta z < \Delta z_c$.

If the tip is oscillating, then I(Δz) must be convoluted over the range of motion of the

tip. This can be done with a semi-circular function, yielding:

$$I'(\Delta z) = \frac{2}{\pi \xi^2} \int_{-\xi}^{\xi} I(\Delta z + x) \sqrt{\xi^2 - x^2} \mathrm{d}x \tag{4.5}$$

This yields an oscillation amplitude of 0.22 Å, which is consistent with other independent measurements of the oscillation amplitude, and a Δz_c that matches the transition in $\Delta f(\Delta z)$ (as illustrated in Fig. 4.12a,b to Fig. 4.14).

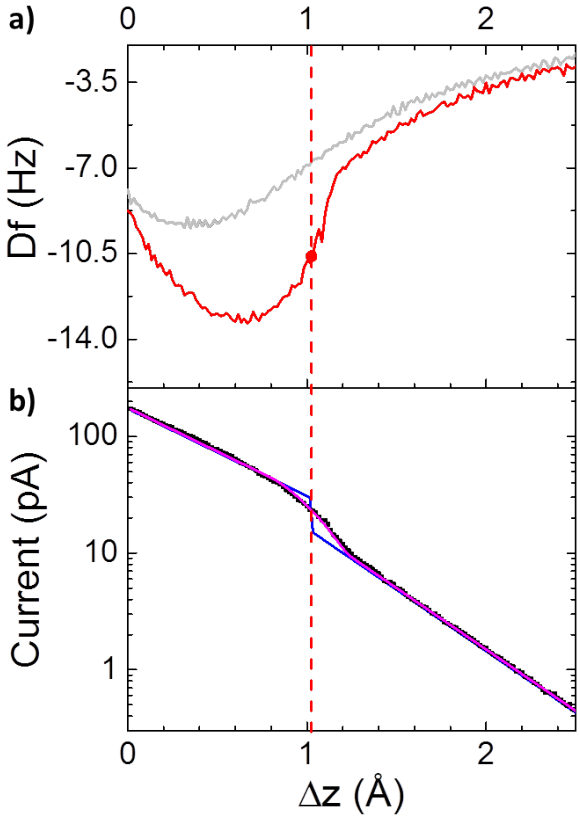

Figure 4.14: $I(\Delta z)$ and $\Delta f(\Delta z)$ electric field induced switching transition comparison. a) Experimental $\Delta f(\Delta z)$ of two different applied bias -0.4 V (grey) and 0.4 V. Red dot denotes where the transition occurs according to $I(\Delta z)$ deconvolution. b) Experimental $I(\Delta z)$ for 0.4 V (black dotted line). Convolution fit for 0.4 V (magenta line) and deconvoluted $I(\Delta z)$ (blue line)with a critical Δz of 1.03 Å.

The I(Δz) spectrum with a step can be described by three distinct parts: i) a high electric field current decay with a characteristic workfunction; ii) a low electric field current decay with a different characteristic workfunction; and iii) a sharp step representing the transition between the two prior states.

4.5.4.1 A simple model for the understanding of the transition in Δf

To interpret the transition, $\Delta f(\Delta z)$ curves were modelled with the three terms described before and illustrated in Fig. 4.12d. In this simple model the sum of the three forces describes the interaction between the tip and the sample, which have been already described in chapter 3:

$$F(z) = F_{chem} + F_{vdW} + F_{el} = \frac{12\varepsilon}{z_m}\left(\left(\frac{z_m}{z}\right)^{13} - \left(\frac{z_m}{z}\right)^{7}\right) - \frac{HR}{z^2} + \frac{1}{2}\frac{\partial C}{\partial z}V^2 \quad (4.6)$$

Non-contact atomic force microscopy measures the frequency shift from the resonance frequency, which is proportional to the negative derivative of the force [24]. Since for our measurements the variation of the centre of the parabolic electrostatic term with Δz is not significant, we model the electrostatic term as a constant Δf_0 (Fig. 4.15). Therefore, we find that:

$$\Delta f \propto -\frac{dF}{dz} = \frac{12e}{z_m}\left(\frac{13z_m^{13}}{z^{14}} - \frac{7z_m^7}{z^8}\right) - \frac{HR}{3z^3} + \Delta f_0 \quad (4.7)$$

The acquired $\Delta f(\Delta z)$ signal will have contributions from both the low field state (1) and the high field state (2) if an oscillation cycle extends over both:

$$\Delta f_1(\Delta z) \propto \frac{12e}{z_m}\left(\frac{13z_m^{13}}{(\Delta z + z_1)^{14}} - \frac{7z_m^7}{(\Delta z + z_1)^8}\right) - \frac{HR}{3(\Delta z + z_{vdW})^3} + \Delta f_0^{(1)} \quad (4.8)$$

$$\Delta f_2(\Delta z) \propto \frac{12e}{z_m}\left(\frac{13z_m^{13}}{(\Delta z + z_2)^{14}} - \frac{7z_m^7}{(\Delta z + z_2)^8}\right) - \frac{HR}{3(\Delta z + z_{vdW})^3} + \Delta f_0^{(2)} \quad (4.9)$$

where $z_{1(2)}$ is the height of the target ion in states 1(2), and z_{vdW} is the average distance between the tip and sample regions contributing to the van der Waals interaction. Since the oscillation of the tip is not negligible, the final signal will be the convolution of Δf_1, Δf_2, and a sharp step that separates both states with a semi-

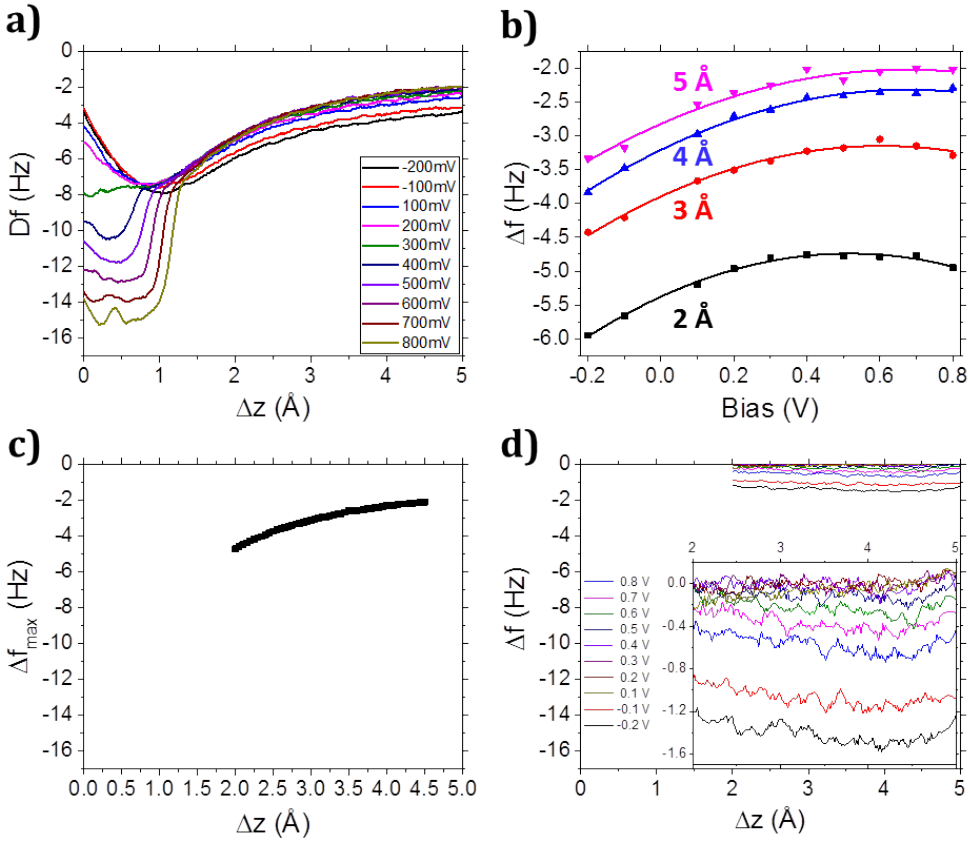

Figure 4.15: Electrostatic contribution to Δf. a) $\Delta f(\Delta z)$ spectrum obtained over NaCl-BL/Cu2N/Cu(001) at different applied voltages. (V_{set}=-0.2 V,I_{set}= 200 pA). b) Same data shown in panel a but plotted as Δf(V) for different values of Δz. c) Maximum value of Δf obtained from a parabolic fit of Δf(V), where the electrostatic contribution to Δf is zero providing the electrostatic potential compensated Δf. d) $\Delta f(\Delta z)$ - Δf_{max} at different values of V, which represents the electrostatic contribution to Δf. The z range corresponding to the high electric field state is not analized because the parabolic shape is distorted by the transition, and there is not enough bias range to extract Δf_{max} reliably.

circular function that broadens the transition:

$$\Delta f(\Delta z) \propto \frac{2}{\pi \xi^2} \int_{-\xi}^{\xi} \left(\Delta f_1 (\Delta z + \chi)(1 - \theta(\Delta z)) + \Delta f_2 (\Delta z + \chi)\theta(\Delta z)\right) \sqrt{\xi^2 - \chi^2} dx \tag{4.10}$$

where $\theta(\Delta z)$ is a step function with θ=1 for $\Delta z < \Delta z_c$ and $\theta = 0$ for $\Delta z > \Delta z_c$.

To fit the $\Delta f(\Delta z)$ spectra for the low field state (1), we first fit an average of the last 2.5 Åin Δz obtained at different negative and positive bias voltage (where no transition occurs) on both Na and Cl sites. Because the Lennard-Jones contribution at these large values of Δz is negligible, we can obtain the van der Waals and electrostatic

terms. Having determined these values, we then use them to fit the full Δz range and extract the value of the Lennard-Jones term.

When convoluting the Δf spectra for state 1 and state 2 as described above, we use the same values obtained from fits for state 1 for all parameters, except for $z_{1(2)}$ and Δf_0.

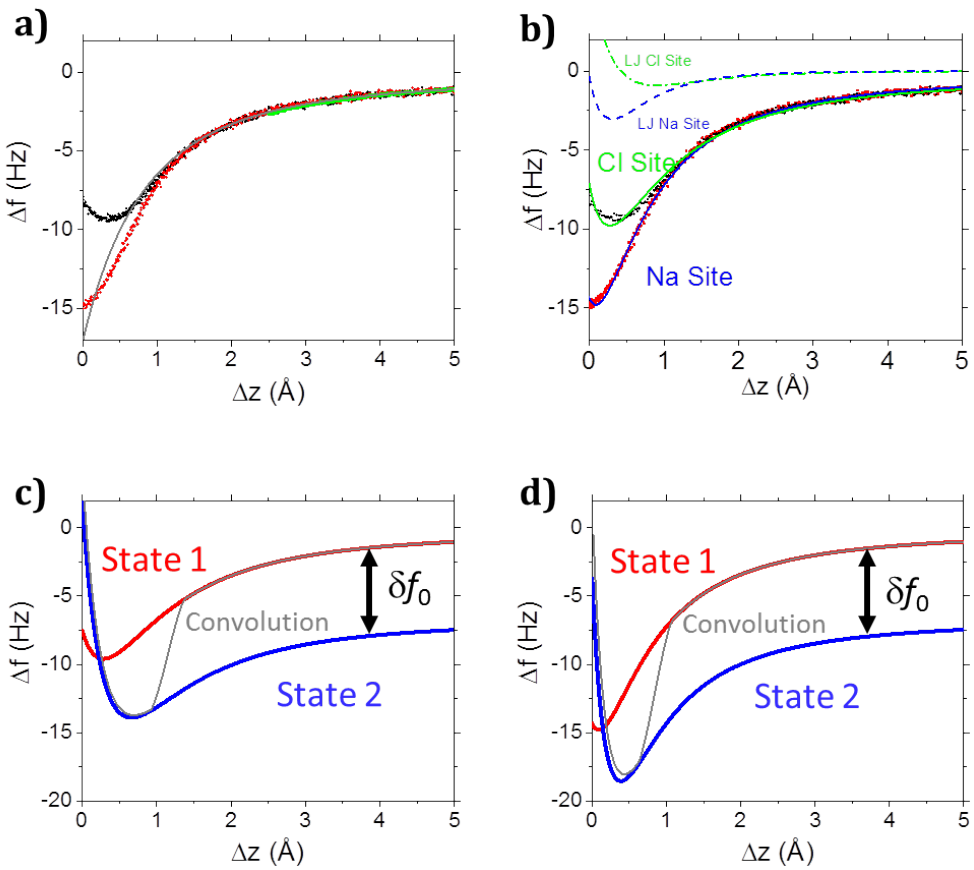

Figure 4.16: Model for the transition in Δf. a) $\Delta f(\Delta z)$ spectrum obtained over a Cl (black) and Na (red) atom at constant height. The last 2.5 Åmatches at all measured values of V on both Na and Cl sites; an average of these curves (green) is fit (grey) to obtain the van der Waals and electrostatic terms. b) Same $\Delta f(\Delta z)$ spectra as shown in panel a, with fits of the full range for Cl (green) and Na (blue) sites shown. The fits use the van der Waals and electrostatic terms obtained in panel a, and now include a Lennard-Jones term that is different for each site (dashed green and blue lines). c) Transition from state 1 to state 2 and its convolution for Cl site. $\delta f_0 = \Delta f_0(2) - \Delta f_0(1)$ indicates the offset of the curve due to the change in the electrostatic term. d) Same as panel c) for the Na site. Note that δf_0 is found to be the same as for the Cl site, suggesting a non-local transition. The shift of the ionic positions ($z_2 - z_1$, see equations below) necessary to describe the $\Delta f(\Delta z)$ dependency in the presence of the transition amounts to about 0.35 Å, although an accurate value of z_2 cannot be retrieved because the Δz region where the high field state is visible is very narrow.

Once the model is presented we can finally describe the transition. The Lennard-Jones potential accounts for short range interactions, and therefore it must be sensitive to the ion displacement beneath the tip. Thus, in Fig. 4.12d the ion position ($z_{1(20)}$)) is changed in the L-J term to reproduce the shift of the minimum upon the transition. This indicates that the different trends in the shift of the $\Delta f(\Delta z)$ minimum with V can be ascribed to Na and Cl atoms shifting their position differently with the applied electric field, in agreement with DFT calculations (4.11). On the other hand, the van der Waals contribution and the electrostatic term are longer range interactions, and they are not atomic site sensitive [90]. In consequence, in the model we keep constant the van der Waal's contribution for both ions and in both states. But in order to reproduce the Δf drop occurring at the transition, we add a constant term that is the same for Na and Cl, which represents a change in the electrostatic force. The change has the same origin as the change in decay rate reported in Fig. 4.7: a change in the surface dipole because of the applied electric field. As with the I(Δz) spectra, convoluting both $\Delta f(\Delta z)$ curves with a sharp step and a semi-circular function which has been previously defined, it gives us an approximate model that successfully reproduces the transition in $\Delta f(\Delta z)$ (Fig. 4.12d). Although this simple model is not able to match perfectly both curves with the transition, it verifies a necessary change in the dielectric constant arising from a change of the electrostatic term [24], shifting downwards the overall curve (Fig. 4.16). The identical contribution of the electrostatic term for Cl and Na site suggests that it has a long-range nature. This indicates a non-local change of the NaCl-BL structure, which might be occurring in a domain, rather than globally as illustrated Fig. 4.11c. We note that Kelvin probe measurements reveal a sharp drop in Δf when the transition occurs (Fig. 4.17).

4.5.5 Influence of the Contact Potential Difference

If two metals with different work functions are separated, their vacuum levels are aligned. When they are in electrical contact (zero potential drop between them), their Fermi levels will align and then, the electrons will flow from the metal with lower work function into the metal with the higher one. The charges will accumulate on the surface leading to space charge and then, their electric fields will push electrons back until an equilibrium is reached. This will lead into a potential difference which is

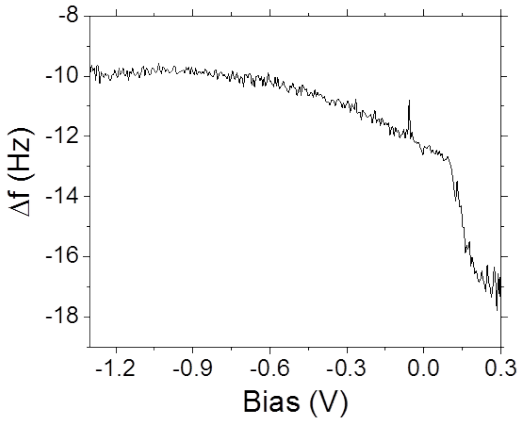

Figure 4.17: Kelvin probe parabola measured on top NaCl-BL/Cu_2N/Cu(001) with the transition at 0.1 V.

called contact potential difference (CPD), which is defined as the difference in work function between the tip and the sample $CPD = (\Phi_2 - \Phi_1)/e$.

Contradicting apparently the simplest theory, Δf(Δz) measurements taken on NaCl-BL/Cu_2N/Cu(001) have yielded intriguing results. The transition at a given critical electric field is observed not only at positive bias (Fig. 4.18a) but also at a moderate low negative bias in some cases (Fig. 4.18b).

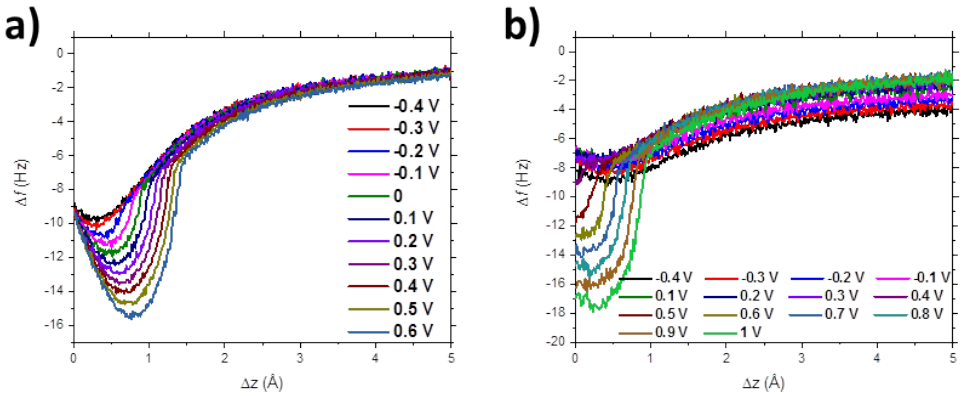

Figure 4.18: Electric field induced transition dependence on the V_{CPD}. a)Δf(Δz) with the transition starting at -0.2 V. b) Δf(Δz) with the transition starting at 0.5 V.

Although no Δf(V) measurements were performed with the same tip on the same area of $\Delta f(\Delta z)$ still information about the contact potential resulting parabola can be extracted. In this experiment, different $\Delta f(\Delta z)$ measurements are performed at the same initial height, and then, plotting Δf against bias can give us the resulting Kelvin probe parabola. Fig. 4.19 shows the evolution of the Kelvin probe parabola at

different heights. As in previous works, the center of the parabola shifts with height [90]. At closer distance, less surface of the sample (accounting NaCl-ML/Cu_2N and Cu_2N) will be averaged while at larger tip sample distances, due to the nature of this interaction (long range) other parts of the sample will be averaged. This consequently will lead to a modification of the average work function. The second remarkable fact is that Fig. 4.19a shows the parabola center at negative bias while Fig. 4.19b shows the parabola center at positive bias indicating that the V_{CPD} can be either positive or negative depending of the tip termination.

It is important to remark that the center of the measured parabola corresponds to the bias that cancels the force due to the V_{CPD} and hence the center of the parabola V^* is defined as $V^* = -V_{CPD}$.

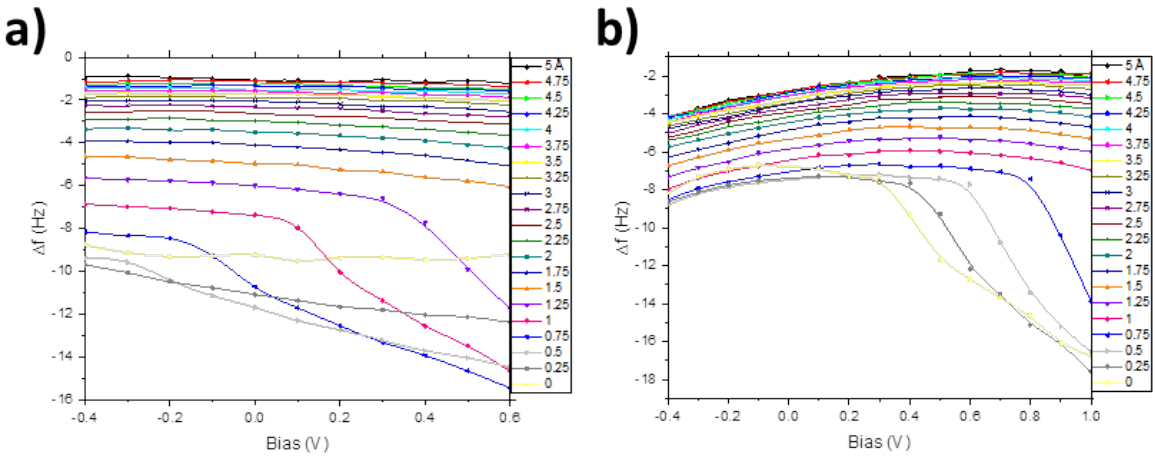

Figure 4.19: Kelvin probe parabolas of previous $\Delta f(\Delta z)$. Two V_{CPD} values can be distinguished at the two different parabolas. The legend shows the parabola at different heights from Δz=0, which is the height at the initial setpoint conditions (V_{set}=-0.4 V, I_{set}=200 pA)to 5 Å. a) Shows the parabola center at negative bias with with a transition starting at 1.25 Å. b) Shows the parabola center at positive bias, with a transition occurring at 0.75 Å.

With the help of the previous discussion, it is easy to conclude that V_{CPD} will be positive for Fig. 4.19a and negative for Fig. 4.19b. This implies that in the absence of an applied bias, the effective electric field will be negative and positive respectively (in a reference frame with the surface normal as positive direction).

With this simple model it is easy to understand how a transition at zero applied bias or even at negative bias is possible: if the effective electric field is still positive and enough to overcome the critical electric field. Additionally a transition at high pos-

itive applied bias implies a negative electric field in the absence of applied bias, increasing the calculated electric field for the transition to happen.

4.5.6 Electric Field Induced Transition on Vacancies: From Piezoelectricity to Ferroelectricity

Previous sections have shown the possibility of controlling a surface dipole layer at the atomic scale through applied electric fields. This behaviour has been observed for a defect free NaCl-BL/Cu_2N/Cu(001) layer. The fact that there are two well defined polarization states separated by a sharp transition may indicate a possible incipient ferroelectricity in this system.

Previous studies have characterized Cl vacancies of NaCl deposited onto different metallic substrates [94]. Structural similarities between past studied Cl vacancies in NaCl and our naturally found defects lead us to think they are the same phenomenon, Cl vacancies.

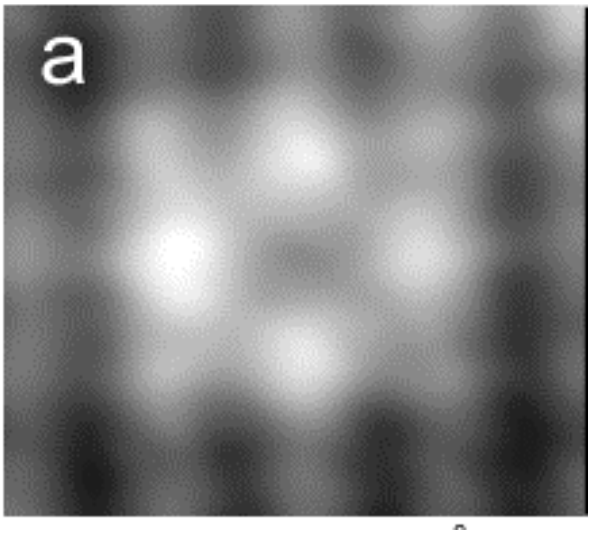

Figure 4.20: Artificially created Cl vacancy on two layers of NaCl on Cu(001) (V_{set}=152 mV, I_{set}=200 pA) [94]. *Permission to reproduce this graphs has been granted by Physical Review Letters.*

Performing the same experiment (variation of the electric field) on top of these defects, as for instance Cl vacancies (Fig. 4.21) show striking results.

The electric field induced transition shows hysteretic behaviour which can be observed in the tunnelling current (Fig. 4.22a) as well as in force spectroscopy (Fig. 4.22b): a clear change in the parabola center and its curvature. Surprisingly

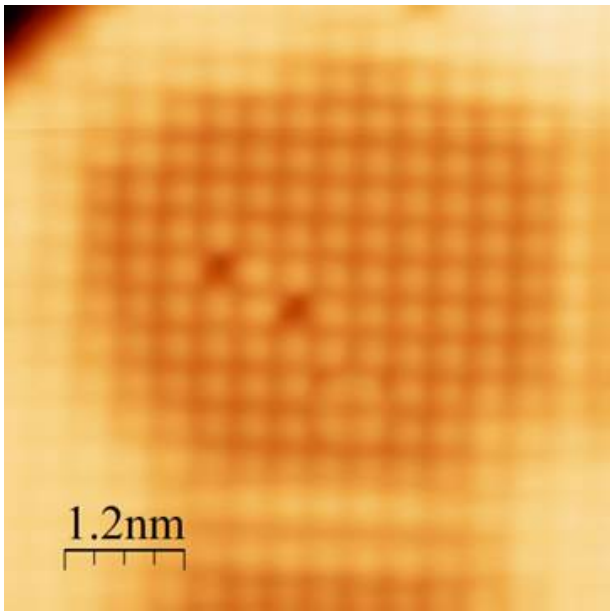

Figure 4.21: STM image of NaCl-BL/Cu_2N/Cu(001) with two Cl vacancies. (I_{set}=50 pA, V_{set}=-1.3 V

this hysteretic behaviour has not only been detected on top of a defect of NaCl-BL/Cu_2N/Cu(001) but also in the NaCl-ML in the same substrate.

In the same way dI/dV measurements show a shift in the differential conductance when swiching between both states. Figure 4.23 shows consecutive hysteretic cycles for different set points: 50, 100, 200 and 50 pA respectively. There are two remarkable facts: the bias at which the transition occurs shifts with tip-sample distance and the reproducibility in the process and the spectra at 50 pA are similar even if they were not performed consecutively. Again, the variation of the threshold bias with the regulation distance points to a electric field driven effect. For this purpose $\Delta I(\Delta z)$ measurements carried on a vacancy on NaCl-BL/Cu_2N/Cu(001) at different V_{set} (Fig. 4.24a). Plotting the critical distance against bias gives a linear behaviour as expected (Fig. 4.24b). The electric field dependence suggests that possibly the switch observed in the free-defect layer and the layer with vacancies is the same phenomenon.

These preliminary results show potential ferroelectricity at atomically thin insulating layers. Further characterization is needed support these findings, including better characterization of electric field dependence and for example obtaining atomically resolved structural characterization in both states. Nevertheless these results and their implication will be extended in the following chapter, where magnetic impurities (Co

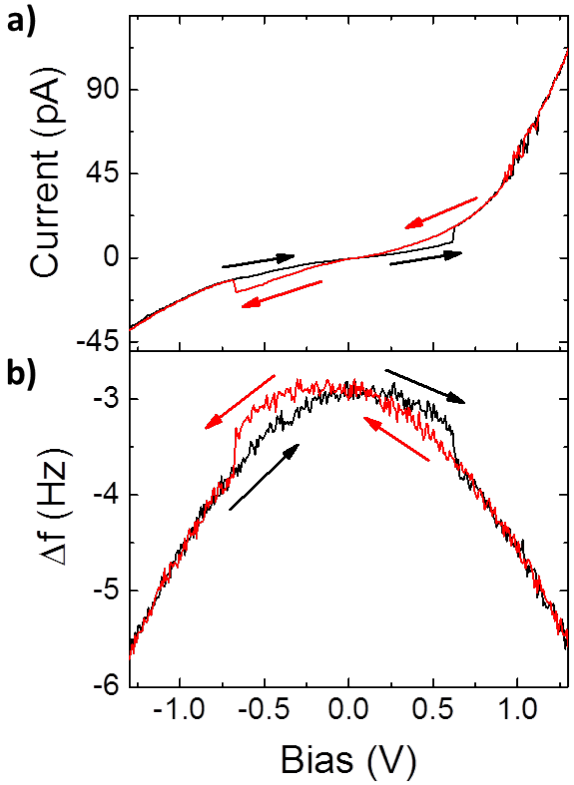

Figure 4.22: Ferroelectric behaviour on a Cl vacancy on NaCl-ML/Cu_2N/Cu. a) I (V) curve showing hysteresis through a sharp step and two characteristic curves. b) $\Delta f(V)$ curve showing both states with two very differentiated parabolas.

atoms) will be evaporated on top and their magnetic properties will be evaluated for different bistable states of the electric polarization.

4.6 Conclusions

In this chapter, we have demonstrated the existence of piezoelectricity on atomically thin stacks of NaCl over an insulating polar surface. This effect can be observed at positive electric fields as a sharp transition possibly due to inversion of surface dipoles of NaCl/Cu_2N/Cu. Furthermore, we have probed the consequences of close tip-sample distance, as elastic deformation of the tip or sample and its influence of the tunnelling barrier. Another important aspect has been observed; V_{CPD} has a big impact on the effective electric field affecting transitions triggered by the electric field. STM shows up as a powerful tool to measure atomic displacement at this unprecedented scale.

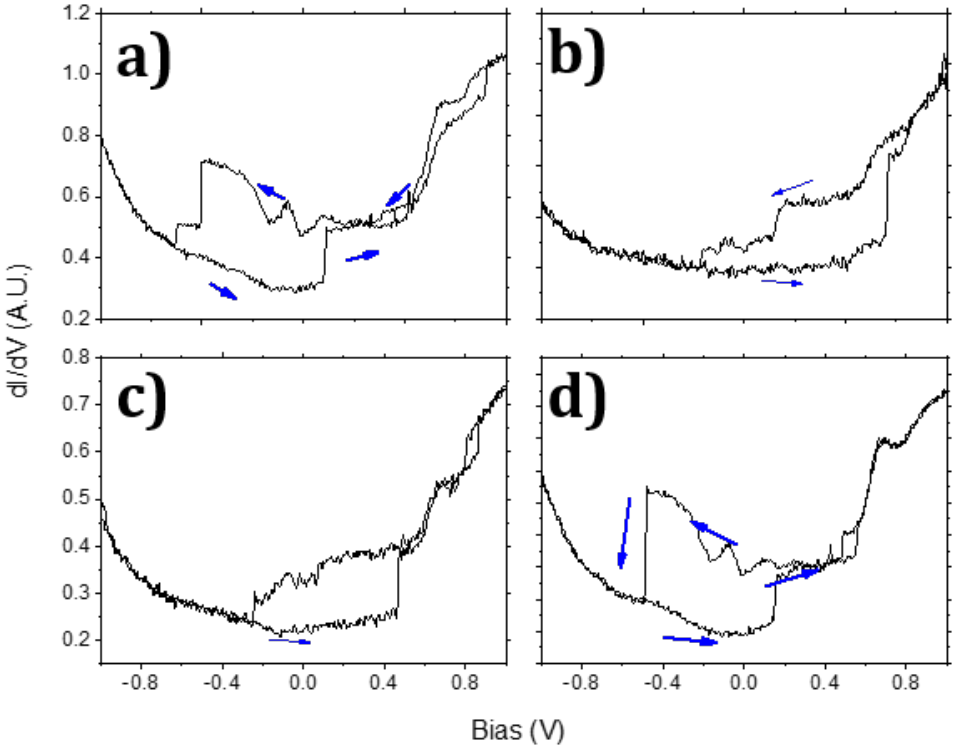

Figure 4.23: dI/dV spectroscopy over a Cl vacancy. Bistability crossing zero can be noticed as a signature of ferroelectricity. The measurements were taken with different current set points (50, 80, 120 and 50 pA) for a), b), c) and d) respectively. A shift of the transition can be noticed as well as the reproducibility of the spectroscopy between a and d.

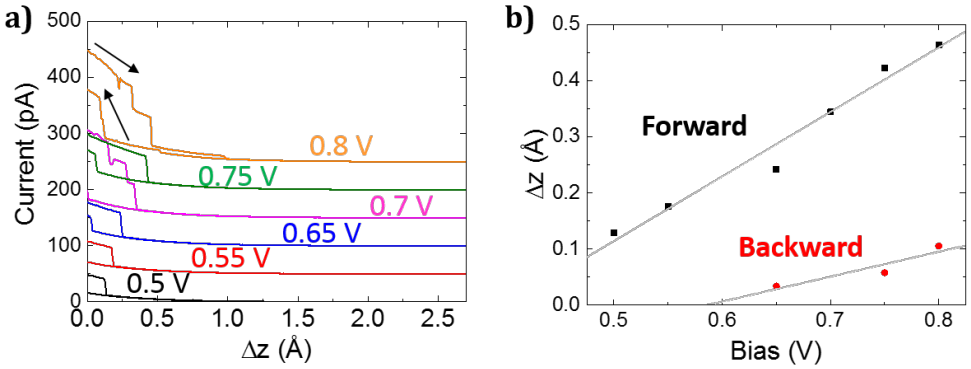

Figure 4.24: $\Delta I(\Delta z)$ on top of a vacancy for different set point bias. a) Shows a shift of the steps with the applied bias. b) Δz vs. Bias denotes an electric field driven process with two different slopes for forward and backward curves.

4.7 Future work

Demonstration of piezoelectricity at this scale opens the door for the study of switching of two stable states triggered by the electric field,in other words, ferroelectricity.

Complementary studies have shown that placing the tip over a defect on NaCl (what is likely to be a Cl vacancy) and ramping the bias (then using as a probe the current) shows a clear response with the electric field and what is more surprising, showing a bistability that crosses zero when performing I(V) measurements (Fig. 4.22a). Consequently, Kelvin probe parabola measured through the frequency shift suffers a dramatic change: the curvature and the center are strongly modified (Fig. 4.22b). Further experiments on this particular system will be required in order to attribute the transition to ferroelectric switching. The experiments will include: atomic force spectroscopy vacancy identification, electric field dependence, imaging on both ferroelectric states and the impact of the contact potential difference in the system.

Chapter 5

Co Atoms on NaCl/Cu_2N/Cu: Multiferroicity at the Atomic Scale

5.1 Abstract

Different strategies have been employed to create functional multiferroic materials [85], from single crystals that contain both ferroelectric and ferromagnetic properties to two-phase multiferroics [95]. As described in the previous chapter, a change in the orientation of the out-of-plane dipole in NaCl-BL on Cu_2N/Cu(001) is observed when large electric fields are applied locally using an STM tip. In addition it has been briefly shown that when a defect is present in NaCl-ML or BL/Cu_2N/Cu(001), a polarization reversal driven by an external electric field with two different remanent states at zero bias can be observed. This is a signature of ferroelectricity. By depositing single magnetic impurities (Co atoms) on top of or close to point defects in NaCl-ML/Cu_2N/Cu(001), a change in magnetic anisotropy is observed with the change in the electric polarization of the layer. This new two-phase multiferroic composite opens the door to experimentally study the origin of the magnetoelectric coupling at the atomic scale, which may eventually lead to the development of stable single atom memory that can be controlled with read-out schemes based on all electric means.

5.2 Introduction

A multiferroic material is defined as a material that exhibits more than one ferroic order parameter simultaneously, for instance ferroelectricity and ferromagnetism. Due

to physical constrains, there is a scarcity of ferromagnetic ferroelectrics: usually cation off-centering in ferroelectrics requires empty d-orbitals while the formation of magnetic moments requires partially filled d-orbitals [85, 95]. Since these compounds are rather unusual and they do not combine large and robust electric and magnetic polarizations at room temperature other strategies have been followed.

In two-phase multiferroic composites, an electric field induces strctural change in the ferroelectric that is passed on to the ferromagnet. This perturbation causes a change in the magnetization [96]. Two-phase multiferroic composites have been successfully implemented in tunnel junctions demonstrating that it is possible to preserve magnetoelectric coupling at least to a thickness of 2 nm for the ferroelectric layer [86].

As described in previous chapters, limited progress has been made in the study of these compounds with STM due to their insulating nature. Some studies have reported magnetoelectric coupling on metals [97, 98]. Nonetheless, they are not based on ferroelectric order and thus do not exhibit bistability.

On the other hand, recent advances have been achieved on the study and characterization on single atoms adsorbed on different surfaces. By depositing Co atoms on top of MgO, the magnetic anisotropy (see introduction chapter for a detailed description of magnetic anisotropy) limit has been reached for a 3d metal atom [61]. In addition, atomic scale memory has been achieved using chains of Fe atoms on Cu_2N [99] built by atomic manipulation, and Co atoms on antiferromagnetic substrates [100]. Although past experiments have shown a possible stabilization of the magnetic moment in the order of minutes for Ho atoms on Pt(111) [101], more recent work has shown by X-ray magnetic circular dichroism (XMCD) indicates that hybridization with the metallic host prevents such a long lifetimes for the these atoms [102, 103]. Nonetheless, recent breakthroughs have been achieved by depositing Ho atoms on top of MgO bilayers on Ag(100), which show magnetic remanence with a relaxation time of 1500 seconds [104]. In this way, bistable single atoms have been achieved. Pursuing single atom memories represents the ultimate memory density in a storage device.

Consequently, by combining a potentially ferroelectric structure (as suggested with NaCl/Cu_2N/Cu(001)) with Co atoms it would be possible to create a single atom

two-phase multiferroic device, where the magnetocrystalline anisotropy is manipulated with the two electric polarizations existing in this system. A change in the crystal environment should be turned into a modified magnetic energy spectrum, visible through the spin-flip processes processes present in low bias inelastic tunnelling spectroscopy (IETS).

5.3 Influence of NaCl on Neighbouring Co Atoms on Top of Cu_2N

The local electrostatic environment is coupled to atomic spin-flip processes in adsorbed single atom impurities via crystal field effects. Therefore a change in the crystal field will influence the magnetocrystalline anisotropy [105]. Prior studies on Cu_2N have extensively reported inelastic excitations on adsorbed single magnetic impurities [40, 41, 42, 43, 106]. Co atoms on top of Cu sites on Cu_2N, not only show inelastic excitations at 5 meV but also Kondo excitations (Fig. 5.1a). In the case of a Co atom in Cu_2N, the total spin is 3/2 while the ground state corresponds to the third component of spin moment, m, equal to $\pm$1/2 (Fig. 5.1b). With this configuration two processes are coupled to the tunneling current. Kondo screening of the ground state appears as an elastic zero bias peak, while inelastic excitations between the ground and first excited state (m=$\pm$1/2 and $\pm$3/2 respectively) show up as conductance steps at both sides of the Fermi level. At B=0, $\pm$1/2 and $\pm$3/2 are pairs of degenerated spin doublets, and then, there is one single inelastic transition, which corresponds to the magnetic anisotropy energy (MAE) splitting. By increasing the coverage of Cu_2N and growing larger Cu_2N islands on a saturated surface [107], it is possible to suppress Kondo interactions with the underlying Cu(001) substrate and tailor the value of the MAE splitting [42].

As previously mentioned, crystal field induced effects are responsible for magnetocrystalline anisotropy, which can be probed by IETS. Therefore, the ground state of transition metal atoms will be strongly affected by the crystalline structure of the local environment. In this section, low bias spectroscopy will be performed on Co atoms placed on Cu_2N separated only a few atomic distances from NaCl-ML/Cu_2N/Cu. The influence of the neighbouring polar layer is evidenced in the modification of the

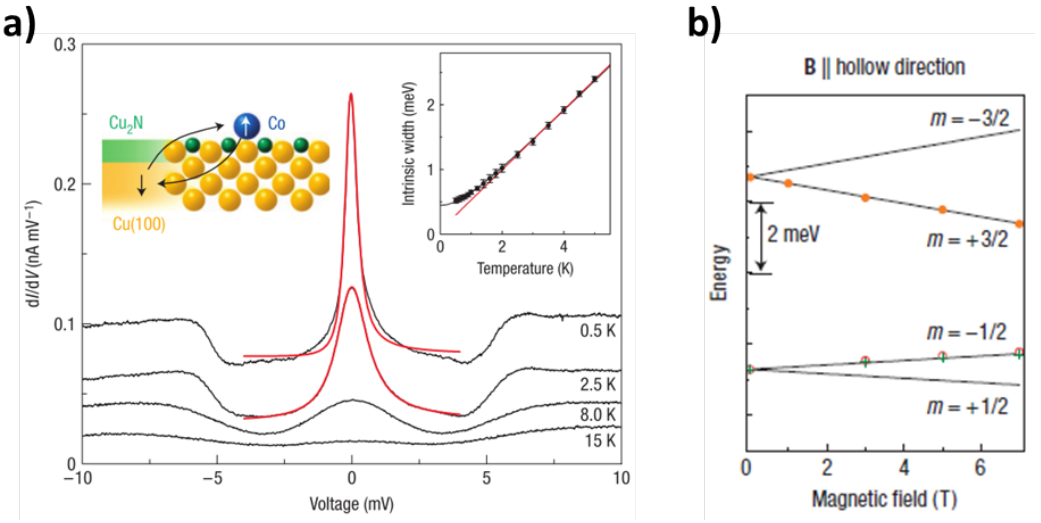

Figure 5.1: a) Co on a Cu site on Cu_2N spectra dependence with temperature. b) Energy eigenlevels for B parallel to hollow direction. [43]. *Permission to reproduce this images has been granted by Nature Physics.*

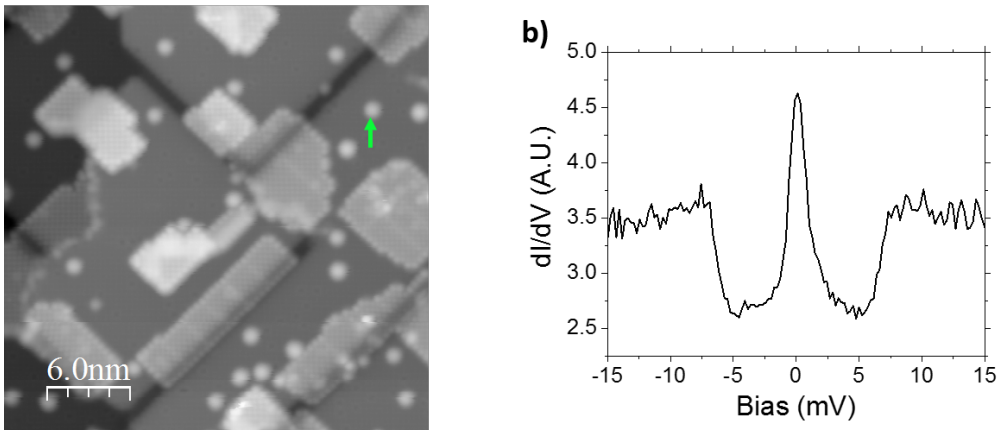

Figure 5.2: Co atoms evaporated on top of NaCl/Cu_2N/Cu(001). a) Image of the system taken at V_{set}=-1.3 V, I_{set}=10 pA. Green arrow indicates where the spectrum on panel b) was taken. b) Co spectrum on top of Cu_2N for T=1.1 K, V_{set}=-15 mV, I_{set}=200 pA. Kondo resonance at Fermi level can be observed in combination with inelastic excitations at around ±5 mV.

spin-flip processes.

In our experiments, we deposit Co atoms while the substrate is held at 4 K. Figure 5.2a shows the NaCl/Cu2N/Cu(001) surface after evaporation. Adsorbed atoms can be seen on top of NaCl-ML, Cu_2N and very close to NaCl-ML. As in the case of Cu_2N the atoms on NaCl-ML are seen as bright spots but with a lower apparent height relative to the underlying surface. Figure 5.2b shows a prototypical low bias spectroscopy on top of a Co over Cu_2N (Fig. 5.2a). In the saturated Cu_2N layer the MAE, i.e. the energy of the center of the inelastic step, may vary with the position

of the atom in the layer [42]. A detailed study of this phenomenon has not been performed in this thesis. Atoms on top of Cu_2N are measured with a setting current of at least 200 pA and a setting bias being equal to the starting point of the spectroscopy. The modulation bias V_m is 240 μV in all the cases.

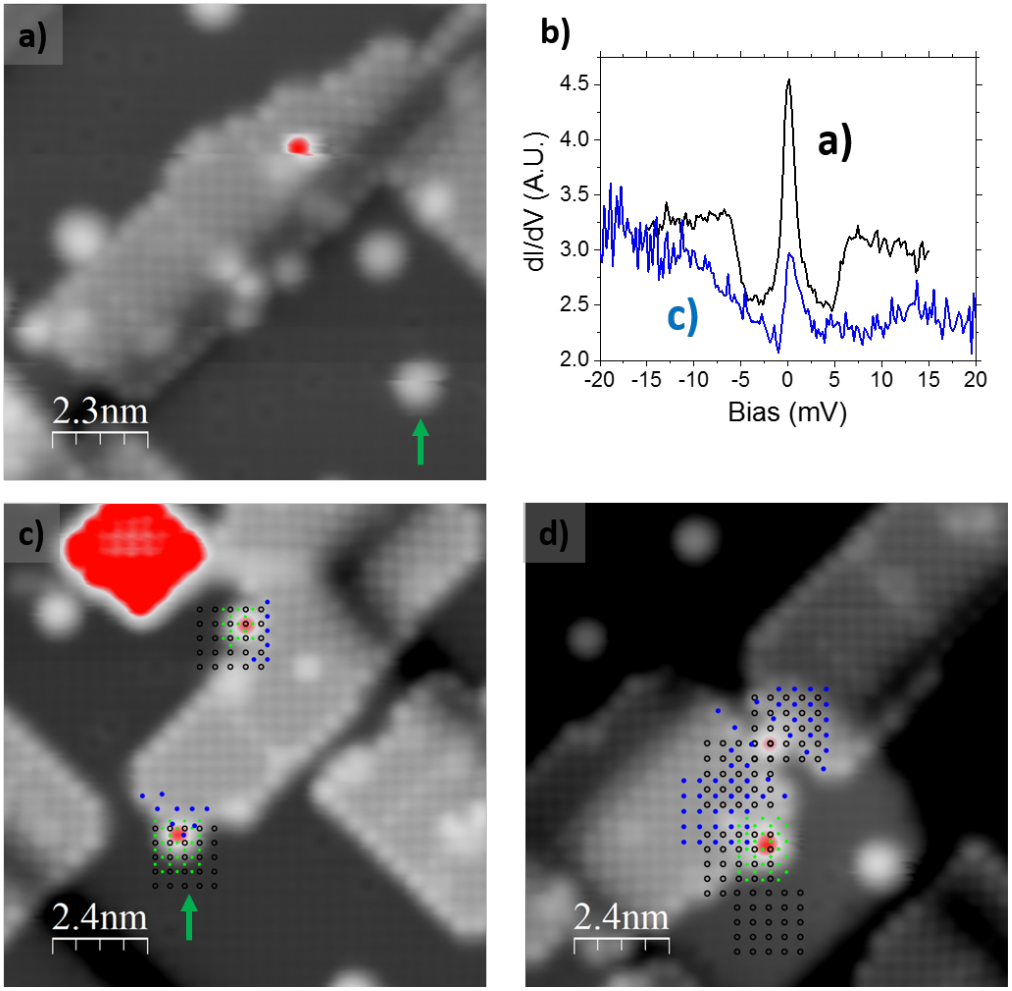

Figure 5.3: Positions of Co atoms on Cu_2N close to NaCl-ML/Cu_2N. Hollow black dots correspond to N atoms, green dots to Cu atoms, blue dots to Cl atoms. Na atoms are not sketched for simplicity. a) Co atom close to NaCl-ML/Cu_2N/Cu(001) (green arrow points to the measured atom). b) dI/dV with inelastic excitation of previous atom (black) and atom measured on panel c) (blue). c,d) Atoms on different positions close to NaCl-ML/Cu_2N/Cu(001) with atomically resolved binding sites. (V_{set}=-1.3 V, I_{set}=10 pA). In this color scale, black represents the lowest measured height, white intermediate and red is used to the highest measured height. This color scale is used in order to emphasize the atoms which in this system are observed with a very low corrugation.

With a sharp tip, it is possible to resolve atomically the lattice of Cu_2N and NaCl-ML/Cu_2N at the same time, which allows us to determine the adsorption sites of Co atoms and associate it with its characteristic spectroscopic signature. Figure 5.3

shows Co atoms on Cu_2N next to NaCl-ML/Cu_2N/Cu(001); their adsorption sites have been determined with atomic precision and characterized spectroscopically. It is important to remark that lattice distortion of NaCl on the 45° border makes difficult the characterization of the adsorption site. Previous work has shown two preferential adsorption sites for Co atoms on Cu_2N [107]: on top of Cu and N sites. Among them, only Co adsorbed on Cu sites reveal spin flip inelastic steps arising from MAE. It is important to remark that the data in this section are preliminary results; with a combination of analysis of apparent heights, comparison of the lattice site assignment, and atomic manipulation it will be possible to determine unambiguously that the Co atoms are in fact in Cu_2N lattice sites. These are promising results, showing a strong modification of the mangetocrystalline anisotropy as well as the total spin ground state of the Co atom (see below).

The impact of the atomic environment on the magnetocrystaline anisotropy is neatly illustrated by Figure 5.3, where a Co atom is placed close but not aside NaCl-ML/Cu_2N/Cu(001) sitting on a Cu site. This atom does not show appreciable modification of its inelastic excitation compared to the case of bare Cu_2N. Only the lower atom in figure 5.3c shows evidence of a spin-flip excitation in the tunnel current and surprisingly, the atom has been determined to sit on top of hollow site of Cu_2N lattice. Atoms in figs. 5.3b and c, as well as fig. 5.4a and b are clearly in a characteristic site: the very edge of the NaCl-ML island, on top of a Cu_2N hollow and in between two Cl atoms (i.e., occupying presumably the position of a Na atom if the NaCl-ML layer was continued). They have the same appearance, but different spectra, because they are at different edges: straight, acute corners and obliques corners. Figure 5.4f, which happens to sit on Cu_2N, shows spectra non-characteristic of a Co atom on Cu_2N. It does not show Kondo excitation for small anisotropy while previous work reported that Kondo excitation disappears for large anisotropy [42], so it is influenced by the NaCl.

Low energy spectroscopy of adsorbed Co atoms aside NaCl-ML show a wide variety of spin phenomena. Single transition and shifted Kondo resonance (Fig. 5.4a_1), what could be a Kondo antiresonance (Fig 5.4b_1, multiple spin transitions (Fig. 5.4c_1, d_1) and other features can be found on these atoms (Fig. 5.4e_1,f_1).

In this section we have seen how low energy magnetic excitations can be modified

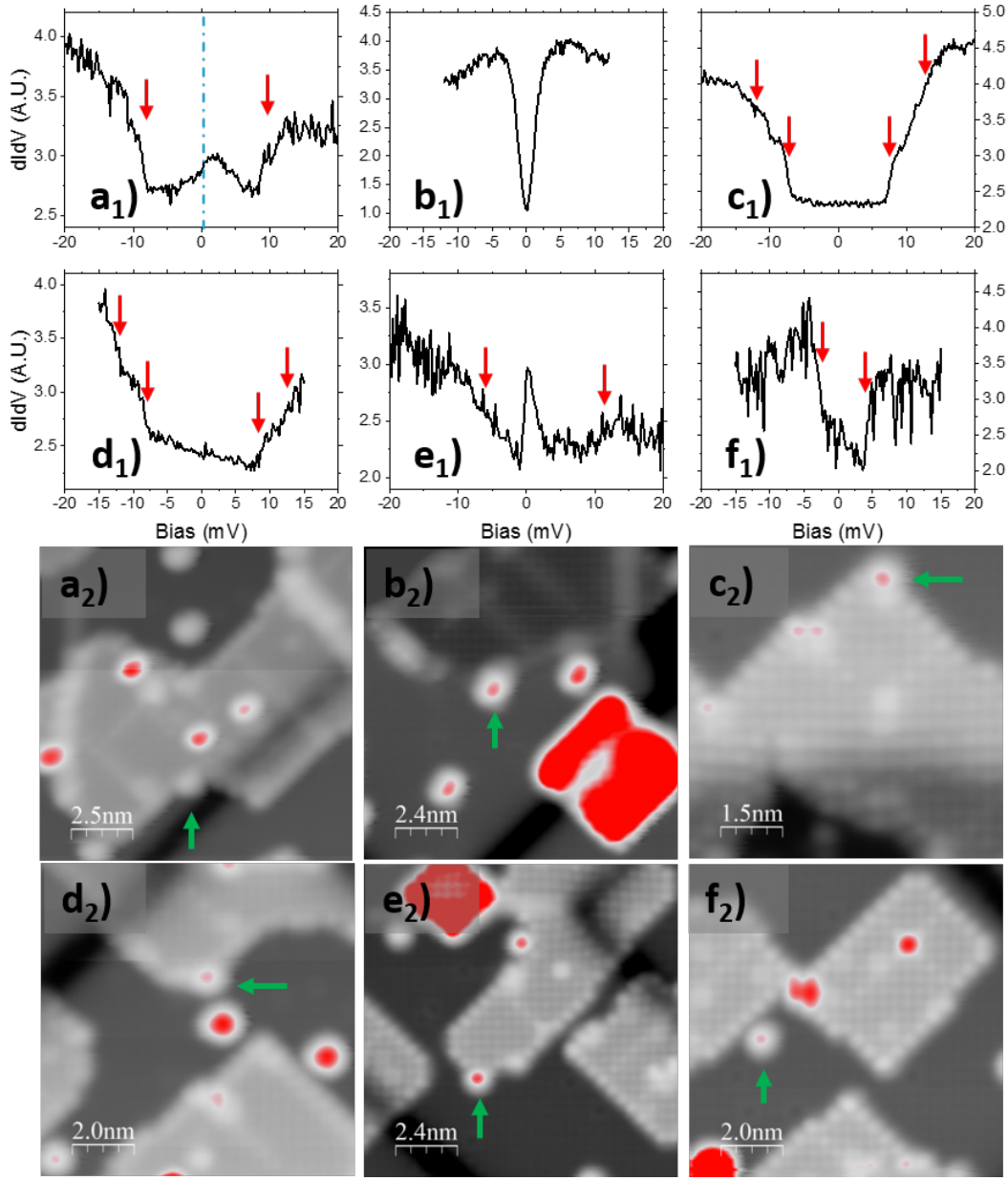

Figure 5.4: Determination of the spin excitation of Co/Cu_2N atoms in the vicinity of NaCl-ML/Cu_2N/Cu(001) and their positions close to NaCl-ML/Cu_2N/Cu(001). Red arrows denote the energy of possible IETS excitations. Green arrows denote the measured atoms. a_1) Shifted Kondo resonance feature. b_1) Kondo antiresonance excitation. c_1) Inelastic feature with with two possible spin transitions. d_1) Inelastic spectrum with two possible spin transitions. e_1) Inelastic spectroscopy with Kondo resonance and a broad spin transition. f_1) Spectrum with a single transition.

when a Co atom is placed next to NaCl-ML because the local environment is modified. Although these results need further confirmation - a strong proof would be atomic manipulation of Co atoms in the surroundings of NaCl-ML – they are rather

promising. Not only the modification of MAE is observed, but the possible appearance of new transitions (more than one step) that actually are forbidden for Co atoms on bare Cu_2N. This fact suggests a possible change occurring in the electronic structure of the Co atom. A half integer spin less or equal than 3/2 cannot have more than one energy gap at zero field. Therefore, the S value must have changed if more than one step is observed.

5.4 Co Atoms on Top of NaCl/Cu_2N/Cu: Influence of Adsorption Sites and Local Environment

It has been demonstrated that placing Co atoms near to NaCl-ML modifies dramatically the magnetic ground state and then it is natural to think that, in the same way, spin excitation process will be altered when they are placed on top of NaCl/Cu_2N/Cu(001).

The insulating nature of this heterostructure (NaCl/Cu_2N) on Cu results in a decrease of the tip-atom distance, making the measurement of Co atoms on top of NaCl even more challenging. In many cases the atoms are swept away due to the perturbation caused by the tip when scanning over the sample. In addition, measuring at too large tip-sample distances makes detection of the inelastic signal difficult, due to too low currents.

Apparently, in the square lattice of NaCl-ML/Cu_2N/Cu(001) four adsorption sites should be available; Co on top of Na, on top of Cl, on the bridge site, and on the hollow site. However, as it will be shown, the apparent lack of hybridization of the atoms in this system, the presence of defects in the layer and the “amorphous" features frequently found make the adsorption site hard to resolve.

In this section, different adsorption sites of Co on top of NaCl-ML/Cu_2N/Cu(001) are identified with the help of atomic manipulation. In addition, a modification of the NaCl-ML/Cu_2N/Cu(001) structure is observed associated to the presence of Co atoms.

Some of the Co atoms on NaCl-ML/Cu_2N/Cu(001) can be identified thanks to their spectroscopic signature: an inelastic process. Hence, performing spectroscopy on a *bright feature* (i.e. a topographic protrusion) which contains an inelastic process

allows us to identify it as an adsorbed Co atom. Once measured, the Co atom can be moved to another position, since it is very easy to make the atom jump with the perturbation of the the tip. The atom will then change its position (tipically to Na site), allowing us to conclude that the new small feature is in fact the same atom previously measured. Figure 5.5a shows a Co atom on NaCl-ML/Cu_2N/Cu(001) (indicated with the green arrow) with a characteristic inelastic step (Fig. 5.5b). After this measurement the atom is moved, jumping to a well identified binding site. Figure

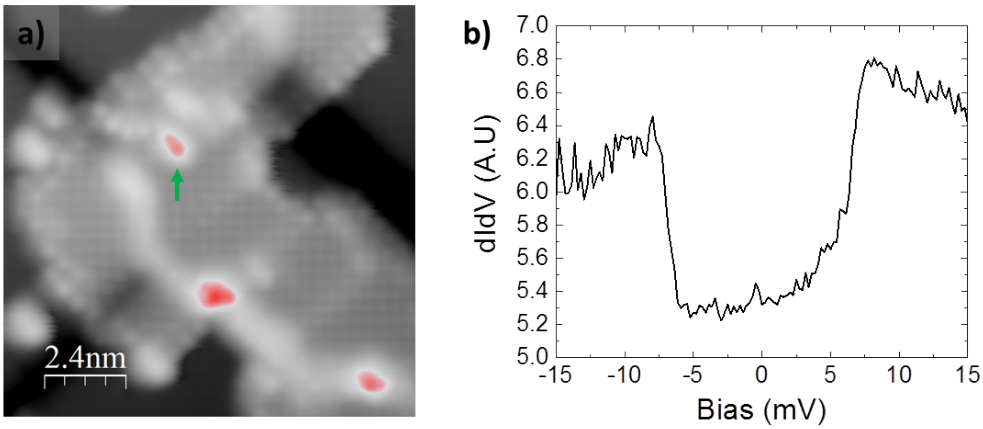

Figure 5.5: Co atom on an unidentified binding site of NaCl-ML/Cu_2N. a) Position of the bright atom pointed with a green arrow. b) Spectroscopy signature of the atom measured with V_{set}=-50 mV, I_{set}=200 pA.

5.6 shows the new binding site of the Co atom after the jump. By sketching the NaCl lattice on top, is easy to conclude that the atom is sitting now on top of a Na atom. Actually, this square-shape protrusion has been identified as the signature of a Co atom atop a Na site.

Co atoms on top of Na sites can be laterally manipulated to the next Na atomic position by approaching the tip on closed feedback and decreasing bias. Starting bias of V_{set}=-1.3 V, I_{set}=10 pA and decreasing the bias until a jump in z control is observed, tipically in the order of tens of mV. The tip is moved through the NaCl-ML/Cu_2N/Cu(001) island while the atom follows the tip. The speed of the tip during lateral manipulation is set in the order of a few nm/s. By this method, the Co manipulation proceeds preferentially through Na binding sites (Fig. 5.7a,b,c). One consequence of the atomic manipulation is the perturbation of the structure. Bright Cl rows pointed with green arrows change jointly with the atom displacement towards

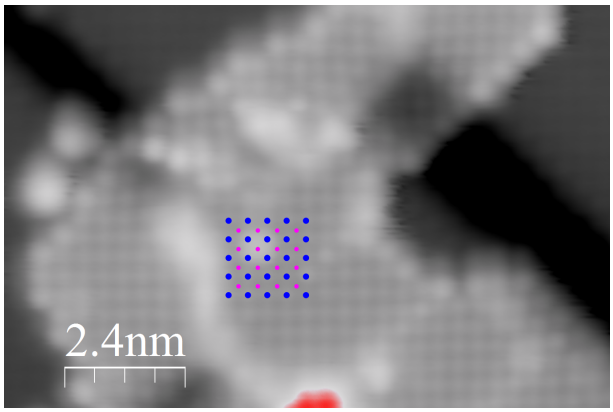

Figure 5.6: Co atom in its new binding site. Blue dots correspond to Cl atoms while magenta dots correspond to Na atoms. The center of the atom is placed right on top of an Na site, V_{set}=-1.3 V, I_{set}=10 pA.

the right side.

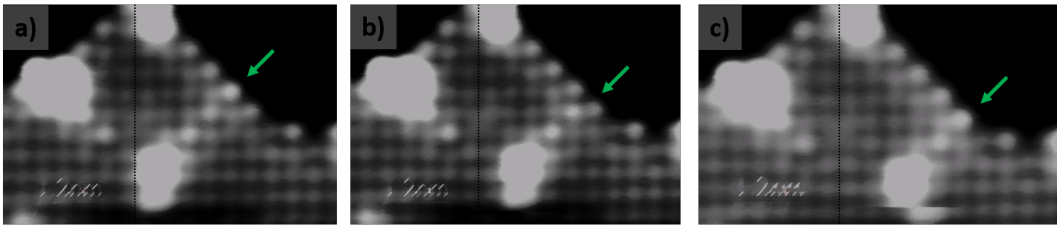

Figure 5.7: Sequence of the manipulation of Co atom on top of Na binding site. Dark dotted line placed on Na row for comparison. Green arrows point out the displacement of the bright Cl row of NaCl-ML/Cu_2N/Cu(001).

The manipulation to well defined adsorption sites and the prior characterization of the inelastic signal will be our criteria to make sure that the irregular features are in fact atoms placed on defects of the NaCl-ML/Cu_2N/Cu(001) layer. Defects on NaCl/Cu_2N/Cu(001) (Fig 5.8) have the same appearance than those created on NaCl on different metallic substrates which have been identified as Cl vacancies [94, 108]. Contrary to NaCl on metallic substrates, defects on NaCl/Cu_2N/Cu(001) can be found over the islands without the need to create them. The concentration of vacancies decreases with the size of the Cu_2N patches. Small patches contain larger number of vacancies than large patches. This effect could be associated to the surface dipole compensation. With an extended layer of Cu_2N it is possible that the NaCl surface becomes reconstructed to reduce its net polarization at the surface while the only possibility for NaCl to reduce the induced polarization in small Cu_2N patches might be the creation of defects, spotted as Cl vacancies [79, 80].

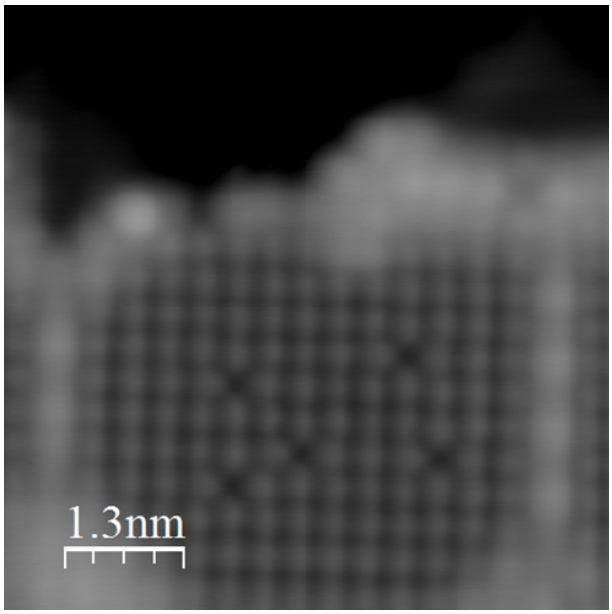

Figure 5.8: Typical defects on NaCl-ML/Cu_2N/Cu(001)when NaCl is grown on grid Cu_2N (V_{set}=-1.3 V, I_{set}=50 pA).

Figure 5.9 shows two different Co atoms placed very near to vacancies. In figure 5.9a, thanks to the sharpness of the tip, it is still possible to observe the shape of the vacancy; the confirmation of the presence of the Co atom is proven with the help of the spectroscopy (Fig. 5.9b). In the second case, the bright feature (Fig. 5.9c) jumps onto a Na position, allowing the visualization of the defect; the feature and its movement is indicated with a green arrow; red arrow indicates the position of the vacancy. The atom, still irregular due to the presence of the vacancy (Fig. 5.9d), with the help of atomic manipulation, is dragged rightwards, recovering its characteristic Na binding site shape (Fig. 5.9e). Then it is again brought close to the vacancy. Here, it is remarkable how the Cl vacancy distorts the shape of the atom (Fig. 5.9f).

By manipulating the Co atom and placing it close to a 45° border it was possible to put it on top of a Cl site (Fig. 5.10a,b). As in the case of Co on Na site, Co atom on Cl site (Fig. 5.10c,d) can be manipulated to jump to other Cl sites, with a reconstruction “indicating" the position of the atom. The cross-shaped featured observed here is characteristic of a Co atom atop a Cl site. By dragging the atom to the center of the island, it jumps again to a Na site (Fig. 5.10e,f). In either case Co on top of Na or of Cl without nearby defects, spectroscopy reveals no spin excitation on either adsorption sites (Fig 5.11a,b).

After atomic manipulation and spectroscopy study it can be concluded that small

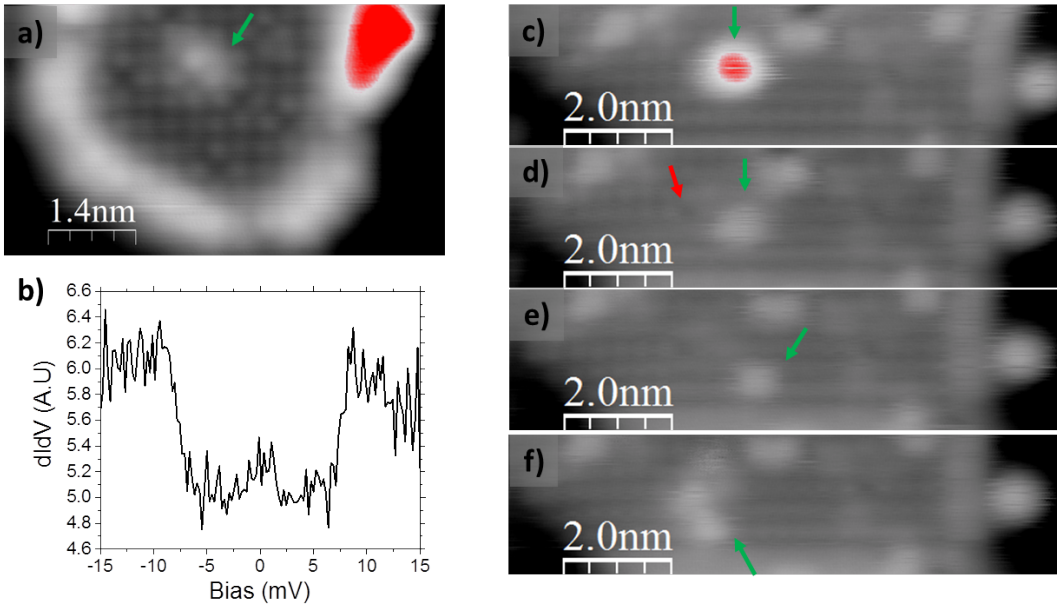

Figure 5.9: Influence of Cl vacancies on Co atoms. a) Co atom on top of a Cl vacancy, amorphous shape of the atom. b) Spectroscopic signature of the magnetic impurity showed on a). c) Co atom on top of a vacancy, bright feature. d) Co atom on a Na site close to the vacancy. Distortion of the feature. e) Co atom far from the vacancy. Recovery of the symmetric shape of the Co atom. f) Co atom brought back to the vacancy. Distortion of the shape, lack of symmetry in the feature. (Spectroscopy taken with (V_{set}=-50 mV, I_{set}=50 pA), images taken with (V_{set}=-1.3 V, I_{set}=10 pA).

features on Na sites are, in fact, Co atoms which do not show any spin excitation. Co atom on Na sites can be, so far, laterally manipulated through Na sites. It has been shown that it is also possible to force them to sit on top of a Cl site, revealing again no spin-flip. Amorphous features with spin excitation are in fact Co atoms placed somewhere around a Cl vacancy. In the proximity of a vacancy, the amorphous shape makes it difficult to identify the atom's binding site.

5.5 Multiferroicity at the Atomic Scale: Control of Spin Excitations with Electric Fields

The previous chapter has shown the possibility of reversing the surface dipole of the outer layer of NaCl-BL/Cu_2N/Cu(001) using the inverse piezoelectric effect. In addition, some early results on defects on NaCl-ML and NaCl-BL on Cu_2N/Cu(001) (see future work on previous chapter) have shown hysteretic behaviour of what it seems the same dipole reversal process. In other words, the defect pins both states causing

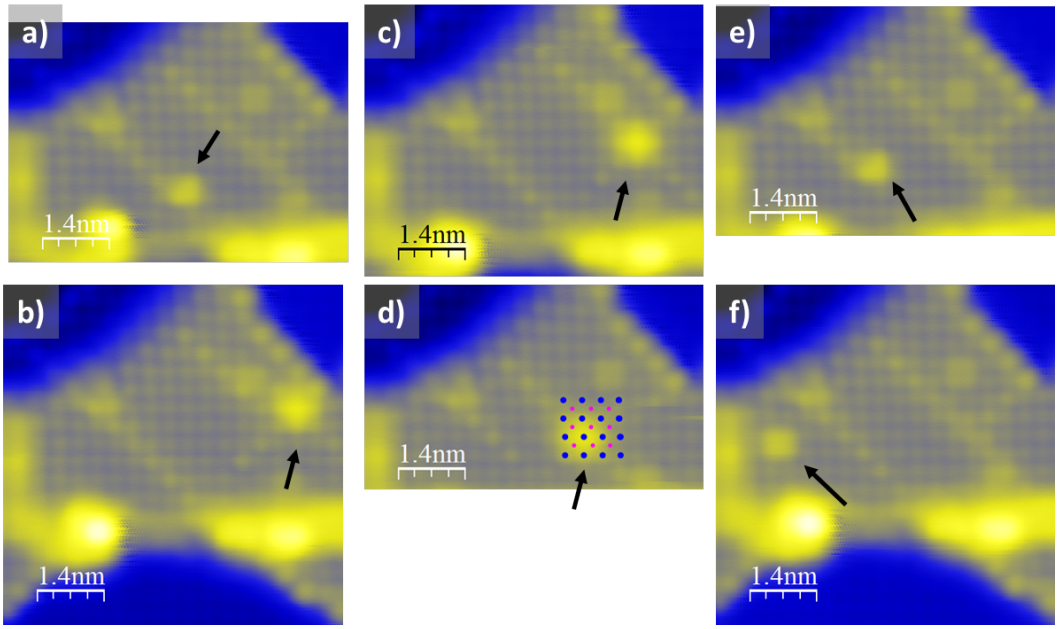

Figure 5.10: Sequential images of atomic manipulation. a) Co atom on a Na site. b) Atom brought to a 45° border, the atom jumps to a Cl site. c) Manipulation of the Co atom to the center of the island on a Cl site. d) Ball model (blue dots Cl atoms, magenta dots Na atoms, indicating the atom is centered on a Cl site. e) Atom back on a Na site. f) Co still on Na site after successive manipulations.

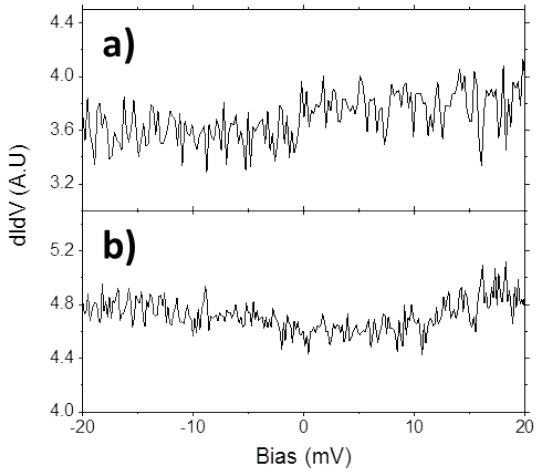

Figure 5.11: dI/dV measurement performed on Co atoms. a) dI/dV performed over a Co atom adsorbed on top of Cl site. b) dI/dV performed over a Co atom adsorbed on top of Na site.

in this way, two stable states at zero tip-sample external bias which are electric field induced: ferroelectricity. This chapter has shown that spin-flip processes have been only found in highly asymmetric adsorption sites, for example, in Co atoms placed on the border of NaCl-ML with Cu_2N or an unidentified binding site somewhere around a Cl vacancy.

Therefore, it is natural to think that the electric field induced states, that are the two different polarizations (which seems to be pinned by Cl vacancies) could affect the spin-flip process and be measured. A change in the underlying NaCl-ML structure could then affect the magnetism of the Co atom, achieving in this way multiferroic cycles at the atomic scale.

5.5.1 Description and Design of the Experiment

In a planar tunnel junction, the distance between the electrodes is fixed and then the behaviour of the tunnelling current is studied varying the bias. This way to proceed is not only applied for the wide variety of existing tunnel junctions (superconducting electrodes [109], ferroelectric barrier [86], ferromagnetic electrodes [110], etc.) but also for other methods to measure ferroelectric properties of thin layers. This is the case of conductive atomic force microscopy (C-AFM) [111], where the tip is in contact (and hence always at the same distance from the sample) and then the tunnelling current is measured as a function of the applied bias. Ferroelectric thin layers have also been studied with C-AFM. Two different regimes with high and low resistivity are observed coinciding with the switching of the ferroelectric domains [88, 112, 111].

However, the nature of these measurements by means of STM presents additional degrees of freedom beyond the contacting force and the applied bias. A detailed description of the tip-sample regulation process and the experiment followed with STM is crucial to understand and follow how measurements of a ferroelectric cycle can be performed with an STM. In closed feedback mode, the current is regulated with tip-sample distance. A change in the current will result in a change on the tip-sample distance. In the same way, in order to keep the same current a change in the bias will result in a change on the tip-sample distance. Therefore, this will result in an applied electric field determined by the feedback and the regulation set point. Figure 5.12 shows how ideally a ferroelectric cycle with a magnetic read out is performed in this system. The sample is scanned at negative bias (normally V_{set}=-1.3 V, I_{set}=10 pA). The tip is positioned on top of the adsorbed Co atom close to the Cl vacancy. The feedback loop is turned off. The bias is decreased until Point 1 is reached. Then dI/dV is performed at low bias in order to measure the inelastic

spin-flip signal (Measurement on State A). The bias is ramped to positive values until switching to “State B" is achieved. Then the bias is ramped down to the same bias where the inelastic spectroscopy seeking for spin-flip processes starts typically (Point 2). At this point, another high resolution dI/dV curve is acquired to characterize the inelastic spin-flip spectrum corresponding to state B. Finally, the bias is ramped to more negative bias until "State A" is reached again and the cycle is closed.

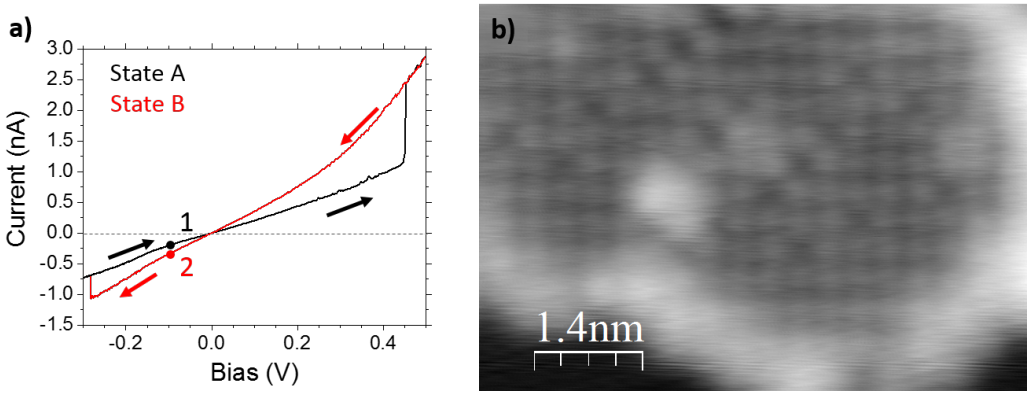

Figure 5.12: Ferroelectric cycle on a Co atom on top of a vacancy in NaCl-ML/Cu_2N. a) Black and red curves indicate indicates the state A and B while the points labelled with number indicate the bias where the low bias spectroscopy was performed (V_{set}=-0.3 V, I_{set}=750 pA). b) Topographic image with a red mark showing where the spectroscopy was taken (V_{set}=-1.3 V, I_{set}=10 pA)

Since it is an electric field driven process, the bias at which the transition occurs will vary from tip to tip (since the electric field depends on the precise shape of the tip apex, which changes with different tips). Moreover, it will be necessary to have a high enough input lock-in signal to detect the inelastic dI/dV spectra. This means that the tunnelling current will have to be undoubtedly increased (by decreasing the tip-sample distance). For this purpose it is completely essential to monitor every step made with STM not only to perform the ferroelectric cycle without missing any possible switch or transition but also to measure the inelastic dI/dV spectum in both states. Fig 5.13 details the process to perform a successful cycle without missing any information. The bias is decreased in closed feedback mode in order to reduce the tip-sample distance. The z-piezo is monitored; a switch or change in the layer would have been seen as a sharp increase or drop of the tip height (Fig. 5.13a). Immediately, still in closed feedback conditions, the current is increased from 10 to 200 pA which is essential to have enough lock-in input signal (Fig. 5.13b). This closer tip-sample distance also allows us to apply electric fields above the coercive fields of the material

with moderate sample bias. Low bias spectroscopy is performed to track down the spin-flip events (Curve 1 of Fig. 5.13d). The tip is kept at a constant height and the bias is ramped to positive values until a sharp change in the current is observed. Then the bias is ramped to small negative values in order to measure the effect of the new polarization state of the substrate in the spin-flip processes (Fig. 5.13c). After measuring the variation on the inelastic signal (Curve 2 of Fig. 5.13d), the bias is ramped to more negative values in order to close the cycle. To guarantee that the process is reversible, we return to small negative bias reaching again point 1, and then confirm that the corresponding inelastic spectra is reproduced.

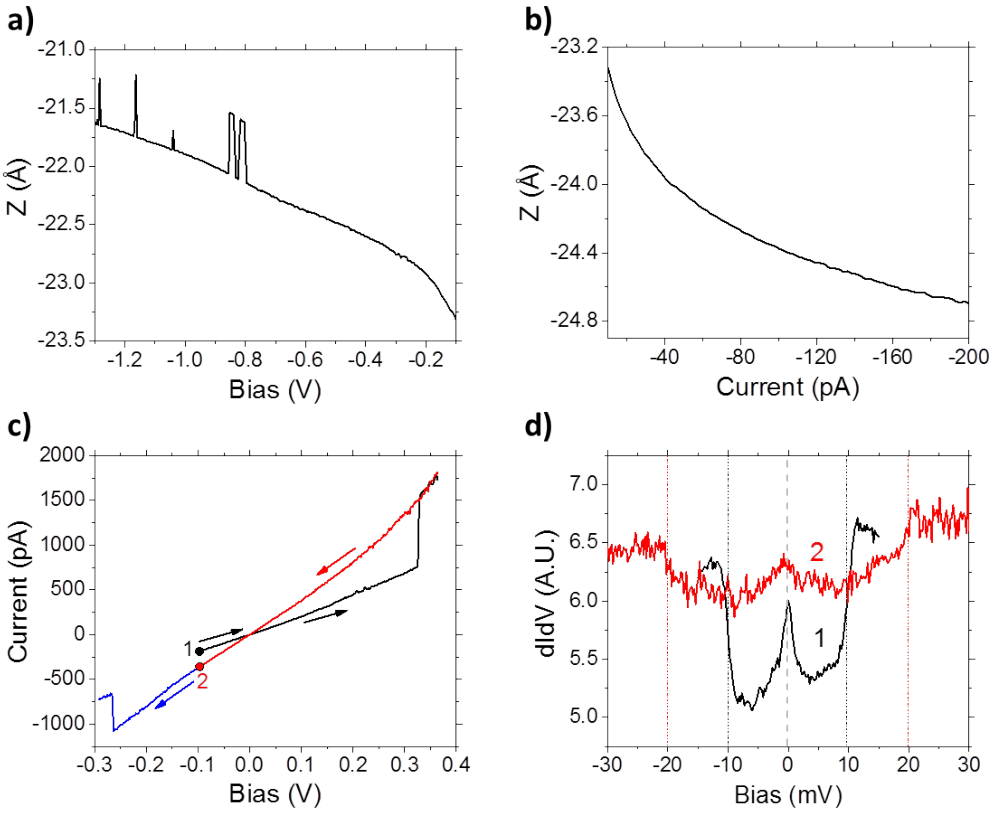

Figure 5.13: Multiferroic cycle. a) Closed feedback bias decrease from -1.3 V to -100 mV. b) Closed feedback current increase from 10 pA to 200 pA. c) Ferroelectric cycles indicating the points where the spectroscopy was performed. d) Inelastic spin-flip spectroscopy measured before, after the transition and in state 1 again.

Three different parameters govern these multiferroic cycles on STM: tip height, applied bias and current. The graphs presented on Fig. 5.13 can be summarized on a 3D plot where the three parameters are considered. In this way, Fig. 5.14 will help us to represent the entire cycle performed as well as all the tip-sample interactions occurring within one single figure without losing any information. In Fig. 5.13d we

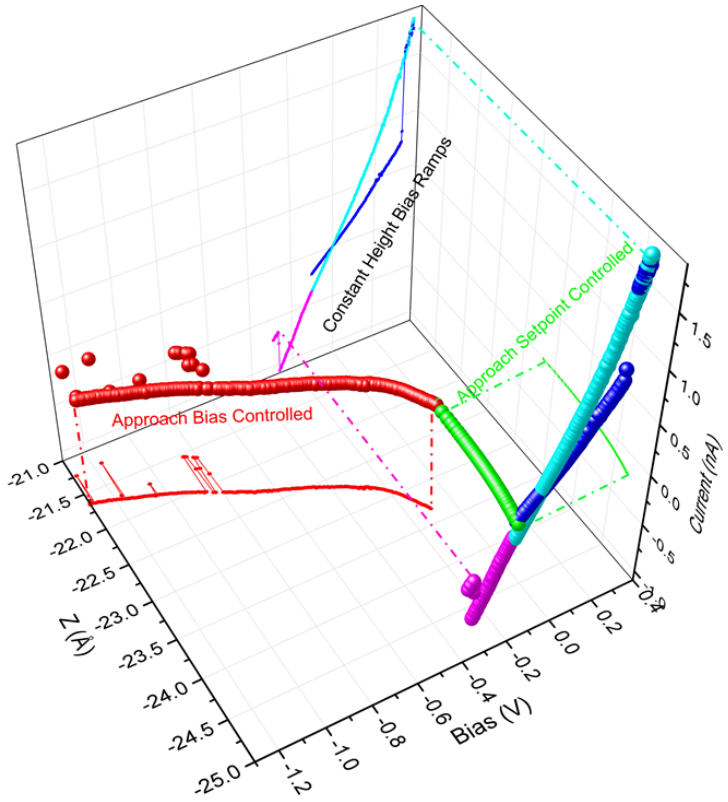

Figure 5.14: 3D plot of a ferroelectric cycle including tip-sample distance. In each axis is represented one of the three different parameters that represents the degree of freedom of a tip-sample system: absolute piezo distance, applied bias and tunnelling current. Each colored curve represents a variation of one parameter as a function of other keeping the third one constant and projected on its respective plane.

observe a dramatic change in the magnetic anisotropy which goes from 9.7 meV for point 1 to between 15 and 20 meV for point 2 implying multiferroicity at the atomic scale. The structural change on NaCl-ML/Cu_2N/Cu(001) affects the magnetism of the atom: the magnetic anisotropy changes by a factor of 2 and the zero bias peak ascribed to Kondo screening displays a prominent broadening. It is remarkable the appearance of a Kondo peak for a magnetic impurity separated by two insulating layers from the screening electrons in the metal.

Once this effect is observed and described, it is essential to perform further experiments to confirm the ferroelectric nature of the magnetic anisotropy change. Thus, it is fundamental to discard charging effects (demonstrating the electric field dependence of the transition), reproducibility (going several times from A to B and measuring the magnetic anisotropy change), magnetic nature of the inelastic process (with the help of applied magnetic fields) and finally, reproducibility with other magnetic

impurities.

5.5.2 Multiferroic Cycles

Unfortunately, due to the complexity of the system, multiferroic (MF) cycles have been observed on only four different locations. On the one hand it is important to have a robust tip capable to scan in these conditions, very close to the sample, without perturbing the adsorbed atoms (which are even closer to the tip). It is also important to perform spectroscopy without having significant contributions from the tip LDOS. This can be checked by performing low bias spectroscopy over a surface without atoms or defects and seeing that it is, in fact, flat. The tip must be able to withstand high electric fields (to perform the ferroelectric cycles) without leaving any material in the substrate and without blowing away the atom and finally, in some cases, able to stand large current over the insulating heterostructure. For all these reasons, the experiment with atoms becomes laborious.

5.5.3 General Overview

So far, the measurements performed on this system showed two switchable states that are bias controlled, however ferroelectric cycles previously shown were not completely tracked. It is worth mentioning that not only a change in MAE was observed, but also in the shape of the Kondo peak, including even its total suppression. Figure 5.15a,b shows topographic images of state A and B after bias ramp in another atom. As observed, the atom does not change its atomic position, but there is an evident decrease in the density of states. Figures 5.15c,d show the associated dI/dV inelastic spectra for each states.

In four cases it has been possible to ramp the bias, switch reproducibly between states A and B, and measure the change in the anisotropy without destroying the area or the tip. In this way, with the previously designed experiment (Fig. 5.14), multiferroic cycle probed in a single atom has been achieved, measuring the variation in both states of the magnetic anisotropy.

Fig 5.16 shows the four different cases found. In all the cases there is a substantial change in the magnetic anisotropy but apparently no change in the total spin, which could lead, for example, to a variation of the number of steps observed. This points to the idea of magnetoelectric coupling mediated by a change in the lattice constant

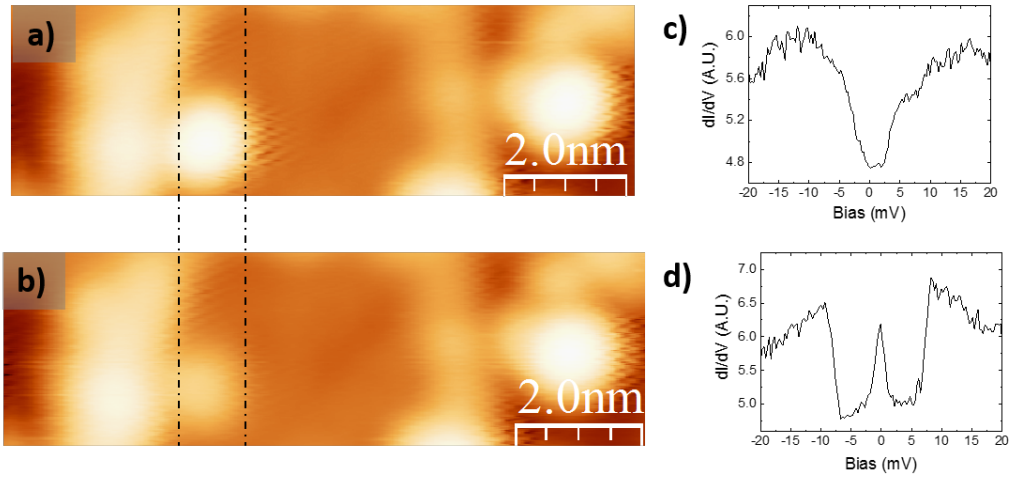

Figure 5.15: Imaging two possible A and B states in the ferroelectric cycle. a) Topographic image of the atom in the initial state A. b) Topographic image of the atom after switching to state B (I_{set}=50 pA, V_{set}=1 V). c) dI/dV inelastic spectroscopy taken in the state A. No Kondo excitation is observed in this case. d) dI/dV inelastic spectroscopy taken in the state B. A Kondo peak appears at Fermi level and the zero field anisotropy splitting experiences a drastic variation (I_{set}=100 pA, V_{set}=30 mV).

(electric polarization), which leads to a change in the magnetic anisotropy rather than an atom charging process. In three of the cases (Fig. 5.16a,c,d) the magnetic anisotropy increases after switching to state B.

As explained before, the cycles exhibit sharp changes in current due to the change in the electric polarization and consequently in the tunnelling barrier. Figure 5.17 shows the I(V) cycles of the previous inelastic excitations showed. Although figure 5.17a does not show a canonical cycle, meaning that there is more than one current abrupt change per ramp, the rest of the cycles (Fig. 5.17b,c,d) match the expected behavior. These cycles have been repeated sequentially switching from A to B several times, indicating the reproducibility of the performed measurements.

The previous discussion suggests that these ferroelectric cycles as well as the spin-flip process might be related to the presence of neighbouring vacancies. For this reason it is essential to know the adsorption site of Co atoms. Fig. 5.18 shows with atomic resolution the adsorption site of the Co atoms as well as the surrounding environment of the atom corresponding to the previously discussed spectra (Fig. 5.16,5.17). It is possible to determine the presence of vacancies on at least three cases (Fig. 5.18b,c,d), while no vacancies are observed (Fig. 5.18a) when the atom

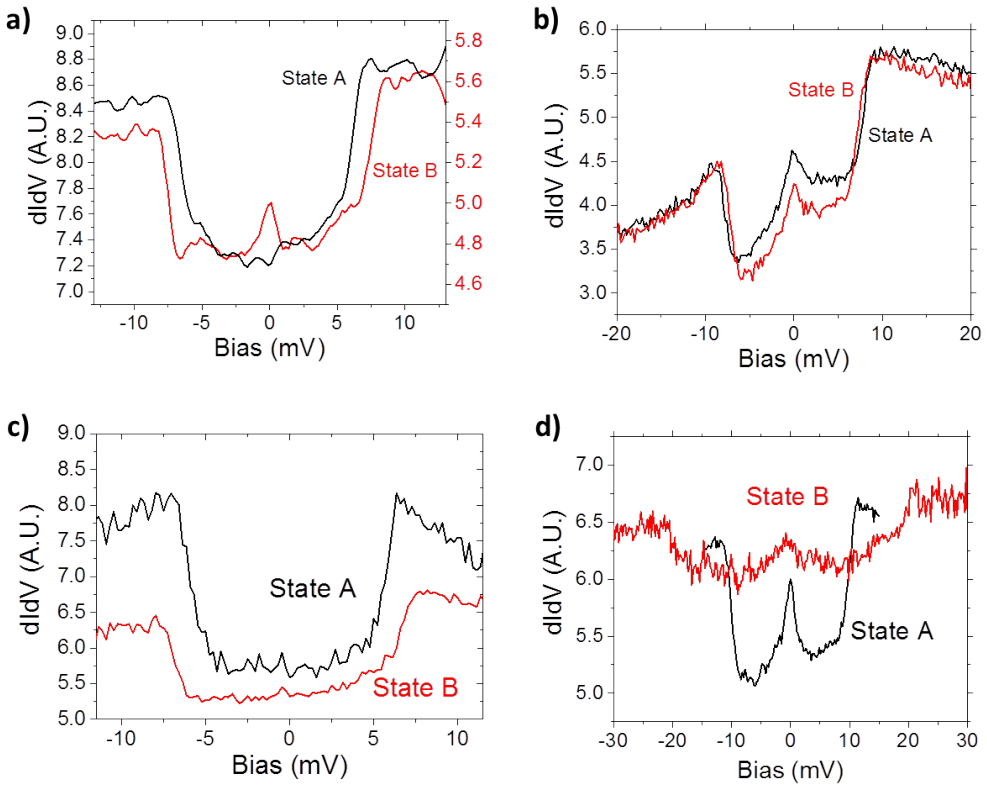

Figure 5.16: Inelastic dI/dV spectra observed on *State A* and *State B*. Panels a), c) and d) show an increase of the MAE while panel b) shows a decreased I_{set}=200 pA, V_{set}=-50 mV.

is in the border of NaCl-ML (marked as brown circle), which could be considered as a defect itself. Figure 5.18b shows a faint depression associated to a Cl vacancy on top of which the atom is sitting. Figure 5.18c shows the Co atom with inelastic spectroscopy signal (upper image) and after jumping to a Na site (bottom image), showing the previous adsorption site (pointed with a red arrow). This shows that it was next to at least one Cl vacancy. Figure 5.18d shows two surrounding vacancies with the help of a sketched lattice. Therefore, atomic resolution shows an unambiguous link between defects on NaCl-ML/Cu_2N/Cu, and bistable multiferroic coupling of the magnetic and structural adsorption states of Co atoms.

Having confirmed this point, it is mandatory to confirm the ferroelectric nature of the process (by proving that it is an electric field driven process) and the magnetic nature of the inelastic excitations (with applied magnetic fields). It would be also interesting to investigate the behaviour of the inelastic step with applied fields before and after the switching.

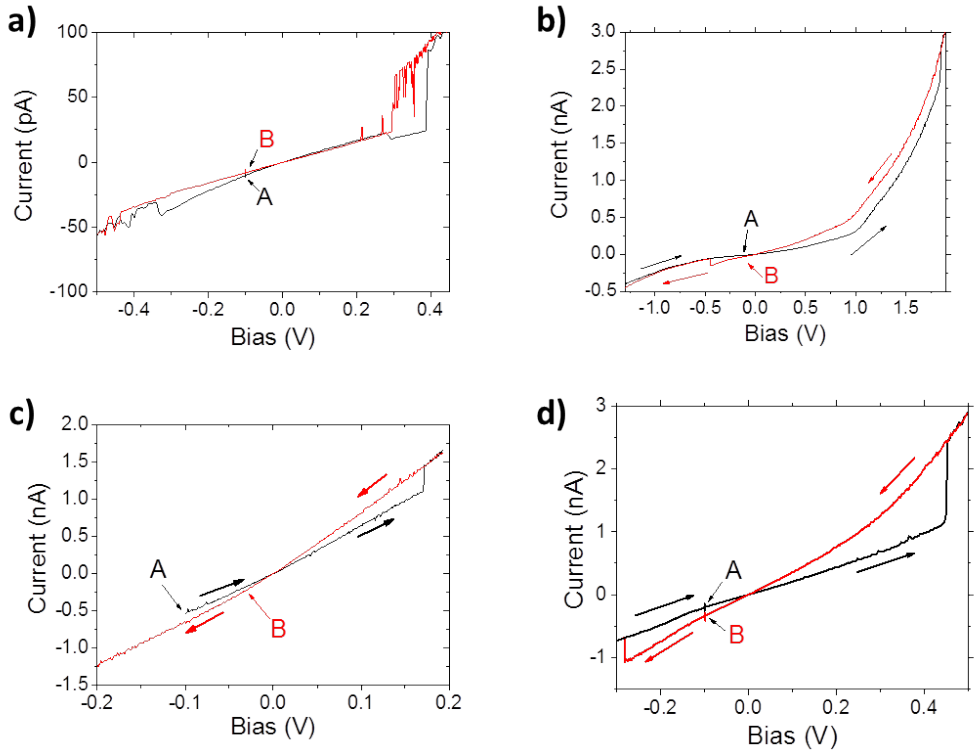

Figure 5.17: Ferroelectric cycles of previous inelastic excitation measurements. a) This cycle is special and currently not well understood since multiple jumps in current are detected, indicating that maybe one than more process is going on. b,c,d) Canonical ferroelectric cycles measured with the change on I(V) current. For all the cycles the initial setting current is the one with the lowest negative bias on state A showed on the graphs as it is the initial setting bias.

5.5.4 Electric Field Dependence

In the previous section, the electric field induced nature of the process has been confirmed setting the initial tip-sample distance, varying the applied bias and retracting the tip. In this case, since we are performing I(V) curves instead of I(Z), the way to confirm it is varying the tip-sample distance systematically. Due to the small tip-sample distances arising from tunneling through the insulating layer, it is recommendable to vary the setting current with the feedback loop closed rather than opening the feedback loop and adjusting the tip-sample distance directly. Since the electric field roughly goes as $E = V/Z$ (where in our system V is the applied bias between electrodes and Z is the absolute tip-sample distance) and variations in the setting current implies small variations of the absolute tip-sample distance (exponential behaviour of the current with distance), sequential variations in the setting current of one order of magnitude are required.

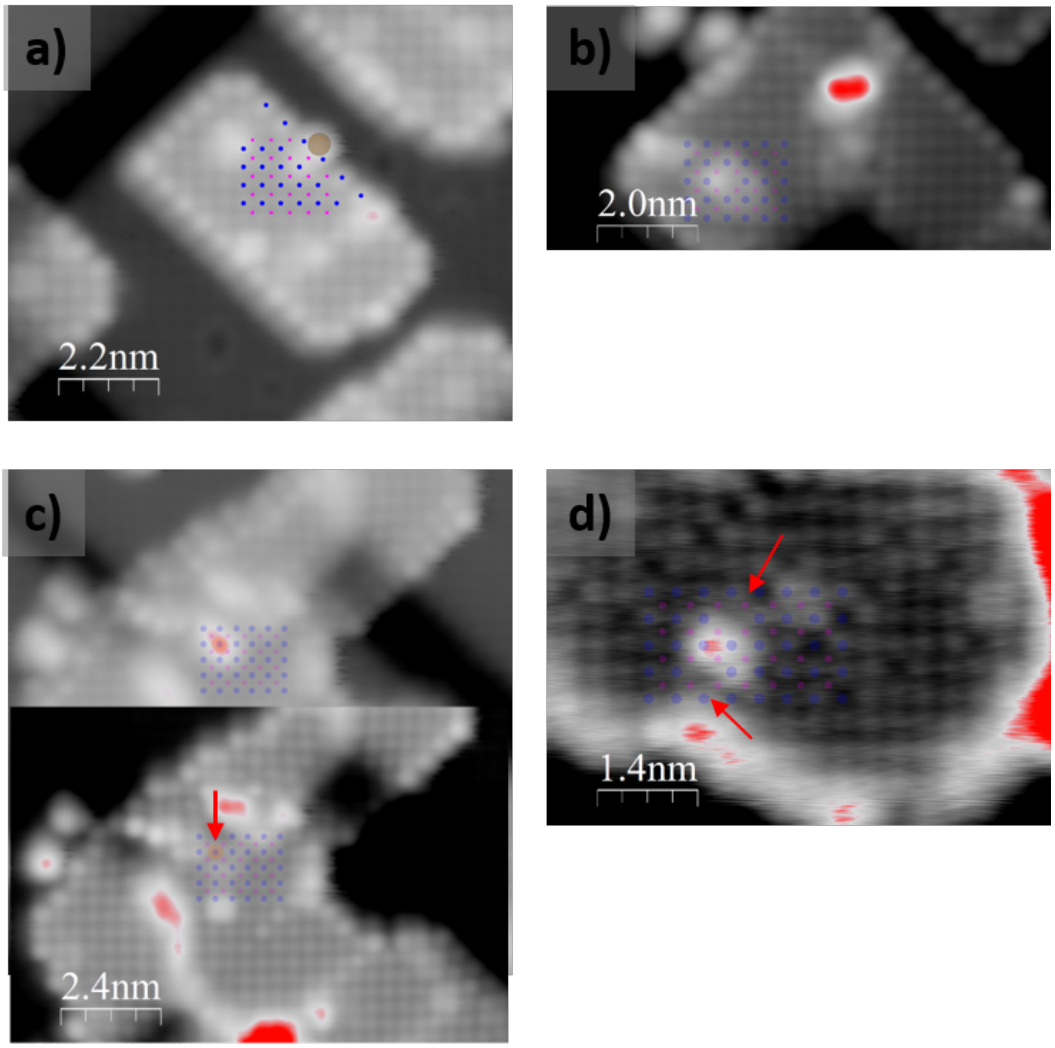

Figure 5.18: Adsorption sites of the four spectra with inelastic excitations and electric field induced transitions discussed in Figs. 5.16 and 5.17. a) Co atom located on the edge of NaCl-ML/Cu_2N/Cu(001). b) Co atom (blurry bright feature) located on top of a vacancy marked with a missing blue dot in the sketched lattice. c) Co atom on top of a Cl site (upper image) and after jumping to a Na site (lower image). The lower image also shows defects where right underneath the previous atom's position. d) Co atom on an not well defined adsorption site that could correspond to a bridge site. The Co atom is very close to Cl vacancies which are marked with missing blue dots in the sketched lattice, red arrows point to them. V_{set}=-1.3 V, I_{set}=10 pA.

Electric field-induced switching has been confirmed in two different cases (Fig. 5.19a,d), corresponding to the atoms a and d respectively of the previous discussed figures. In the first case, the bias at which the the transition is induced is not clear (Fig. 5.19a) while in the second case there is only a single sharp drop (Fig. 5.19d).

Second panel row indicates the switching bias (coercive field) as a function of the setting current. Since the current goes exponential with distance it does not follow a linear trend (Fig. 5.19). For each setting current, the position of the z piezo is recorded. Figure 5.19, third row, shows the coercive bias as function of the tip-sample distance relative to the value corresponding to the lowest setting current. The linear dependence is the mark of an electric field driven transition. Moreover fitting the trend with a linear fit should give us an idea of the critical electric field at which the transition is occurring.

For the atom depicted in Fig. 5.19a, the inferred critical electric field is 0.46 V/Åfor the forward and -0.32 V/Åfor the backward. In the second case it is only 0.06 and -0.07 V/Å, which is almost an order of magnitude lower. In both cases, the critical electric field is lower than in defectless NaCl-BL/Cu_2N/Cu(001), pointing to an easier switching between states in the presence of defects even in the case of NaCl-ML/Cu_2N/Cu(001).

5.5.5 Magnetic Field Dependence

To further confirm the magnetic nature of the inelastic process, magnetic fields were applied in some cases. It is hypothesized that the transition from state A to B is purely a change in the structure of the NaCl layer (inversion of the surface dipoles) which affects the magnetic anisotropy. Applying magnetic fields and seeing how the Kondo resonance and inelastic step changes in state A an B is particularly interesting to see how this structural change is affecting the magnetic anisotropy. In two different atoms it was possible to measure state A and B in the presence of an applied magnetic field.

Figure 5.20 shows inelastic processes measured over two atoms at 0 and 3 T on state A and B corresponding to the atoms a) and d) of the figures from section 5.5.3. As it can be seen, State A shows in both cases a shift of the inelastic step (Fig. 5.20a,c) of 0.0.08 meV/T and 0.13 meV/T for atoms a and d respectively. In the same way Kondo excitations are split with different values of 0.72 meV/T (Fig. 5.20a) and 0.56 meV/T (Fig. 5.20)c). Regarding state B, it remains unclear if there is a real shift of the steps since it is on the resolution limit of the microscope. However the split of the Kondo excitation can be measured, which results in a splitting of 0.65 and 0.9

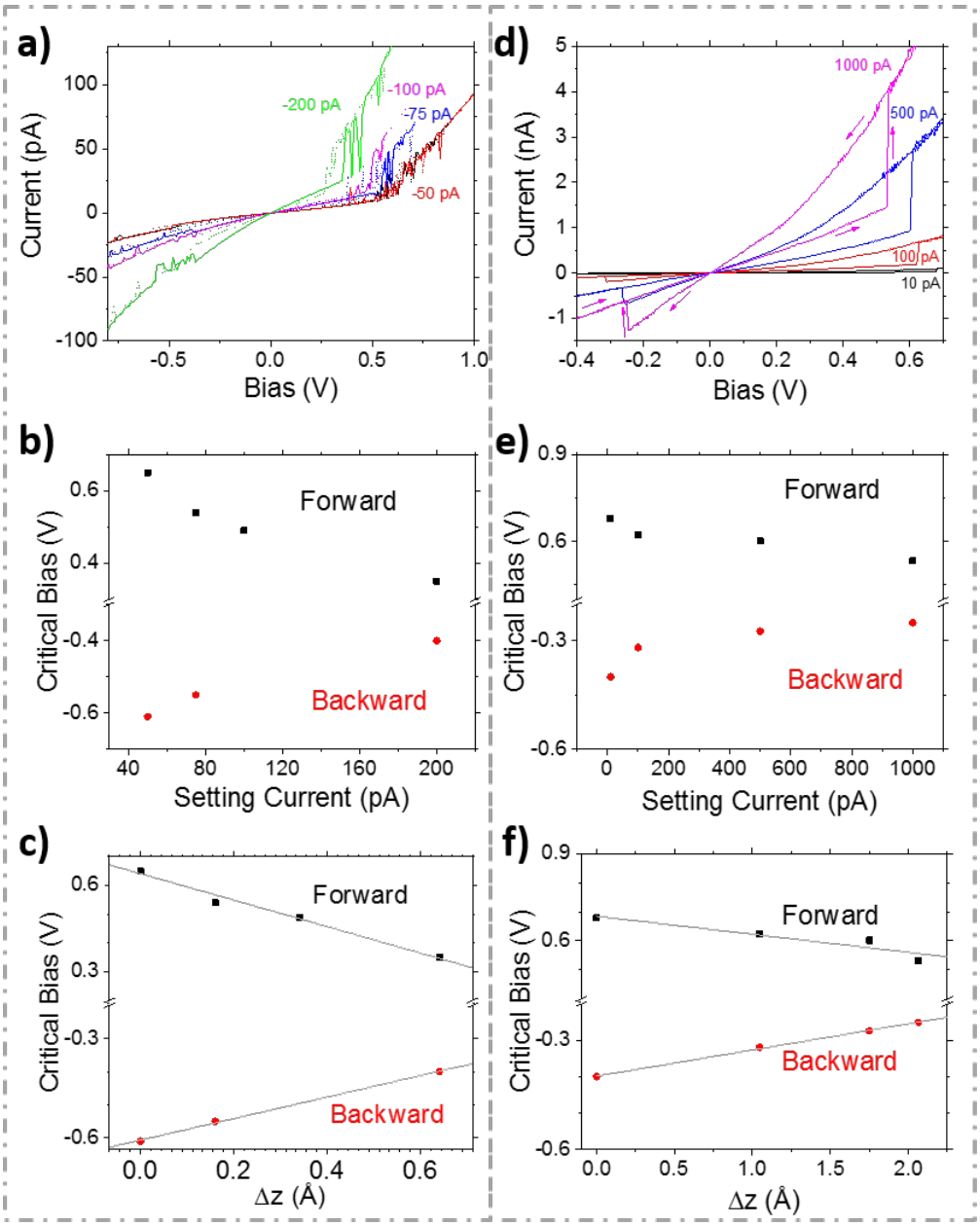

Figure 5.19: Response of the ferroelectric cycles with the tip-sample distance. a,d) Ferroelectric cycles for two different atoms. Change in the width of the cycle with the tip-sample distance. b,e) Critical bias transition for trace and retrace curves with different setting bias. c,f) Critical bias transition for the relative tip-sample distance with linear fits (grey curve) indicating a linear response and then, electric field induced effect.

meV/T (Fig. 5.20b,d). The Kondo splitting for state A and B experiences a variation for atom a) and d) of 0.07 and 0.13 meV/T respectively, which could be perfectly feasible if the atom environment is different [105].

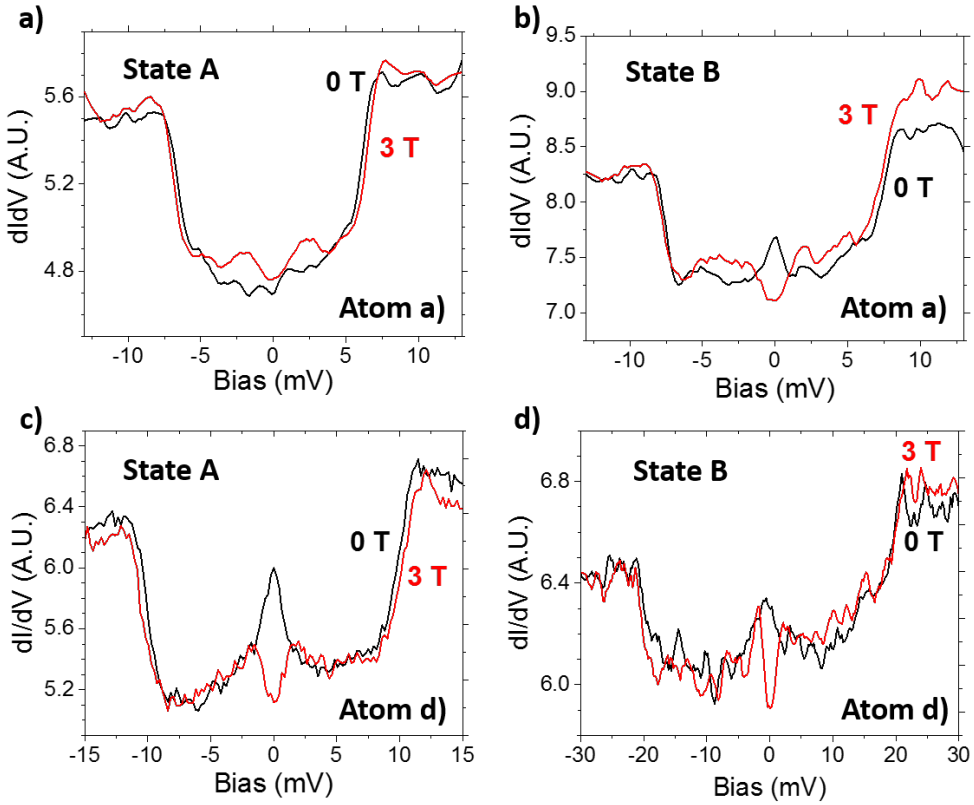

Figure 5.20: Inelastic excitation comparison for state A and B with 0 and 3 T. a,b) Atom corresponding to atom a) analyzed in the previous sections on state A and B at 0 and 3 T. c,d) Atom corresponding to atom d) analyzed in the previous sections on state A and B at 0 and 3 T.

5.6 Conclusion

In this chapter it has been possible to observe how charged neighbouring atoms (NaCl-ML aside to Co/Cu_2N/Cu(001)) are able to modify the magnetocrystalline anisotropy via crystal field effect.

Different adsorption sites of Co atoms on top of NaCl-ML have been determined with atomic precision. This has shown that most high symmetric sites (Co on Na and Cl site) do not show inelastic excitations in the absence of neighboring defects. It has been also shown that irregular features are Co atoms on top or close to Cl vacancies of NaCl-ML/Cu_2N/Cu(001), showing different inelastic excitations.

The previous chapter has demonstrated the possibility of reversing the surface dipoles with the help of electric fields (inverse piezoelectric effect). Here we have been shown that Cl vacancies can stabilize both states even at the single layer of NaCl on Cu_2N/Cu(001) leading towards ferroelectricity.

We have taken advantage of this fact to perform ferroelectric cycles with atoms adsorbed on top or close to vacancies. *Reading* with the help of IETS the magnetic properties of the adsorbed Co atoms in both states having thus, multiferroic cycles: writting with the help of electric fields and reading the states through the change of magnetocrystalline anisotropy and Kondo screening. In the experiments discussed here, the main impact takes place in the change in magnetocrystalline anisotropy, which points out to a change in the surface dipole rather than a charging process. Variations in the Kondo resonance are also found. For instance, in Fig. 5.16a the Kondo resonance is fully suppressed in state B, while in Fig 5.16d the resonance is broadened (higher Tk). In general, one could also expect a strong influence in the Kondo resonance from the MAE [42]. More importantly, we present examples in which the Kondo resonance remains in the two ferroelectric states (see Fig. 5.16b and 5.20c,d), where the only noticeable changes appear in the MAE splitting. This suggest that charging/discharging of the atoms can not be contributing to the transition between states A and B.

Applied magnetic fields have further confirmed the magnetic nature of the inelastic excitations. However behaviour of state 1 and 2 remains not accurately characterized with applied magnetic fields.

5.7 Future Work

This chapter opens the door for extensive studies of multiferroics at the atomic scale. From this point a wide variety of 3d transition metals such as Fe, Mn, Cr, and Ni can be evaporated on top of NaCl-ML/Cu_2N/Cu(001) to study their different total spin and the modification of the magnetocrystalline anisotropy with the ferroelectric cycle.

MgO has shown two interesting properties: adsorbed atoms showed strong bonding in this binary oxide with the rock-salt structure and a huge magnetocrystalline anisotropy in the case of adsorbed Co atoms [61, 104]. MgO could hence represent a new step forward in the understanding of ferroelectric cycles and magnetocrystalline anisotropy.

Chapter 6

Conclusion

6.1 Summary

In this thesis we have created a new heterostructure composed of atomically thin stacks of insulators and characterized it through the use of STM and AFM. We have shown that because Cu_2N acts as a charge modulated template and NaCl is ionic, both compounds interact strongly via electrostatic interactions. Because of this strong interaction, NaCl is commensurate wih Cu_2N, adopting its lattice parameter and suffering compressive strain of 7% respect its bulk lattice parameter.

The first consequence is that, because NaCl is strained and atoms in the same layer are brought closer, Pauli's repulsion stops Cl and Na from being co-planar (as they are in the regular binary rock-salt structure). Hence the surface is buckled breaking the center of symmetry and inducing a net out of plane surface dipole. The second consequence is that the insulating nature of Cu_2N plays a major role *insulating* the NaCl adlayer. In this way hybridization is prevented as well as charge transfer. The lack of surface charges due to the insulating host (compared to a metallic host) avoids the screening of the surface dipole.

The combination of these two consequences generates an inverse piezoelectric response on NaCl-BL/Cu_2N/Cu(001) that cannot be found on NaCl-BL/Cu(001). Inversion of a surface dipole is evidenced by a sharp change in the conductivity as well as in the calculated work function. The critical distance at which the transition occurs shifts linearly with the applied bias. This evidences an electric field driven effect, which is fully consistent with an inverse piezoelectric response. In addition, rumpling inversion is further supported by DFT calculations. To fully understand

the transition, simultaneous NC-AFM measurements were carried out. AFM measurements show analogously to I(z) measurements, a sharp drop in the measured frequency. Accordingly, the critical distance at which the transition happens shifts linearly with the applied bias. A simple model developed in this thesis explains the origin of the sharp drop as a change in the electrostatic term of the distance-force dependent curve (Δf (Δz)). The abrupt change in the electrostatic term can be explained as a non-local change of the surface dipoles since this term is intimately related to the dielectric constant.

Detailed analysis of Kelvin probe force measurements have shown that depending on the tip, both negative and positive contact potential difference are possible implying a possible effective electric field at zero bias negative and positive. Because of this, dipole inversion can also be found at small applied negative bias. These results are relevant since it implies that for electric field driven effects, the contact potential must be taken into account.

Defects on NaCl-BL/Cu_2N/Cu(001) have shown that when the tip is located on top of them and the electric field is ramped, the transition can also be found with two fundamental differences. Firstly, smaller electric fields are required to induce the dipole inversion and secondly hysteresis is observed at zero bias, resulting in bistability of the two different polarization states (nominally, the definition of ferroelectricity).

Lastly, Co atoms were evaporated on top of NaCl-ML/Cu_2N/Cu(001). A wide variety of spin excitations have been found in this system. Theoretical support provided in the future will be useful to explore the rich variety of features that are observed.. Furthermore, multiferroic cycles have been carried on with the help of vacancies. Atoms deposited on top of vacancies shows spin excitations with a well-defined magnetocrystalline anisotropy energy. This energy can be modified in a reproducible manner between states “1" and “2" which define the ferroelectric cycles. These results demonstrates the possibility of feasible multiferroicity at the ultimate limit, the single atom.

Bibliography

[1] Vladimir Fridkin. *Ferroelectricity at the Nanoscale*. Springer, 2014.

[2] K M Rabe, C H Ahn, and Jean-Marc Triscone. *Physics of Ferroelectrics*, volume 105. Springer, 2007.

[3] D D Fong, A M Kolpak, J A Eastman, S K Streiffer, P H Fuoss, G B Stephenson, Carol Thompson, D M Kim, K J Choi, C B Eom, I Grinberg, and A M Rappe. Stabilization of Monodomain Polarization in Ultrathin PbTiO3 Films. *Physical Review Letters*, 96(12):127601, 2006.

[4] B D Cullity and Graham C D. *Introduction to magnetic materials*. Wiley, 2nd edition, 2008.

[5] Claude Cohen Tannoudji, Bernard Diu, and Frank Laloe. *Quantum Mechanics Vol. 1*. 12th edition, 2006.

[6] Dante Gatteschi, Roberta Sessoli, and Jacques Villain. *Molecular Nanomagnets*. Oxford University Press, 2nd edition, 2010.

[7] W J de Haas, J de Boer, and G J van dën Berg. The electrical resistance of gold, copper and lead at low temperatures. *Physica*, 34:1115, 1934.

[8] Jun Kondo. Resistance Minimum in Dilute Magnetic Alloys Jun. *Prog. Theor. Phys.*, 32(1):37–49, 1964.

[9] Jun Kondo. Effect of ordinary scattering on exchange scattering from magnetic impurity in metals. *Physical Review Letters*, 169(2):437, 1968.

[10] Leo Kouwenhoven and Leonid Glazman. Revival of the Kondo effect. *Physics World*, 14(2):33–38, 2001.

[11] G Binnig and M Rohrer. Scanning Tunneling Microscopy. *Surface Science*, 126:236–244, 1983.

[12] Joseph A Stroscio and D M Eigler. Atomic and Molecular Manipulation with the Scanning Tunneling Microscope. *Science*, 254(5036):1319, 1991.

[13] C J Chen. *Introduction to Scanning Tunneling Microscopy*. Oxford University Press, 1991.

[14] H L Skriver and N M Rosengaard. *Physical Review B*.

[15] M. Crommie, C P Lutz, and D M Eigler. Imaging standing waves in a two-dimensional electron gas. *Nature*, 363:524–527, 1993.

[16] Markus Ternes. *Scanning tunneling spectroscopy at the single atom scale*. PhD thesis, TU Berlin, 2006.

[17] J Lambe and R C Jaklevic. Spectra by Inelastic Electron Tunneling. *Physical Review Letters*, 165(3):821–832, 1968.

[18] A Kogan, S Amasha, D Goldhaber-Gordon, G Granger, M Kastner, and Hadas Shtrikman. Measurements of Kondo and Spin Splitting in Single-Electron Transistors. *Physical Review Letters*, 93(16):166602, 2004.

[19] D M Eigler and E K Scheweizer. Positioning single atoms with a scanning tunnelling microscope. *Nature*, 344:524–526, 1990.

[20] K Morgenstern, N Lorente, and Karl-Heinz Rieder. Controlled manipulation of single atoms and small molecules using the scanning tunnelling microscope. *Physical Status Solidi B*, 1–81, 2013.

[21] Saw-Wai Hla. Scanning tunneling microscopy single atom/molecule manipulation and its application to nanoscience and technology. *Journal of Vacuum Science & Technology B: Microelectronics and Nanometer Structures*, 23(4):1351, 2005.

[22] Laurent Pizzagalli and Alexis Baratoff. Theory of single atom manipulation with a scanning probe tip:âĂČForce signatures, constant-height, and constant-force scans. *Physical Review B*, 68(11):115427, 2003.

[23] D M Eigler, C P Lutz, and W E Rudge. An atomic switch realized with the scanning tunnelling microscope. *Nature*, 352:600–603, 1991.

[24] Franz J Giessibl. Advances in atomic force microscopy. *Reviews of Modern Physics*, 75(949):949–983, 2003.

[25] Franz J Giessibl. Atomic resolution on Si(111)-(7X7) by noncontact atomic force microscopy with a force sensor based on a quartz tuning fork. *Applied Physics Letters*, 76(11):1470, 2000.

[26] Franz J Giessibl. Forces and frequency shifts in atomic-resolution dynamic-force microscopy. *Physical Review B*, 56(24):10–15, 1997.

[27] Leo Gross, Fabian Mohn, Nikolaj Moll, Peter Liljeroth, and Gerhard Meyer. The Chemical Structure of a Molecule Resolved by Atomic Force Microscopy. *Science*, 325(28):1110–1115, 2009.

[28] Christian Lotze. *Fundamental Processes in Single Molecule Junctions : Interplay of Forces and Electronic Effects*. PhD thesis, FU Berlin, 2013.

[29] J. C. Slater and F. H Frank. *Electromagnetism*. Dover Books on Physics, 2011.

[30] Fabian Mohn, Leo Gross, Nikolaj Moll, and Gerhard Meyer. Imaging the charge distribution within a single molecule. *Nature Nanotechnology*, 7(4):227–31, April 2012.

[31] L Zhang, T Miyamachi, T Tomanić, R Dehm, and W Wulfhekel. A compact sub-Kelvin ultrahigh vacuum scanning tunneling microscope with high energy resolution and high stability. *Review of Scientific Instruments*, 82(10):103702, 2011.

[32] S H Pan, E W Hudson, and J C Davis. [sup 3]He refrigerator based very low temperature scanning tunneling microscope. *Review of Scientific Instruments*, 70(2):1459, 1999.

[33] S H Pan, E W Hudson, and J C Davis. Vacuum tunneling of superconducting quasiparticles from atomically sharp scanning tunneling microscope tips. *Applied Physics Letters*, 73(20):2992, 1998.

[34] R Meservey and P M Tedrow. Spin-polarized electron tunneling. *Physics Reports*, 238(4):173–243, 1994.

[35] Michael Tinkham. *Introduction to Superconductivity*. Dover Books, 2004.

[36] D K Finnemore, T F Stromberg, and C A Swenson. Superconducting Properties of High-Purity Niobium. *Physical Review*, 149(1):231, 1966.

[37] Ralph C Dougherty and J Daniel Kimel. Temperature dependence of the superconductor energy gap. *ArXiv:1212.0423*, pages 1–23.

[38] F M Leibsle, S S Dhesi, S D Barrett, and A W Robinson. STM observations of Cu(100)–c(2x2)N surfaces: evidence for attractive interactions and an incommensurate c(2x2) structure. *Surface Science*, 317(3):309–320, 1994.

[39] F M Leibsle. The formation and properties of adsorbate nanostructures on Cu surfaces. *Nanotechnology*, 320, 1996.

[40] Cyrus F Hirjibehedin, Christopher P Lutz, and Andreas J Heinrich. Spin coupling in engineered atomic structures. *Science*, 312(5776):1021–4, 2006.

[41] Cyrus F Hirjibehedin, Chiung-Yuan Lin, Alexander F Otte, Markus Ternes, Christopher P Lutz, Barbara a Jones, and Andreas J Heinrich. Large magnetic anisotropy of a single atomic spin embedded in a surface molecular network. *Science*, 317(5842):1199–203, 2007.

[42] Jenny C Oberg, M Reyes Calvo, Fernando Delgado, María Moro-Lagares, David Serrate, David Jacob, Joaquín Fernández-Rossier, and Cyrus F Hirjibehedin. Control of single-spin magnetic anisotropy by exchange coupling. *Nature Nanotechnology*, 9(1):64–8, 2014.

[43] Alexander F Otte, Markus Ternes, Kirsten von Bergmann, Sebastian Loth, Harald Brune, Christopher P Lutz, Cyrus F Hirjibehedin, and Andreas J Heinrich. The role of magnetic anisotropy in the Kondo effect. *Nature Physics*, 4(11):847–850, 2008.

[44] David EÌĄcija, Marta Trelka, Christian Urban, Paula de Mendoza, Antonio Echavarren, Roberto Otero, JoseÌĄ MariÌĄa Gallego, and Rodolfo Miranda.

Templated growth of an ordered array of organic bidimensional mesopores. *Applied Physics Letters*, 92(22):223117, 2008.

[45] T Parker, L Wilson, N Condon, and F Leibsle. Epitaxy controlled by self-assembled nanometer-scale structures. *Physical Review B*, 56(11):6458–6461, 1997.

[46] R Bennewitz, V Barwich, M Bammerlin, C Loppacher, M Guggisberg, A Baratoff, E Meyer, and H Gu. Ultrathin films of NaCl on Cu (111): a LEED and dynamic force microscopy study. *Surface Science*, 438:289–296, 1999.

[47] Jascha Repp, Gerhard Meyer, Sladjana Stojković, André Gourdon, and Christian Joachim. Molecules on Insulating Films: Scanning-Tunneling Microscopy Imaging of Individual Molecular Orbitals. *Physical Review Letters*, 94(2):026803, 2005.

[48] Jascha Repp, Gerhard Meyer, Fredrik E Olsson, and Mats Persson. Controlling the charge state of individual gold adatoms. *Science*, 305(5683):493–5, 2004.

[49] J H Haeni, P Irvin, W Chang, R Uecker, P Reiche, and Y L Li. Room-temperature ferroelectricity in strained $SrTiO_3$. *Nature*, 430:758–761, 2004.

[50] Pavlo Zubko, Stefano Gariglio, Marc Gabay, Philippe Ghosez, and Jean-Marc Triscone. Interface Physics in Complex Oxide Heterostructures. *Annual Review of Condensed Matter Physics*, 2(1):141–165, 2011.

[51] H Y Hwang, Y Iwasa, M Kawasaki, B Keimer, N Nagaosa, and Y Tokura. Emergent phenomena at oxide interfaces. *Nature Materials*, 11(2):103–13, 2012.

[52] A K Geim and I V Grigorieva. Van der Waals heterostructures. *Nature*, 499(7459):419–25, 2013.

[53] Jacek Goniakowski and Claudine Noguera. Polarization and rumpling in oxide monolayers deposited on metallic substrates. *Physical Review B*, 79(15):155433, 2009.

[54] K S Novoselov, A K Geim, S V Morozov, D Jiang, Y Zhang, S V Dubonos, I V Grigorieva, and A A Firsov. Electric Field Effect in Atomically Thin Carbon Films. *Science*, 306(5696):666–669, 2004.

[55] C R Dean, A F Young, I Meric, C Lee, L Wang, S Sorgenfrei, K Watanabe, T Taniguchi, P Kim, K L Shepard, and J Hone. Boron nitride substrates for high-quality graphene electronics. *Nature Nanotechnology*, 5(10):722–6, 2010.

[56] Patrick Vogt, Paola De Padova, Claudio Quaresima, Jose Avila, Emmanouil Frantzeskakis, Maria Carmen Asensio, Andrea Resta, Bénédicte Ealet, and Guy Le Lay. Silicene: Compelling Experimental Evidence for Graphenelike Two-Dimensional Silicon. *Physical Review Letters*, 108(15):155501, 2012.

[57] N Nilius, T M Wallis, and W Ho. Influence of a Heterogeneous A l 2 O 3 Surface on the Electronic Properties of Single Pd Atoms. *Physical Review Letters*, 90(4):046808, 2003.

[58] Igor Beinik, Clemens Barth, Margrit Hanbücken, and Laurence Masson. KCl ultra-thin films with polar and non-polar surfaces grown on Si(111)7 ÃŮ 7. *Scientific Reports*, 5(111):8223, 2015.

[59] Christian Loppacher, Ulrich Zerweck, and Lukas M Eng. Kelvin probe force microscopy of alkali chloride thin films on Au(111). *Nanotechnology*, 15(2):S9–S13, 2004.

[60] J.J. Kolodziej, B. Such, P. Czuba, F. Krok, P. Piatkowski, and M. Szymonski. Scanning-tunneling/atomic-force microscopy study of the growth of {KBr} films on insb(001). *Surface Science*, 506(1–2):12–22, 2002.

[61] Ileana G Rau, Susanne Baumann, Stefano Rusponi, Fabio Donati, Sebastian Stepanow, Luca Gragnaniello, Jan Dreiser, Cinthia Piamonteze, Frithjof Nolting, Shruba Gangopadhyay, Oliver R Albertini, Roger M Macfarlane, Christopher P Lutz, Barbara Jones, Pietro Gambardella, Andreas J Heinrich, and Harald Brune. Reaching the Magnetic Anisotropy Limit of a 3d Metal Atom. *Science*, 344(6187):988–992, 2014.

[62] Jascha Repp, Stefan Fölsch, Gerhard Meyer, and Karl-Heinz Rieder. Ionic Films on Vicinal Metal Surfaces: Enhanced Binding due to Charge Modulation. *Physical Review Letters*, 86(2):252–255, 2001.

[63] Eric Bousquet, Nicola A Spaldin, and Philippe Ghosez. Strain-Induced Ferroelectricity in Simple Rocksalt Binary Oxides. *Physical Review Letters*, 104(3):037601, 2010.

[64] Bog G Kim. Epitaxial strain induced ferroelectricity in rocksalt binary compound: Hybrid functional Ab initio calculation and soft mode group theory analysis. *Solid State Communications*, 151(9):674–677, 2011.

[65] G Kresse and D Joubert. From ultrasoft pseudopotentials to the projector augmented-wave method. *Physical Review B*, 59:1758–1775, 1999.

[66] P E Blöchl. Projector augmented-wave method. *Physical Review B*, 50(24):17953–17978, 1994.

[67] M Dion, H Rydberg, E Schröder, D C Langreth, and B I Lundqvist. Van der Waals density functional for general geometries. *Physical Review Letters*, 92(24):246401, 2004.

[68] T Thonhauser, Valentino R Cooper, Shen Li, Aaron Puzder, Per Hyldgaard, and David C Langreth. Van der Waals density functional: Self-consistent potential and the nature of the van der Waals bond. *Physical Review B*, 76(12):125112, 2007.

[69] Guillermo Román-Pérez and José M Soler. Efficient implementation of a van der Waals density functional: application to double-wall carbon nanotubes. *Physical Review Letters*, 103(9):096102, 2009.

[70] Jirí Klimeš, David R Bowler, and Angelos Michaelides. Van der Waals density functionals applied to solids. *Physical Review B*, 83(19):195131, 2011.

[71] T Choi, C Ruggiero, and J Gupta. Incommensurability and atomic structure of c(2X2)N/Cu(100): A scanning tunneling microscopy study. *Physical Review B*, 78(3):035430, 2008.

[72] Werner A Hofer, Adam S Foster, and Alexander L Shluger. Theories of scanning probe microscopes at the atomic scale. *Reviews of Modern Physics*, 75(October):1287–1331, 2003.

[73] J K Gimzewsky, R Möller, D W Pohl, and R R Schlittler. Transition from Tunnelling to Point Contact Investigated by Scanning Tunnelling Microscopy and Spectroscopy. *Surface Science*, 190:15–23, 1987.

[74] W Hebenstreit, J Redinger, Z Horozova, M Schmid, R Podloucky, and P Varga. Atomic resolution by STM on ultra-thin films of alkali halides : experiment and local density calculations. *Surface Science*, 424(2-3), 1999.

[75] C D Ruggiero, M Badal, T Choi, and J A Gupta. Emergence of surface states in nanoscale Cu2N islands. *Physical Review B*, 83, 2011.

[76] C D Ruggiero, T Choi, and J A Gupta. Tunneling spectroscopy of ultrathin insulating films: CuN on Cu(100). *Applied Physics Letters*, 91(25):253106, 2007.

[77] Alexander Kabakchiev. *Scanning Tunneling Luminescence of Pentacene Nanocrystals*. PhD thesis, École Polytechnique Fédérale de Lausanne, 2010.

[78] Javier Junquera and Philippe Ghosez. Critical thickness for ferroelectricity in perovskite ultrathin films. *Nature*, 422(February):506–509, 2003.

[79] Matthew F Chisholm, Weidong Luo, Mark P Oxley, Sokrates T Pantelides, and Ho Nyung Lee. Atomic-Scale Compensation Phenomena at Polar Interfaces. *Physical Review Letters*, 105(19):197602, 2010.

[80] Zhicheng Zhong, G Koster, and Paul J Kelly. Prediction of thickness limits of ideal polar ultrathin films. *Physical Review B*, 85(12):121411, 2012.

[81] Mathias Müller, Julian Ikonomov, and Moritz Sokolowski. Structure of Epitaxial Layers of KCl on Ag(100). *Surface Science*, 605(11-12):1090–1094, 2011.

[82] A Helms and K H Rieder. Epitaxy of ionic insulators on a vicinal metal substrate : KCl and RbI on Cu(211). *Applied Surface Science*, 08:270–274, 2000.

[83] Masao Katayama, Keiji Ueno, Atsushi Koma, Manabu Kiguchi, and Koichiro Saiki. Scanning Tunneling Microscopy and Spectroscopy Study of LiBr/Si(001) Heterostructure. *Japanese Journal of Applied Physics*, 43(No. 2A):L203–L205, 2004.

[84] N A Spaldin. Fundamental Size limits in Ferroelectricity. *Science*, 304(1606), 2004.

[85] R Ramesh and N A Spaldin. Multiferroics : progress and prospects in thin fi lms. *Nature Materials*, 6:21–29, 2007.

[86] Martin Gajek, Manuel Bibes, Stéphane Fusil, Karim Bouzehouane, Josep Fontcuberta, Agnès Barthélémy, and Albert Fert. Tunnel junctions with multiferroic barriers. *Nature Materials*, 6(4):296–302, 2007.

[87] Dillon D Fong, G Brian Stephenson, Stephen K Streiffer, Jeffrey A Eastman, Orlando Auciello, and Paul H Fuoss. Ferroelectricity in Ultrathin Perovskite Films. *Sicence*, 304(5677):1650–1653, 2004.

[88] A Gruverman, D Wu, H Lu, Y Wang, H W Jang, C M Folkman, M Ye Zhuravlev, D Felker, M Rzchowski, C Eom, and E Y Tsymbal. Tunneling Electroresistance Effect in Ferroelectric Tunnel Junctions at the Nanoscale. *Nano Letters*, 9(10):3539–3543, 2009.

[89] T C Leung, C L Kao, W S Su, Y J Feng, and C T Chan. Relationship between surface dipole, work function and charge transfer: Some exceptions to an established rule. *Physical Review B*, 68(19):195408, 2003.

[90] Leo Gross, Bruno Schuler, Fabian Mohn, Nikolaj Moll, Niko Pavliček, Wolfram Steurer, Ivan Scivetti, Konstantinos Kotsis, Mats Persson, and Gerhard Meyer. Investigating atomic contrast in atomic force microscopy and Kelvin probe force microscopy on ionic systems using functionalized tips. *Physical Review B*, 90(15):155455, 2014.

[91] Yoshiaki Sugimoto, Pablo Pou, Masayuki Abe, Pavel Jelinek, Rubén Pérez, Seizo Morita, and Oscar Custance. Chemical identification of individual surface atoms by atomic force microscopy. *Nature*, 446(7131):64–7, 2007.

[92] N Kocić, P Weiderer, S Keller, S Decurtins, S-X Liu, and J Repp. Periodic Charging of Individual Molecules Coupled to the Motion of an Atomic Force Microscopy Tip. *Nano letters*, 15(7):4406–11, 2015.

[93] F J Giessibl. A direct method to calculate tip-sample forces from frequency shifts in frequency-modulation atomic force microscopy. *Applied Physics Letters*, 78(1):123, 2001.

[94] Jascha Repp, Gerhard Meyer, Sami Paavilainen, Fredrik Olsson, and Mats Persson. Scanning Tunneling Spectroscopy of Cl Vacancies in NaCl Films: Strong Electron-Phonon Coupling in Double-Barrier Tunneling Junctions. *Physical Review Letters*, 95(22):225503, 2005.

[95] Nicola A Spaldin and Manfred Fiebig. The Reinaissance of Magnetoelectric Multiferroics. *Science*, 309(391), 2005.

[96] Thomas Lottermoser, Thomas Lonkai, Uwe Amann, and Manfred Fiebig. Magnetic phase control by an electric field. *Nature*, 430:541–544, 2004.

[97] L Gerhard, T K Yamada, T Balashov, A F Takács, R J H Wesselink, M Däne, M Fechner, S Ostanin, A Ernst, I Mertig, and W Wulfhekel. Magnetoelectric coupling at metal surfaces. *Nature Nanotechnology*, 5(11):792–7, 2010.

[98] A Sonntag, J Hermenau, A Schlenhoff, J Friedlein, S Krause, and R Wiesendanger. Electric-field-induced magnetic anisotropy in a nanomagnet investigated on the atomic scale. *Physical Review Letters*, 112(1):017204, 2014.

[99] Sebastian Loth, Susanne Baumann, Christopher P Lutz, D M Eigler, and Andreas J Heinrich. Bistability in atomic-scale antiferromagnets. *Science*, 335(6065):196–9, 2012.

[100] David Serrate, Paolo Ferriani, Yasuo Yoshida, Saw-Wai Hla, Matthias Menzel, Kirsten von Bergmann, Stefan Heinze, Andre Kubetzka, and Roland Wiesendanger. Imaging and manipulating the spin direction of individual atoms. *Nature Nanotechnology*, 5(5):350–3, 2010.

[101] Toshio Miyamachi, Tobias Schuh, Tobias Märkl, Christopher Bresch, Timofey Balashov, Alexander Stöhr, Christian Karlewski, Stephan André, Michael Marthaler, Martin Hoffmann, Matthias Geilhufe, Sergey Ostanin, Wolfram Hergert, Ingrid Mertig, Gerd Schön, Arthur Ernst, and Wulf Wulfhekel. Stabilizing the magnetic moment of single holmium atoms by symmetry. *Nature*, 503(7475):242–246, 2013.

[102] F Donati, a Singha, S Stepanow, C Wäckerlin, J Dreiser, P Gambardella, S Rusponi, and H Brune. Magnetism of Ho and Er atoms on close-packed metal surfaces. *Physical Review Letters*, 113(23):237201, 2014.

[103] M Steinbrecher, A Sonntag, M Dos Santos Dias, M Bouhassoune, S Lounis, J Wiebe, R Wiesendanger, and a a Khajetoorians. Absence of a spin-signature from a single Ho adatom as probed by spin-sensitive tunneling. *Nature Communications*, 7:10454, 2016.

[104] F Donati, S Rusponi, S Stepanow, A Singha, L Persichetti, R Baltic, K Diller, F Patthey, E Fernandes, J Dreiser, K Kummer, C Nistor, P Gambardella, and H Brune. Magnetic remanence in single atoms. *Science*, 352(6283):318–321, 2016.

[105] B Bryant, a Spinelli, J J T Wagenaar, M Gerrits, and a F Otte. Local control of single atom magnetocrystalline anisotropy. *Physical Review Letters*, 111(12):127203, 2013.

[106] Sebastian Loth, Kirsten von Bergmann, Markus Ternes, Alexander F Otte, Christopher P Lutz, and Andreas J. Heinrich. Controlling the state of quantum spins with electric currents. *Nature Physics*, 6(5):340–344, 2010.

[107] T Choi, C D Ruggiero, and J A Gupta. Tunneling spectroscopy of ultrathin insulating Cu_2N films, and single Co adatoms. *Journal of Vacuum Science & Technology B: Microelectronics and Nanometer Structures*, 27(2):887, 2009.

[108] Zhe Li, Koen Schouteden, Violeta Iancu, Ewald Janssens, Peter Lievens, and Chris Van Haesendonck. Chemically modified STM tips for atomic-resolution imaging on ultrathin NaCl films. *Nano Research*, 8(7):2223–2230, 2015.

[109] Ivar Giaever. Energy gap in superconductors measured by electron tunneling. *Physical Review Letters*, 5(4):147–148, 1960.

[110] J M De Teresa. Role of Metal-Oxide Interface in Determining the Spin Polarization of Magnetic Tunnel Junctions. *Science*, 286(5439):507–509, 1999.

[111] V Garcia, S Fusil, K Bouzehouane, S Enouz-Vedrenne, N D Mathur, a Barthélémy, and M Bibes. Giant tunnel electroresistance for non-destructive readout of ferroelectric states. *Nature*, 460(7251):81–4, 2009.

[112] D Eichler, S G Lucek, F A Aharonian, V N Zirakashvili, W M Goss, C L Brogan, M J Claussen, J Rho, T H Jarrett, S D Hunter, G Kanbach, P Sreekumar, J M Cordes, R J Dewey, K D Kuntz, R L Shelton, E B Giacani, G Dubner, C Brogan, N E Kassim, R A Chevalier, D C Ellison, Y A Uvarov, I V Moskalenko, A W Strong, A Mastichiadis, R H Becker, R L White, A Fallon, and S Tuttle. Ferroelectric Control of Spin Polarization. *Science*, (327):1106–1111, 2010.